MINERAL CHEMISTRY AND ND ISOTOPE GEOCHEMISTRY OF APATITE IN OROGENIC AU-ASSOCIATED GABBROS, BAIE VERTE, NEWFOUNDLAND

A thesis submitted

to the School of Graduate Studies in partial fulfillment of the

requirements for the degree of

Master of Science

Department of Earth Sciences

Memorial University of Newfoundland

St. John's, Newfoundland and Labrador

September 2023

Abstract

Orogenic Au deposits on the Baie Verte Peninsula, Newfoundland Appalachians, are structurally controlled and primarily hosted by Lower Ordovician volcanic cover sequences (Snooks Arm Group) and ophiolitic rocks. Gabbro-hosted orogenic Au can be found in three locations: the Stog'er Tight (642,000 t @ 3.02 g/t Au indicated, and 53,000 t @ 5.63 g/t Au inferred resources), the Argyle (436,800 t @ 2.53 g/t Au indicated and 500 t @ 2.77 g/t Au inferred resources) deposits, and the Animal Pond prospect. All these deposits are located in the hanging wall of the Scrape thrust fault typically within 100s of meters of the surface trace of the fault. Gold mineralization in all three areas is associated with coarse-grained, pegmatoidal gabbros that are variably deformed and were metasomatically altered by orogenic Au-related hydrothermal fluids. Gold is also associated with hydrothermally modified apatite, hydrothermal zircon, monazite ($(Ce,La)PO_4$) and xenotime (YPO_4). Phosphate minerals are widely distributed throughout the Au-related hydrothermal alteration zones. The deposition of gold occurred concurrent with the dissolution and reprecipitation in apatite, which caused the leaching of REE from apatite and the precipitation of coeval hydrothermal monazite and xenotime.

All apatite in fresh and altered rocks are subhedral to euhedral and have homogeneous backscattered electron images. In contrast, cathodoluminescence (CL) images for apatite in unaltered rocks displays yellow to yellow-green luminescence, whereas apatite in altered rocks displays a dark green to gray luminescence. Electron microprobe and laser ablation inductively coupled plasma mass spectrometry data for

apatite in altered rocks show they are depleted in Mn, Cl, LREE (low La/Yb_N, La/Sm_N), Th, and U, and enriched in Sr and and have higher Sr/Y compared to apatite in the fresh rocks. This is compatible with the altered apatites having experienced fluid aided REE-Mn-Cl-Th-U remobilization and subsequent growth of hydrothermal monazite and lesser xenotime inclusions. Despite variable elemental concentrations, the Nd isotope signatures of fresh and altered apatite are similar in all apatite grains with $\varepsilon_{Nd}(t)$= +2.34-6.60 vs. =+2.80-6.96, respectively.

This study highlights that the combination of textural studies, CL imaging, and chemical composition of apatite can be used to determine igneous vs apatite influenced by Au-related hydrothermal alteration and that apatite can be modified by hydrothermal fluids during fluid-rock interaction.

Acknowledgements

First and foremost, I would like to thank my supervisor, Dr. Stephen Piercey for his guidance, endless support, and trusting me with this project during my time at the Memorial University of Newfoundland. Steve's supervision style has allowed me to be independent and flexible regarding the direction of this research project, which has helped me develop into the scientist I am today.

Lab work for this project would not have been possible without the help of John Hanchar, Wanda Aylward, Rebecca Lam, Markus Wälle, Matt Crocker, and Dylan Goudie. I'd also like to extend my gratitude to Dr. Gregory Dunning as my supervisory committee member, for his constructive comments and feedback on the thesis. I am particularly grateful to Nikola Denisova for helpful comments on early drafts of the manuscript. I would like to acknowledge the remaining members of the Piercey Research Group, for the time you listened to me about apatite.

Last but certainly not least, I also wish to thank my families in Istanbul and Batman for their constant support and understanding, and finally to my both colleague and husband Lokman, for his endless emotional support and encouragement. My Newfoundland adventure would be incomplete without you. Thank you for being you and pushing me beyond my comfort zone.

Financial support for this master's thesis has been provided by the Republic of Türkiye Ministry of National Education to Fatma Gümüş and an NSERC Discovery Grant to Dr. Stephen J. Piercey.

Table of Content

Abstract i
Acknowledgements iii
Table of Content iv
List of Figures vii
List of Abbrevations xii
List of Appendices xv
Chapter 1: Introduction to the gabbro hosted orogenic gold deposits in Baie Verte, Newfoundland, Canada 1
1.1. Orogenic Gold Deposits 2
1.2. Exploration History 6
1.3. Regional Geology and Tectonic Evolution 8
1.4. Geology of the Baie Verte Peninsula 10
1.5. Stratigraphy 14
1.6. Deposit Geology 15
1.7. Analytical Methods 19
1.8. Co-authorship statement 19
1.9. Presentation 20
1.10. References 21
Chapter 2: Mineral Chemistry and Nd Isotope Geochemistry of Apatite in Orogenic Au-associated Gabbros, Baie Verte, Newfoundland 38
2.1. Abstract 38
2.2. Introduction 40
2.3. Geological Setting 42
2.4. Baie Verte Peninsula Gabbro Hosted Orogenic Gold Deposit Characteristics 45
2.5. Apatite 46
2.5.1. Apatite luminescence 48
2.6. Sampling and Analytical Methods 49
2.6.1. Sample selection and preparation 49
2.6.2. Bench-top cathodoluminescence 51

2.6.3. Scanning electron microscopy 51
2.6.4. Scanning electron microscopy-mineral liberation analysis (SEM-MLA) .. 52
2.6.5. Electron probe micro analysis (EPMA) 52
2.6.6. Laser ablation split stream (LASS) trace elements–Nd isotopes in apatite 54
2.7. Results 55
2.7.1. Textural characteristics 55
2.7.1.1. Apatite in unaltered rocks 56
2.7.1.2. Apatite in altered rocks 57
2.7.2. Apatite major and trace elements geochemistry 58
2.7.3. In situ Nd isotopic compositions of apatite 60
2.8. Discussion 60
2.8.1. Apatite textures 61
2.8.2. Apatite composition variations 62
2.8.2.1. Eu anomalies in apatite 66
2.8.2.2. The oxidation state of apatite during precipitation: insights from Eu/Eu* and Ce/Ce* 67
2.8.3. Neodymium isotopic composition variations 69
2.8.4. Vectors to Mineralization 70
2.8.5. Conclusions 72
2.8.6. References 74
Chapter 3: Summary and Future Work 113
3.1. Summary 113
3.2. Suggestions for Future Research 115
APPENDIX A: Representative BSE images of apatites from the Animal Pond Prospect, Stog'er Tight and Argyle deposits 116
APPENDIX B: Representative CL images of apatites from the Animal Pond Prospect, Stog'er Tight and Argyle deposits 124
APPENDIX C: Scanning electron microscopy-mineral liberation analysis (SEM-MLA) of the mounts from the Animal Pond Prospect, Stog'er Tight and Argyle deposits 132
APPENDIX D: Summarized methods for EPMA and EPMA average oxide and apfu results of apatite from the Animal Pond Prospect, Stog'er Tight and Argyle deposits .. 134

APPENDIX E: Summarized methods for LASS (LA-ICPMS and LA-MC- ICPMS) and trace element results of apatite from the Animal Pond Prospect, Stog'er Tight and Argyle deposits 137

APPENDIX F: Nd results for apatite grains from LASS, and calculation of $\varepsilon_{Nd}(t)$ 142

List of Figures

Figure 1.1. Tectonic settings in which gold deposits form. Orogenic gold deposits are found in deformed forearcs and backarcs, in addition to sheared margins of continental arc batholiths (modified after Goldfarb and Groves, 2015).

Figure 1.2. Inferred crustal levels of formation of orogenic gold deposits (modified after Poulsen et al., 2000; Dubé et al., 2001; Dubé and Gosselin, 2007).

Figure 1.3. Geological map of the Stog'er Tight Area showing the Stog'er Tight Mine and the two pits constraining the 2021 Stog'er Tight Mineral Resource (modified after Kuntz et al., 2021).

Figure 1.4. Diamond drill hole locations and geology of Argyle Deposit.(modified after Kuntz et al., 2021).

Figure 1.5. a) Simplified map of tectonostratigraphic terranes of Newfoundland (modified after Williams, 1979 and Williams et al., 1988). b) Geology map of the Baie Verte Peninsula (modified after Skulski et al., 2010 and Pawlukiewicz, 2019).

Figure 1.6. Stratigraphy of the Point Rousse Complex (modified after Skulski et al., 2009).

Figure 2.1. a) Simplified map of tectonostratigraphic terranes of Newfoundland (modified after Williams, 1979 and Williams et al., 1988). b) Geology map of the Baie Verte Peninsula (modified after Skulski et al., 2010 and Pawlukiewicz, 2019).

Figure 2.2. Stratigraphy of the Point Rousse Complex (modified after Skulski et al., 2009).

Figure 2.3. Geological map of the Point Rousse Peninsula showing the various deposits (modified after Skulski et al., 2010 and Pawlukiewicz, 2019).

Figure 2.4. a-c) Cross sections through Stog'er Tight and Argyle deposits and b) stratigraphic section from Animal Pond showing gabbro-hosted mineralization.

Figure 2.5. Photographs of samples of various gabbros from the Animal Pond prospect, Stog'er Tight and Argyle deposits: a) pegmatoidal plagioclase-rich gabbro with relict cumulate textures and weak albite alteration; b) medium-grained gabbro with minor brown, leucoxene alteration; c) medium- to coarse-grained gabbro with pinkish albite alteration of feldspar with minor chlorite-epidote in the matrix; d) medium-grained albite-chlorite-hematite altered gabbro; e) brick red albite-chlorite-Fe-carbonate-hematite altered gabbro with quartz veins and "sooty" pyrite grains that contain gold. This type of sample is typical of high grade mineralization in Stog'er Tight; f) foliated albite-hematite-chlorite altered gabbro with quartz veins that are cross cutting the foliation as well as those that are parallel to the foliation; g) medium-grained gabbro with chlorite, albite, and hematite alteration; h) albite-chlorite-carbonate altered gabbro with cross-cutting quartz veins; and i) gabbro with feldspars partly altered to albite and beige coloured leucoxene (titanite-rutile intergrown?).

Figure 2.6. Representative back-scattered electron and cathodoluminescence photomicrographs illustrating the key petrographic features of the magmatic apatite; a)

needle-shaped or fine-grained apatite intergrown with albite in Argyle deposit; b) apatite grain from the Animal Pond prospect showing no internal texture; c) apatite occurring as an inclusion within titanomagnetite with exsolved ilmenite ; d) apatite coexisting with ilmenite displaying a euhedral crystal shape and has a bright reflection in the Animal Pond prospect; e-f) apatite coexisting with zircon in the Animal Pond prospect; g) apatite showing distinct dark core-light rim zonation from the Animal Pond prospect; h-i) euhedral to subhedral apatite grains showing yellow and yellow-green luminescence in Argyle deposit. Abbreviations: Ab= Albite, Amph= Amphibole, Ap = Apatite, Cal=Calcite, Ilm= Ilmenite, Py = Pyrite, Zr = Zircon.

Figure 2.7. Representative back-scattered electron and cathodoluminescence photomicrographs illustrating the key petrographic features of the hydrothermally modified apatite: a-d) hydrothermally influenced apatite coexisting with secondary hydrothermal minerals, including monazite, xenotime, and zircon in Stog'er Tight deposit; e) acicular apatite in Argyle deposit; f) apatite grains showing dark rims and bright cores in the early stages of alteration in Stog'er Tight deposit; g-i) apatite grains displaying complex CL features with heterogeneous patchy pattern from Stog'er Tight and Argyle deposits; j-l) apatite grains showing distinct dark green to gray luminescence from Stog'er and Argyle deposits. Abbreviations: Ab= Albite, Amph= Amphibole, Ap = Apatite, Cal=Calcite, Chl= Chlorite, Mnz= Monazite, Xtm= Xenotime, Zr = Zircon.

Figure 2.8. Photomicrographs of apatite associated with orogenic gold within pyrite: a) backscatter image of the hydrothermally influenced apatite grain with gold inclusions within pyrite crystal in the most altered zones from Stog'er Tight deposit; and b) gold

infilling voids and fractures within pyrite from Argyle deposit. Abbreviations: Ap = apatite, Py= pyrite, Au=gold, Ab=albite, Cal=calcite.

Figure 2.9. Diagrams illustrating the halogen and Na_2O contents of apatite from the Animal Pond prospect, Stog'er Tight and Argyle deposits. a) Ternary OH-Cl-F plot (using Approach 3 of Ketcham, 2015); b) Cl versus F plot; c) F/Cl ratio and Na_2O contents.

Figure 2.10. Box-and-whisker plots showing the major element contents of fluorapatite from the Animal Pond prospect, Stog'er Tight and Argyle deposits (based on EPMA analysis). Line =median value; square = mean value; box = interquartile range; triangle= a far outlier; circle= an outlier.

Figure 2.11. Trace element composition of apatite in unaltered and altered host rocks, showing that altered samples are depleted in Mn and Cl. (apfu = atomic per formula unit).

Figure 2.12. Diagrams displaying trace-element variations of fluorapatite from the Animal Pond prospect, Stog'er Tight and Argyle deposits: a) Y (ppm) versus Sr (ppm); b) ternary Sr-Y-REE plot; c) Th (ppm) versus U (ppm); and d) Sr/Y versus LREE (La + Ce + Pr + Nd) (ppm).

Figure 2.13. Binary plots of trace element concentrations and ratios of fluorapatite from the Animal Pond prospect, Stog'er Tight and Argyle deposits, illustrating differences between magmatic and hydrothermal apatite. a) La/Yb_N versus La/Sm_N; b) La/Sm_N versus Eu/Eu*; c) La/Yb_N versus Eu/Eu*. Normalizing (N) values taken from Taylor and Mclennan (1985).

Figure 2.14. a) Eu/Eu* versus Ce/Ce* in fluoroapatite (Mercer et al., 2020); b-c) Eu/Eu* versus Mn, and Sr contents in the fluorapatite; $Eu/Eu^* = (Eu)_{CN}/[(Sm)_{CN} \times (Gd)_{CN}]^{0.5}$; $Ce/Ce^* = Ce_{CN}/[(La_{CN} \times Nd_{CN})]^{0.5}$. CN – chondrite normalized. Normalization values are from Taylor and Mclennan (1985).

Figure 2.15. Chondrite-normalized REE and Y diagrams in fluorapatite (McDonough and Sun, 1995).

Figure 2.16. a) Plot of $^{143}Nd/^{144}Nd$ versus $^{147}Sm/^{144}Nd$ for fluorapatite. A 420 Ma Sm-Nd isochron is shown for reference; b) Histogram of $(^{143}Nd/^{144}Nd)_t$ distribution for the fluorapatite; c) Histogram of $(\varepsilon_{Nd})t$ (420 Ma) distribution for the fluorapatite; d) Histogram of T_{DM} distribution for the fluorapatite.

List of Abbrevations

Amph-Amphibole

Ab-Albite

Alt- Alteration

Ank-Ankerite

Ap – Apatite

Apfu = Atomic per formula unit

Au-Gold

BSE imaging - Back-scattered electron imaging

BIF- Banded iron formation

BVBL-Baie Verte-Brompton line

BVL- Baie Verte Line

BVOT- Baie Verte oceanic tract

Cal-calcite

CCD- Charge-coupled device

Chl-Chlorite

CHUR- Chondritic uniform reservoir CHUR

CL - Cathodoluminescence

EDS - Energy-dispersive spectroscopy

EPMA - Electron probe micro-analyzer

GRUB- Gander River ultrabasic belt

HREE- Heavy rare earth elements

HR-ICPMS- High resolution double-focusing magnetic sector-inductively coupled plasma mass spectrometer

ID-TIMS - Isotope dilution-thermal ionization mass spectrometry

Ilm-Ilmenite

IOA- Iron-oxide apatite

LA-ICPMS - Laser ablation-inductively coupled plasma mass spectrometry

LASS - Laser ablation split stream

LILE- Large ion lithophile elements

LREE-Light rare earth elements

MAD02- Madagascar apatite

MAF - Micro Analysis Facility

MC-ICPMS - Multi-collector inductively coupled plasma mass spectrometer

MLA-Mineral liberation analysis

MREE- Middle rare earth elemets

Mnz-Monazite

MtAp-Magnetite-apatite

Mt – Magnetite

Ppm- Parts per million

Py - Pyrite

REE - Rare earth elements

RGB- Red-green-blue

Rut-Rutile

Sd-Standard deviation

SEM-Scanning electron microscope

VMS- Volcanogenic massive sulfide

WDS- wavelength-dispersive X-ray spectrometers

Wt %- Weight percent

Xtm-Xenotime

Zr-Zircon

List of Appendices

Appendix A Representative BSE images of apatites from the Animal Pond Prospect, Stog'er Tight and Argyle deposits

Appendix B Representative CL images of apatites from the Animal Pond Prospect, Stog'er Tight and Argyle deposits

Appendix C Mineral liberation analysis (MLA-SEM) of the mounts from the the Animal Pond Prospect, Stog'er Tight and Argyle deposits

Appendix D Summarized methods for EPMA and EPMA average oxide and apfu results of apatite from the Animal Pond Prospect, Stog'er Tight and Argyle deposits

Appendix E Summarized methods for LASS (LA-ICPMS and LA-MC- ICPMS) and trace element results of apatite from the Animal Pond Prospect, Stog'er Tight and Argyle deposits

Appendix F Nd results for apatite grains from LASS, and calculation of $\varepsilon_{Nd}(t)$

Chapter 1: Introduction to the gabbro hosted orogenic gold deposits in Baie Verte, Newfoundland, Canada

The Baie Verte Peninsula hosts numerous orogenic gold occurrences, primarily within the Lower Ordovician volcanic cover sequences (Snooks Arm Group) and the ophiolitic rocks of the Baie Verte oceanic tract. The region hosts three known gabbro-hosted orogenic deposits: the Stog'er Tight deposit, the Argyle deposit, and the Animal Pond prospect. All the deposits are located in the hanging wall of the Scrape thrust fault at various distances from the thrust front, but typically within 100s of meters of the surface trace of the fault (Ramezani et al., 2000; Evans, 2004; Castonguay et al., 2009; Skulski et al., 2009, 2010; Ybarra et al., 2017; Pawlukiewicz, 2019). Gold mineralization in all three areas is associated with coarse-grained, pegmatoidal gabbros that are variably deformed and metasomatically altered by orogenic Au-related hydrothermal fluids. The original igneous rocks contain primary igneous apatite that was subsequently partially to fully replaced during later metasomatic alteration to produce secondary monazite and xenotime and that is spatially associated with hydrothermal zircon. This thesis project investigates apatite textures, mineral chemistry, and radiogenic isotope signatures to monitor igneous and hydrothermal processes recorded in the Baie Verte gabbro-hosted Au deposits. We use a multi-method approach comprising petrography, mineral liberation analysis (MLA), cathodoluminescence (CL) microscopy, scanning electron microscopy (SEM) CL and back-scattered electron (BSE) imaging, electron microprobe analysis (EPMA), laser ablation inductively coupled plasma mass spectrometry (LA-ICP-MS) for

trace element analysis, and laser ablation multi-collector inductively coupled plasma mass spectrometry (LA-MC-ICP-MS) for Sm-Nd analysis. The goals of this project are to: 1) understand the textural, chemical, and isotopic evolution of the primary igneous and secondary hydrothermally influenced apatite; 2) document the apatite paragenesis; 3) utilize apatite U-Pb ages to better understand the timing and evolution of the orogenic Au mineralization in the Baie Verte Peninsula; 4) use CL imaging, chemical, and isotopic differences in the apatite to evaluate the potential of apatite to be a tracer of magmatic and hydrothermal processes; and 5) establish whether apatite chemistry and isotopic signatures can be used as a vector for orogenic Au deposits. The following sections provide a general overview of orogenic gold deposits, the geologic setting of the deposits in the Baie Verte Peninsula, and the proposed methodology for the thesis.

1.1. Orogenic Gold Deposits

The following synthesis is based on papers by Groves et al. (1998) and Dube & Gosselin (2007). Orogenic gold deposits are epigenetic, structurally controlled deposits that generally occur in deformed and metamorphosed greenstone belts (Fig. 1.1). These deposits occur in regionally metamorphosed terranes of all ages. The deposit type is also known as quartz-carbonate vein deposits or lode gold deposits. Orogenic Au deposits are associated with greenschist facies rocks as has been observed throughout Archaean greenstone belts globally and Proterozoic-Phanerozoic metamorphic belts. However, some major deposits (e.g., Sigma-Lamaque, Québec; Kolar, India; Mt. Charlotte, Australia) are found in higher metamorphic grade Archaean terranes (McCuaig et al., 1993). In Canada, orogenic Au deposits represent the main source of gold and are found

primarily in the Archean greenstone belts of the Superior and Slave provinces. Deposits of this type have also been reported in the Paleozoic greenstone and metasedimentary terranes of the Appalachian orogen and in the oceanic terranes of the Cordillera (Dube & Gosselin, 2007).

Orogenic gold can occur in varying lithologies, including felsic plutonic rocks, banded iron formations, mafic volcanic rocks, and metasedimentary rocks (Groves et al., 2003; Goldfarb and Groves, 2015). The deposits generally occur in brittle-ductile shear zones and faults, and they contain quartz and quartz-carbonate veins, with variable amounts of Au and Ag present in both the veins and the wall rock. Structural controls of these vein systems can be highly variable in terms of type and geometry. Stockwork and hydrothermal breccia veins may develop depending on the geological and structural environment (Robert et al., 1994; Robert and Poulsen, 2001). The presence of rigid granitic intrusions can cause significant variations in the orientation and slip directions in shear zones developed within the intrusions; therefore, competency contrast can have a major influence on the distribution and geometry of the associated quartz-carbonate vein network (Dubé and Gosselin, 2007). In most cases, deposits are spatially associated with regional scale structures, often terrane boundaries, but the deposits themselves are hosted by subsidiary structures (e.g., 2nd or 3rd order faults off of major regional fault systems; Dubé and Gosselin, 2007).

The major gangue minerals in orogenic Au deposits are quartz and carbonates (calcite, dolomite, ankerite, and siderite; Groves et al., 1998). Minor gangue phases include white mica, chlorite, tourmaline and scheelite that are commonly associated with

hydrothermal alteration in orogenic deposits (Groves et al., 1998). Orogenic Au deposits contain varying amounts of Au with or without Ag, As, W, B, Sb, Te, and Mo, and typically with background or low concentrations of base metals (e.g., Cu, Pb, and Zn; Dubé and Gosselin, 2007). The main ore minerals are native gold, decreasing amounts of pyrite, pyrrhotite, arsenopyrite, and chalcopyrite, and commonly, there is no significant vertical mineralogical or metal zoning (Dubé and Gosselin, 2007). These deposits are characterized by sulfide mineralogy that reflects the lithogeochemistry of the host. While arsenopyrite commonly represents the main sulfide in metasedimentary rocks, pyrite or pyrrhotite are the dominant sulfide in metamorphosed igneous rocks (Groves et al., 1988). Some deposits, such as those hosted by syenites in the Kirkland Lake area, contain trace quantities of molybdenite and tellurides (Thompson et al., 1950).

Greenstone-hosted orogenic Au deposits, like those in Baie Verte, Newfoundland, are predominantly hosted by greenschist to lower amphibolite facies mafic metamorphic rocks and were formed at medium crustal depths (5-10 km; Fig 1.2; Dubé and Gosselin, 2007). Veins in greenstone-associated orogenic Au deposits are hosted in diverse lithologies: mafic and ultramafic volcanic rocks (e.g., Timmins; Kerr-Addison; Dubé and Gosselin, 2007), competent Fe-rich gabbroic sills (e.g., Stog'er Tight, Golden Mile; Phillips et al., 1986; Ramezani, 1992), or granitoid intrusions (e.g., Granny Smith; Dubé and Gosselin, 2007).

The mineralized structures and associated alteration zones occur 10s to 100s of meters from the main controlling structures and generally narrow the deeper in the crust the mineralization formed (Groves et al., 1988). Greenstone-hosted deposits typically

have abundant carbonate alteration dominated by Fe-carbonates like ankerite and siderite but can also contain dolomite or calcite (Groves et al., 1988). Potassium metasomatism commonly results in sericite alteration, lesser fuchsite, biotite, K-feldspar, and/or albite. Chlorite occurs in some deposits. At deeper crustal levels, actinolite or diopside form, and carbonate minerals are found in lesser amounts (Groves et al., 1988). Sulfidation of wall rocks is common in deposits hosted by banded iron formation (BIF) and Fe-rich host rocks (Groves et al., 1988). Wall rock alteration is accompanied by the addition of significant amounts of CO_2, S, K, H_2O, SiO_2, ± N, and large ion lithophile elements (LILE).

Although the potential sources of ore-forming fluids in orogenic gold deposits remain a matter of debate due to the overlap of H and O isotope values of igneous and metamorphic fluids (Ridley and Diamond 2000), most studies support the metamorphic dehydration model (Phillips and Groves, 1983; Robert and Kelly, 1987; Kerrich, 1989; Goldfarb et al., 1991; Groves et al., 1993; Phillips and Powell, 2010; Groves et al., 2019), while others argue for the magmatic-hydrothermal fluids model (Giggenbach, 1986; Sillitoe, 1989; Sillitoe and Bonham Jr, 1990; Spooner, 1993). The metamorphic fluids are produced in the mid- to lower crust at the transition between greenschist to amphibolite facies and are mobilized towards higher crustal levels along large-scale faults and deformation zones (Groves et al., 1988). During their migration through the crust the fluids sequentially dissolve Au and other elements and subsequently precipitate Au due to pressure changes and/or reaction with wall rocks (Mikucki, 1998).

In orogenic gold systems, ore fluids comprise H_2O-CO_2 ±CH_4, have a low salinity and a pH of 5.5. At temperatures up to 350°C, the most important gold transporting complex is HS-, with Au (HS)° dominating at lower pH and Au $(HS)_2^-$ dominating at higher pH, while $AuCl_2^-$ dominates at higher temperatures (>350 °C) (Fig. 1.3; Mikucki, 1998; Williams-Jones et al., 2009; Goldfarb and Groves, 2015). Calculations show that $AuCl_2$ complexes are thermodynamically stable at temperatures >350°C, low pH, and high oxygen fugacity (fO_2), but the pH of orogenic gold fluids is commonly near neutral, therefore Au $(HS)_2^-$ remains the dominant transport species (Mikucki, 1998; Ridley and Diamond, 2000; Williams-Jones et al., 2009).

1.2. Exploration History

The Baie Verte Peninsula in Newfoundland hosts numerous gold occurrences (Evans, 2004). Until the 1980s, Au in Newfoundland was mainly produced as a by-product of the mining of volcanogenic massive sulfide (VMS) deposits (Evans, 2004; Skulski et al., 2009); however, more recently fault-associated orogenic Au deposits on the peninsula (e.g., Nugget Pond, Pine Cove, Stog'er Tight, Argyle all located in the Mings Bight – Point Rousse area) have become significant Au producers (Lavigne, 1993; Dimmell and Hartley, 1991; Ramezani, 1992; Piercey and Copeland, 2017).

Gold mineralization in the Baie Verte Peninsula is mainly hosted by Lower Ordovician ophiolitic rocks and submarine volcano-sedimentary rocks of the Baie Verte oceanic tract (BVOT; Williams et al., 1988; Bédard et al., 1998; Evans, 2004; van Staal, 2007). Orogenic gold deposits in the BVOT include Nugget Pond (Swinden et al.,1990),

Pine Cove (Dimmell and Hartley, 1991), Deer Cove (Patey and Wilton, 1993), Romeo & Juliet (Meade et al., 1998), Stog'er Tight (Ramezani, 1992; Ramezani et al., 2000), and Argyle (Piercey and Copeland, 2017).

Stog'er Tight was discovered in the 1980s by the Noranda Exploration Company Ltd. during a soil geochemistry survey (Ramezani, 1992). In the following years, seven gabbro-hosted mineralized zones (Gabbro Zone, Gabbro West, Gabbro East, Cliff Zone, West Zone, South Zone, and East Zone; Fig.1.4) were discovered through geochemical, geological, and geophysical surveys and a drilling campaign (Evans, 2004). In 1996, Ming Minerals Inc. took over the property from Noranda, producing 30,735 tons of gold-bearing bulk samples; the project was abandoned due to a lower-than-expected gold grade (Cullen et al., 2018). A supplementary trenching and drilling program was carried out by Tenacity Gold Mining Company Ltd. in 2006, resulting in an indicated resource estimate of 96,000 t @ 7.04 g/t Au and an inferred resource estimate of 53,000 t @ 5.75 g/t Au (Cullen et al., 2018). In 2012, 1512513 10Alberta Ltd. purchased the Stog'er Tight Mining Lease and optioned it to Anaconda Mining (Cullen et al., 2018). At the Stog'er Tight deposit, a total of 18,074 m in 282 diamond drill holes was drilled since its discovery (Cullen et al., 2018). Anaconda's regional exploration focused on gold mineralization hosted in gabbros similar to those at Stog'er Tight. Kuntz et al. (2021) defined an initial National Instrument (NI) 43-101 mineral resource estimate for the Stog'er Tight deposit at 642,000 t @ 3.02 g/t Au indicated, and 53,000 t @ 5.63 g/t Au inferred.

The Argyle deposit is located ~2 km northeast of the Stog'er Tight deposit within the hanging wall of the Scrape thrust and is associated with gabbros that are similar to those hosting the Stog'er Tight deposit. Gold mineralization at Argyle was discovered by Anaconda Mining Inc. in 2012 through prospecting guided by geochemical soil surveys. Anaconda completed 35 diamond drill holes totaling 1,835 m at the Argyle Deposit since August 2020 (Kuntz et al., 2021). A mineralized zone with associated hydrothermal alteration extends over a strike length of 675 m and 225 m down-dip with encouraging assay results, which included: 2.83 g/t gold over 10.0 m (AE-20-160), 5.72 g/t gold over 7.0 m (AE-21-184), 2.16 g/t gold over 14.0 m (AE-21-185), 5.25 g/t gold over 6.0 m (AE-21-169) and 1.04 g/t gold over 8.0 m (AE-21-174;Fig. 1.5; Kuntz et al., 2021). An initial (NI) 43-101 mineral resource estimate for Argyle deposit in 2021 defined an indicated mineral resource of 436,800 t @ 2.53 g/t Au and an inferred mineral resource of 500 t @ 2.77 g/t Au (Kuntz et al., 2021).

1.3. Regional Geology and Tectonic Evolution

The island of Newfoundland is a part of the Paleozoic Appalachian-Caledonian Orogenic Belt. Williams (1979, 1995), Williams et al. (1988) and Williams and Grant (1998) divided Newfoundland into four tectonostratigraphic zones, where each zone represents spatially and geologically distinct regions that were amalgamated during Appalachian orogenesis. These tectonostratigraphic zones are (from west to east) the Humber, Dunnage, Gander and Avalon zones (Fig. 1.6a).

The Humber Zone represents the remnants of Laurentia's Appalachian margin, which was involved in the Paleozoic orogenic events (e.g., Williams, 1979). The Dunnage Zone comprises the remnants of accreted continental and oceanic arc terranes that formed within the realm of the Iapetus Ocean (van Staal, 2007). The Dunnage Zone has been divided into two subzones based on provenance: the peri-Laurentian Notre Dame and the peri-Gondwanan Exploits Subzones (Williams et al., 1988). The Gander and Avalon zones are peri-Gondwanan microcontinents that crossed the Iapetus Ocean and were accreted to the Laurentian margin, along with remnants of the Iapetus Ocean, from the Ordovician to the Middle Devonian (~470-380 Ma; van Staal, 2007).

The Humber Zone, extending over western Newfoundland and southern Quebec, represents the ancient passive continental margin of North America (Laurentia), on to which subsequent terranes were accreted, and it consists of shelf-facies carbonate and siliciclastic rocks deposited upon a crystalline Precambrian basement (Williams 1979; Williams and Hiscott, 1987). The Dunnage Zone, situated between the Humber and Gander zones, is best preserved in Newfoundland, but significant segments are also exposed in New Brunswick and Southern Quebec (van Staal, 2007). It represents the remnants of the ancient Iapetus Ocean, and it contains ophiolites, volcanic, volcaniclastic, and sedimentary rocks of island arc and back-arc origins (Williams, 1979; Williams et al., 1988; van Staal, 2007; van Staal and Barr, 2012).

The Dunnage Zone is bordered to the west by the Baie Verte-Brompton line (BVBL; Baie Verte line or BVL in Newfoundland) and to the east by the GRUB Line (Gander River ultrabasic belt) and subdivided into the Notre Dame and the Exploits

subzones that formed on the opposite sides of the Iapetus Ocean (Williams, 1979; Williams et al., 1988). The Notre Dame Subzone terranes were accreted to the Laurentian margin during the Cambrian-Ordovician Taconic orogeny, whereas the Exploits Subzone terranes were accreted to the Gander margin during the Early Ordovician Penobscot orogeny (van Staal, 2007; van Staal et al., 2012). The Exploits and Notre Dame Subzones were amalgamated along the Mekwe'jit Line during the Silurian Salinic orogeny (White and Waldron, 2022).

The Baie Verte Peninsula consists of two distinct tectonostratigraphic belts, the Humber Zone, and the Notre Dame Subzone of the Dunnage Zone that are divided by the BVL, a complex brittle-ductile shear zone with ophiolite along slivers its length (Williams, 1979; Williams and St Julien, 1982; Castonguay et al., 2014).

The juxtaposition and amalgamation of Newfoundland's four main tectonostratigraphic zones played a crucial role in the formation of orogenic gold deposits in the region. The accretion of the leading edge of Ganderia to Laurentia in the Silurian caused Salinic orogenesis, whereas the Devonian merger of Avalonia and composite Laurentia led to the Acadian orogenesis and the subsequent closure of the Acadian Seaway (van Staal, 2007; van Staal et al., 2012). Orogenic gold deposits in the region are interpreted to form as a consequence of these younger Silurian-Devonian orogenic events (van Staal, 2007; van Staal et al., 2012).

1.4. Geology of the Baie Verte Peninsula

The Baie Verte Peninsula is located on Newfoundland's northern coast and represents the northernmost land exposure of the Appalachian Dunnage Zone. The Baie Verte Peninsula comprises both the Humber Zone and Notre Dame Subzone of Dunnage zone (Fig.1.6a; Williams, 1979; Williams and St. Julien, 1982; Castonguay et al., 2014). The two contrasting and distinct tectonostratigraphic belts are separated by the BVBL/BVL. The BVL is a complex fault zone oriented north-northeast to east that juxtaposes the oceanic terrane of the Notre Dame Subzone with the continental rocks of the Humber Zone (Hibbard, 1983). To the west of the BVL, the Humber Zone consists of the East Pond Metamorphic Suite, which includes deformed schists and gneisses, overlain by Fleur de Lys Supergroup metaclastic rocks, which contains pelite, amphibolite, and schist that were derived from continental margin sedimentary rocks (Hibbard, 1983). The East Pond Metamorphic Suite rocks are the Grenvillian crystalline basement (Hibbard, 1983; Skulski et al., 2010).

Rocks located east of the BVL belong to the Notre Dame Subzone and include: 1) Cambro-Ordovician ophiolitic sequences; 2) Ordovician volcanic cover rocks; 3) Silurian terrestrial volcanic and sedimentary rocks unconformably overlying Ordovician sequences; and 4) Siluro-Devonian intrusive rocks (Evans, 2004; van Staal, 2007; Skulski et al., 2009; van Staal and Barr, 2012). The ophiolite suites include the Advocate Complex, the Point Rousse Complex, the Betts Cove Complex and Pacquet Complex (Fig. 1.5b, Hibbard, 1983; Skulski et al., 2010). All ophiolite sequences in the Baie Verte Peninsula are well correlated and include the rocks of the Betts Cove ophiolite (489 Ma) and the volcanic cover sequence of the Snooks Arm Group (<487 Ma to 467 Ma; Skulski

et al., 2010). Continental and oceanic terrains on both sides of the BVL are crosscut by mafic to felsic intrusions of Silurian-Devonian age (Cawood and Dunning, 1993; Cawood et al., 1994).

The Pacquet Complex and Point Rousse Complex host various gold deposits in the central part of the Baie Verte Peninsula (Fig. 1.5, Evans, 2004; Skulski et al., 2010). The Pacquet Complex contains rocks correlative with the Betts Cove Complex, but it also contains a rhyolite unit - the Rambler rhyolite formation, which hosts Au-rich VMS mineralization (Skulski et al., 2010). The Point Rousse Complex is an Ordovician ophiolite series, comprising ultramafic and mafic cumulate rocks, gabbros, sheeted dykes, and pillow lava (Norman and Strong, 1975; Kidd et al., 1978) that correlates with the Pacquet Complex and Betts Cove Complex; these are overlain by the Point Rousse cover sequence that consists of jasper-like chert and red magnetite-siltstone iron formation, volcanogenic turbidites, tuff breccia, and volcanic conglomerate that correlate with the Snooks Arm Group (Bédard, 1999; Bédard et al., 2000; Evans, 2004; Skulski et al., 2010; Sparrow et al., 2017).

The Point Rousse Complex is separated from the Pacquet Complex to the south by the Scrape thrust fault (Fig. 1.6b) and to the east it is separated from the metasedimentary rocks of the Mings Bight Group by a high angle fault zone (Hibbard, 1983; Anderson et al., 2001). Orogenic gold mineralization is hosted predominantly in the Snooks Arm Group rocks in the hanging wall of the Scrape thrust fault, which is interpreted to be a splay off of the BVL (Hibbard, 1983; Skulski et al., 2010).

According to Castonguay et al. (2009), the rocks of the Baie Verte Peninsula record at least four deformation events (D_1-D_4). The D_1 deformation occurred as a result of the obduction of Baie Verte oceanic tract ophiolites during the Taconic orogeny but was not well preserved in the ophiolitic and cover sequence rocks due to overprinting by subsequent deformation and metamorphic events (Castonguay et al., 2009). D_2 fabrics are related to north-dipping, south-directed thrust faults and shear zones, are also responsible for general northward dips of units, north-dipping S_2 foliation and downslope, and northward lineations; these are interpreted to be a result of Salinic to Acadian deformation (Castonguay et al., 2009; Sparrow et al., 2017; Skulski et al., 2010). Fabrics associated with the D_3 deformation event are expressed as reclined folds and south sloping extensional shear zones that affected earlier fabrics; they are attributed to transpression associated with Devonian (Acadian) dextral transtension (Anderson et al., 2001). The D_4 deformation consists of underdeveloped cross layers uniformly throughout the peninsula and is marked by north-northeast oriented anticlines and synclines that affect the D_1-D_3 structures and commonly causes doubly plunging features in the earlier structures (Castonguay et al., 2009; Sparrow et al., 2017).

Epigenetic gold occurrences in the Baie Verte Peninsula are hosted in quartz-carbonate veins and wall rock (Evans, 2004). The mineralization is spatially and temporally related to the hanging walls of D_2 thrust sheets, such as the Scrape thrust and the Deer Cove thrust (Kirkwood and Dubé, 1992; Dubé et al., 1993; Evans, 2004; Castonguay et al., 2009, 2014; Skulski et al., 2009, 2010). The spatial association between gold mineralization and Silurian-(Devonian) D_2 faults together with radiometric

age determinations from various deposits, suggest that gold mineralization was coeval with Silurian-(Devonian) orogenesis (Ritcey et al.,1995; Ramezani et al., 2000; Castonguay et. al, 2009; Kerr and Selby, 2012; Castonguay et. al, 2014). This is based on a 420 ± 5 Ma U-Pb date for hydrothermal zircon at Stog'er Tight (Ramezani et al., 2000) and a 420 ± 7 Ma Re-Os date for pyrite from Pine Cove (Kerr and Selby, 2012).

1.5. Stratigraphy

The Animal Pond prospect, Argyle, and Stog'er Tight gold deposits are hosted by Cambro-Ordovician rocks of the Snooks Arm Group in the Point Rousse cover sequence (Bédard, 1999; Bédard et al., 2000; Skulski et al., 2010).

Figure 1.6 shows the pseudo-stratigraphic units for the Baie Verte Peninsula as identified by Skulski et al. (2010) with their characteristics briefly outlined here in vertical succession. The Betts Cove Complex consists of ultramafic cumulate sections overlain by layered gabbros, massive gabbros, sheeted dykes, and low- to intermediate-Ti boninites (Hibbard, 1983; Skulski, 2010). Contrary to Bedard et al. (2000), Skulski et al. (2010) included Mount Misery Formation rocks in the Betts Cove Complex rather than in the Snooks Arm Group. Mount Misery Formation rocks include island-arc tholeiitic pillow basalts and intermediate-Ti boninites (Skulski et al., 2010).

The Snooks Arm Group comprises the Scrape Point Formation, the Bobby Cove Formation, the Venam's Bight Formation, the Balsam Bud Cove Formation, and the Round Harbor Formation (Fig. 1.6, Bédard et al., 2000; Skulski et al, 2010). The Scrape Point Formation, the lowest part of the Snooks Arm Group, is composed of localized

basaltic conglomerate cemented by jasper that is overlain by red siltstone, shale and banded iron formation (Bédard et al., 2000). The Bobby Cove Formation, which overlies the Scrape Point Formation, contains calc-alkaline mafic volcanic rocks including lapilli tuffs and volcanic conglomerates; the East Pond member consists of a calc-alkaline clinopyroxene-phyric tuff that is a marker horizon within the Snooks Arm Group (Skulski et al., 2010). The Venam's Bight Formation is composed of tholeiitic, high-Ti basalts interbedded with volcanic breccias and hematitic mudstones or ironstones (Skulski et al., 2009, 2010; Ybarra et al., 2017). The Balsam Bud Cove Formation comprises felsic tuff, rhyolite, tholeiitic basalt, red and green siltstone, shale, and sandstone (Bédard et al., 2000; Kessler and Bédard, 2000; Skulski et al., 2010). The Round Harbor Formation, at the top of the Snooks Arm Group, contains mostly sheet and pillowed flows of tholeiitic basalt (Bédard et al., 2000).

1.6. Deposit Geology

This thesis focuses on the coarse-grained pegmatoidal gabbroic rocks that host the Animal Pond prospect, and the Stog'er Tight and Argyle deposits. The gabbroic rocks are intruded by mafic volcanic and sedimentary rocks of the Scrape Point and Bobby Cove formations of the Snooks Arm Group, which include massive basalt flows interbedded with green mudstone, tuffs, clinopyroxene-phyric lapilli and crystal tuffs (Bédard et al., 2000; Skulski et al., 2009, 2010). These are cut by variably deformed gabbroic sills and mafic dykes with weak to proto- mylonitic foliation (Bédard, 1999; Bédard et al., 2000; Skulski et al., 2009, 2010; Sparrow et al., 2017). All the deposits are in the hanging wall of the Scrape thrust fault at various distances from the thrust front, but commonly within

100s of meters of the surface trace of the fault (Ramezani et al., 2000; Evans, 2004; Castonguay et al., 2009; Skulski et al., 2009, 2010; Ybarra et al., 2017; Pawlukiewicz, 2019).

The volcaniclastic cover sequence at Stog'er Tight is cut by three distinct gabbroic sills that are between 11-70 m thick (Kirkwood and Dubé, 1992; Ramezani et al., 2000). The gabbros have variable amounts of plagioclase, amphibole, pyroxene, ilmenomagnetite, apatite, and zircon (Ramezani et al., 2000; Piercey and Copeland, 2017). The sills have slightly to moderately sheared contacts to the south and chilled contacts to the north (Kirkwood and Dubé, 1992). Stog'er Tight gabbro is characterized by an elevated concentration of ilmenomagnetite compared with barren Fe-Ti-poor gabbro sills to the north (Ramezani et al., 2000).

Gold mineralization in Stog'er Tight is mainly hosted by gabbroic sills within the Point Rousse cover sequence within the hanging wall of the Scrape thrust fault; the host gabbro was dated at 483 +3/-2 Ma (2σ) using multi-grain zircon isotope dilution-thermal ionization mass spectrometry (ID-TIMS) U-Pb geochronology (Ramezani, 1992). In subsequent years, geochemical, geological, and geophysical surveys outlined seven similar gabbro-hosted mineralized zones, including the Gabbro Zone, Gabbro West, Gabbro East, Cliff Zone, West Zone, South Zone and East Zone (Evans, 2004).

Ramezani (1992) defined four alteration zones in Stog'er Tight: 1) chlorite-calcite; 2) ankerite-sericite; 3) chlorite-magnetite; and 4) red albite-pyrite (± gold). In Stog'er Tight, gold often occurs as micro-veinlets and disseminated blebs within coarse

pyrite aggregates (Ramezani et al., 2000). The highest gold grades in Stog'er Tight are associated with coarse, mottled pyrite (Copeland et al., 2015).

Altered mafic rocks at Stog'er Tight also contain hydrothermal zircon, which Ramezani (1992) dated at 420±5 Ma U–Pb age, inferring that this was the age of gold mineralization. Based on samples that are essentially devoid of common Os, direct dating using the Re-Os technique on pyrite separates in correlative rocks at Pine Cove revealed an age between 419 Ma and 404 Ma (Kerr and Selby, 2012), which is consistent with the previous result.

The units hosting the Argyle deposit are generally east-west striking, dip moderately to the north-northwest, and occur in the hanging wall of the Scrape thrust, which outcrops 200-300 m to the south of the deposit (Sparrow et al., 2017). Gold mineralization at Argyle is hosted in a 50 m thick Fe-Ti-rich gabbroic sill, which is similar in age to the Ordovician (483 Ma +3/-2 U-Pb zircon age) suite of gabbroic rocks dated by Ramezani (1992) at Stog'er Tight (Piercey and Copeland, 2017). The mineralization has a strike length of 685 m and is defined down-dip for 225 m (Sparrow et al., 2017).

The Argyle deposit is hosted by a gabbro with varying textures like those found at Stog’er Tight. At contacts with the volcaniclastic rocks, the gabbro is aphanitic or displays fine-grained chilled margins, and locally, proximal to the mineralization, the gabbro is pegmatoidal with large feldspars (Pawlukiewicz, 2019). Gold mineralization

occurs in the coarsest, pegmatoidal gabbros and is spatially linked to the presence of coarse-grained Fe-Ti minerals (Pawlukiewicz, 2019).

Gold mineralization at the Argyle deposit is associated with altered, quartz-veined and pyritized gabbro where gold is associated with coarse, mottled pyrite similar to Stog'er Tight (Piercey and Copeland, 2017). Gold mineralization in the Argyle deposit is interpreted to have formed by wall rock sulfidation and is commonly found within 1 m of the quartz-carbonate vein margins (Pawlukiewicz, 2019). The gabbroic host rocks have an approximately symmetrical alteration zone (30 to 70 m) with a distinct distal to proximal mineralization zonation that occurs as zones of: 1) patchy epidote-albite-magnetite; 2) epidote-albite-chlorite; 3) epidote-albite-chlorite-rutile; and 4) pervasive albite-muscovite-Fe-carbonate-black chlorite ± pyrite-gold and quartz veins (Piercey and Copeland, 2017; Sparrow et al., 2017).

Gold occurs in the most altered zones and is associated with sooty black tarnished, inclusion-rich subhedral to euhedral pyrite crystals and is typically found as fine inclusions within pyrite crystals, on pyrite grain margins, or in fractures (Piercey and Copeland, 2017; Sparrow et al., 2017). The Argyle deposit contains trace levels of disseminated euhedral pyrite crystals in all units and alteration assemblages (Pawlukiewicz, 2019). The highest gold grades are associated with late black chlorite veinlets (Pawlukiewicz, 2019).

The Animal Pond prospect is hosted by weakly altered gabbro, and it is likely the least altered compared to the Argyle and Sto'ger Tight gabbros (Piercey, unpublished

report). The gabbro displays a variety of textures, including oikocrystic clinopyroxene, locally it contains abundant magnetite, and can be fine-grained, feldspar-rich pegmatoidal, or medium-grained with cumulate textures (Piercey, unpublished report).

1.7. Analytical Methods

Thin sections of all collected samples were studied by polarized, reflected and cathodoluminescence (CL) petrography for an assessment of the mineral paragenesis, the extent of alteration and the presence of apatite. Cathodoluminescence (CL) and back-scattered electron (BSE) imaging was performed on a scanning electron microscope (SEM) to reveal the abundance and physical properties of apatite, including shape, size, color, and luminescence. A bench-top optical microscope-based system was used to obtain CL images of apatite grains. Mineral liberation analysis (MLA) was also performed on mounts to obtain the sizes and shapes of grains and their spatial relationships in the mounts and to gold.

Major and minor elements in apatite were measured using an electron probe microanalyzer (EPMA), trace elements concentrations were analyzed using laser ablation inductively coupled plasma mass spectrometry (LA-ICPMS), and Sm-Nd in apatite was measured using laser ablation multi-collector inductively coupled plasma mass spectrometry (LA-MC-ICPMS).

All analyses were performed in the Micro Analysis Facility (CREAIT) and in the Department of Earth Sciences (TERRA) at Memorial University of Newfoundland.

1.8. Co-authorship statement

The design of this research project is credited to Dr. Stephen Piercey. The author conducted all primary research activities including sample preparation, optical microscopy and data reduction. CL imaging was conducted by the author with assistance from Dr. John Hanchar. SEM imaging and EPMA analyses were conducted by the author under the supervision of Dr. Wanda Aylward. The author did the LASS analyses and data reduction with assistance from Dr. Rebecca Lam and Dr. Markus Wälle. The primary editor of this thesis is Dr. Stephen Piercey, with secondary editing by Dr. Gregory Dunning.

1.9. Presentation

This thesis consists of three chapters with supplementary appendices. Chapter 1 introduces overall topic that provides background information about the regional and local geology, previous work on the deposit, and the objectives of this thesis.

Chapter 2 is the main body of the thesis that focuses on understanding the textural, chemical, and isotopic evolution of the primary and secondary apatite and details the multi-method approach that involves petrography, CL microscopy, CL and BSE imaging using SEM, MLA, EPMA analyses for major and minor elements, LA-ICPMS analyses of trace element composition of apatite, LA-MC-ICPMS analyses of Sm-Nd in apatite. Chapter 2 will be submitted as a manuscript to an international peer-reviewed journal.

Chapter 3 will summarize the results of the research and set the direction for potential future research.

1.10. References

Anderson, S., Jamieson, R. A., Reynolds, P., and Dunning, G., 2001, Devonian extension in northwestern Newfoundland: 40Ar/39Ar and U-Pb data from the Ming's Bight area, Baie Verte Peninsula: Journal of Geology, v. 109, p. 191–211.

Bédard, J. H., 1999, Petrogenesis of boninites from the Betts Cove ophiolite, Newfoundland, Canada: identification of subducted source components: Journal of Petrology, v. 40, p. 1853–1889.

Bédard, J. H., Lauziere, K., Tremblay, A., and Sangster, A., 1998, Evidence for forearc seafloor spreading from the Betts Cove ophiolite, Newfoundland: oceanic crust of boninitic affinity: Tectonophysics, v. 284, p. 233–245.

Bédard, J. H., Lauziere, K., Tremblay, A., Sangster, A. L., Douma, S., and Dec, T., 2000, Betts Cove ophiolite and its cover rocks: Geological Survey of Canada Bulletin, v. 550, 76 p.

Castonguay, S., Skulski, T., van Staal, C., and Currie, M., 2009, New insights on the structural geology of the Pacquet Harbour Group and Point Rousse Complex, Baie Verte Peninsula, Newfoundland: Newfoundland and Labrador Department of Natural Resources, Geological Survey, Report 09-1, p. 147–158.

Castonguay, S., van Staal, C. R., Joyce, N., Skulski, T., and Hibbard, J. P., 2014, Taconic metamorphism preserved in the Baie Verte Peninsula, Newfoundland Appalachians: Geochronological evidence for ophiolite obduction and subduction

and exhumation of the leading edge of the Laurentian (Humber) margin during closure of the Taconic Seaway: Geoscience Canada, v. 41, p. 459–482.

Cawood, P.A., and Dunning, G.R., 1993, Silurian age for movement on the Baie Verte Line: implications for accretionary tectonics in the Northern Appalachians. Geological Society of America, Abstracts with Programs, v. 25, p. A422.

Cawood, P.A., Dunning, G.A., Lux, D., and van Gool, J.A.M., 1994, Timing of peak metamorphism and deformation along the Appalachian margin of Laurentia in Newfoundland: Silurian, not Ordovician: Geology, v. 22, p. 399–402.

Copeland, D. A., Pitman, C., Evans, D. T. W., McNeill, P., and Slepcev, G., 2015, Mineral resource and mineral reserve update on the Pine Cove Mine and mineral resource estimate on the Stog'er Tight deposit, Point Rousse Project Baie Verte, NI-43-101 Technical Report: Anaconda Mining Inc., Newfoundland and Labrador, Canada, 249 p.

Cullen, M., Pitman, C., Copeland, D. A., McNeill, P., and Slepcev, G., 2018, Mineral resource and mineral reserve update on the Point Rousse Project, Baie Verte, Newfoundland and Labrador, Canada, NI-43-101 Technical Report: Anaconda Mining Inc., Newfoundland and Labrador, Canada, 285 p.

Dimmell, P. and Hartley, C., 1991, Gold mineralization and exploration of the Pine Cove property, Baie Verte Peninsula. In Ore Horizons, Volume 1. Edited by H.S. Swinden and A. Hogan: Newfoundland Department of Mines and Energy, Geological Survey Branch, p. 51-62.

Dubé, B. and Gosselin, P., 2007, Greenstone-hosted quartz-carbonate vein deposits: in Goodfellow, W. D., ed., Mineral deposits of Canada: A Synthesis of Major Deposit-Types, District Metallogeny, the Evolution of Geological Provinces and Exploration Methods: Geological Association of Canada, Mineral Deposits Division, Special Publication No. 5, p. 49–73.

Dubé, B., Lauzière, K., and Poulsen, H. K., 1993, The Deer Cove deposit: an example of "thrust"- related breccia-vein type gold mineralization in the Baie Verte Peninsula, Newfoundland: Geological Survey of Canada, Current Research, Paper 93-1D, p. 1–10.

Evans, D. T. W., 2004, Epigenetic gold occurrences, Baie Verte Peninsula, (NTS 12H/09, 16 and 12I/01) Newfoundland: Government of Newfoundland and Labrador, Department of Natural Resources, Geological Survey, Mineral Resource Report No. 11, 157 p.

Giggenbach, W. F., 1986, The use of gas chemistry in delineating the origin of fluids discharged over the Taupo volcanic zone: a review: in International Volcanological Congress, Proceedings Symposium, Hamilton, New Zealand, v. 5, p. 47-50.

Goldfarb, R. J. and Groves, D. I., 2015, Orogenic gold: common or evolving fluid and metal sources through time: Lithos, v. 233, p. 2–26.

Goldfarb, R. J., Snee, L. W., Miller, L. D., and Newberry, R. J., 1991, Rapid dewatering of the crust deduced from ages of mesothermal gold deposits: Nature, v. 354, p. 296–298.

Groves, D. I., 1993, The crustal continuum model for late-Archaean lode-gold deposits of the Yilgarn block, Western Australia: Mineralium Deposita, v. 28, p. 366–374.

Groves, D. I., Goldfarb, R. J., Gebre-Mariam, M., Hagemann, S. G., and Robert, F., 1988, Orogenic gold deposits: a proposed classification in the context of their crustal distribution and relationship to other gold deposit types: Ore Geology Reviews, v. 13, p. 7-27.

Groves, D. I., Goldfarb, R. J., Robert, F., and Hart, C. J. R., 2003, Gold deposits in metamorphic belts: overview of current understanding, outstanding problems, future research, and exploration significance: Economic Geology, v. 98, p. 1–29.

Groves, D. I., Santosh, M., Deng, J., Wang, Q., Yang, L., and Zhang, L., 2019, A holistic model for the origin of orogenic gold deposits and its implications for exploration: Mineralium Deposita, v. 54, p. 1-18.

Hibbard, J., 1983, Geology of the Baie Verte Peninsula, Newfoundland: Government of Newfoundland and Labrador, Department of Mines and Energy, Mineral Development Division, Memoir 2, 280 p.

Kerr, A. and Selby, D., 2012, The timing of epigenetic gold mineralization on the Baie Verte Peninsula, Newfoundland, Canada: new evidence from Re-Os pyrite geochronology: Mineralium Deposita, v. 47, p. 325–337.

Kerrich, R., 1989, Archean gold: relation to granulite formation or felsic intrusions?: Geology, v. 17, p. 1011-1015.

Kessler, L. G., and Bédard, J. H., 2000, Epiclastic volcanic debrites-evidence of flow transformations between avalanche and debris flow processes, Middle Ordovician, Baie Verte Peninsula, Newfoundland, Canada: Precambrian Research, v. 101, 135-161.

Kidd, W. S. F., Dewey, J. F., and Bird, J. M., 1978, The Mings Bight ophiolite complex, Newfoundland: Appalachian oceanic crust and mantle: Canadian Journal of Earth Sciences, v.15, p. 781-804.

Kuntz, G., Robinson, J., McNeill, P., Bullock, K., and Budgell C., 2021, Mineral resource and mineral reserve update on the Point Rousse Project, Baie Verte, Newfoundland and Labrador, Canada, NI-43-101 Technical Report: Anaconda Mining Inc., Newfoundland and Labrador, Canada, 271 p.

Lavigne, J., 1993, The geology and geochemistry of gold mineralization in the Betts Big Pond area, Newfoundland, unpublished M.Sc. thesis, University of Ottawa, Canada. 214 p.

McCuaig, T.C., Kerrich, R., Groves, D.I., Archer, N., 1993, The nature and dimensions of regional and local gold-related hydrothermal alteration in tholeiitic metabasalts in the Norseman goldfields: the missing link in a crustal continuum of gold deposits?: Mineralium Deposita, v. 28, p. 420–435.

Meade, J., Evans, D.T.W. and Wilton, D.H.C., 1998, Romeo and Juliet Prospect, Baie Verte Peninsula, Newfoundland: Newfoundland Department of Mines and Energy, Geological Survey, Report 98-1, p. 77-83.

Mikucki, E. J., 1998, Hydrothermal transport and depositional processes in Archaean lode-gold systems: A review: Ore Geology Reviews, v. 13, p. 307–321.

Norman, R. E. and Strong, D. F., 1975, The geology and geochemistry of ophiolitic rocks exposed at Ming's Bight, Newfoundland: Canadian Journal of Earth Sciences, v. 12, p. 777-797.

Patey, K.S. and Wilton, D.H.C., 1993, The Deer Cove deposit, Baie Verte Peninsula, Newfoundland, a Paleozoic mesothermal lode-gold occurrence in the northern Appalachians. Canadian Journal of Earth Sciences, v. 30, p.1532-1546.

Pawlukiewicz, M., 2019, Hydrothermal Reconstruction and Lithogeochemistry of the Argyle Orogenic Gold Deposit, Baie Verte, Newfoundland, Canada, MSc thesis, Memorial University of Newfoundland, St. John's, NL, Canada, 421 p.

Phillips, G. N., and Groves D. I., 1983, The nature of Archaean gold-bearing fluids as deduced from gold deposits of western Australia: Journal of the Geological Society of Australia, v. 30, p. 25–39.

Phillips, G. N., Groves, D. I., Neall, F. B., Donnelly, T. H., Lambert, I. B., 1986, Anomalous sulfur isotope compositions in the Golden Mile, Kalgoorlie: Economic Geology, v. 81, p. 2008-2015.

Phillips, G. N., Powell, R., 2010, Formation of gold deposits: a metamorphic devolatilization model, Journal of Metamorphic Geology, v. 28, p. 689-718.

Piercey, S. J. and Copeland, D. A., 2017, Host-rock reactivity in the generation of gabbro-hosted orogenic Au in the Baie Verte Peninsula, Newfoundland, Canada: GAC-Newfoundland and Labrador Section, 2017 Spring Technical Meeting, Program with Abstracts, St. John's, Newfoundland, v. 53, p. 250.

Ramezani, J., 1992, The geology, geochemistry and U-Pb geochronology of the Stog'er Tight Gold Prospect, Baie Verte Peninsula, Newfoundland. M.Sc. thesis, Memorial University of Newfoundland, St. John's, Newfoundland, 312 p.

Ramezani, J., Dunning, G. R., and Wilson, M. R., 2000, Geologic setting, geochemistry of alteration, and U-Pb age of hydrothermal zircon from the Silurian Stog'er Tight Gold Prospect, Newfoundland Appalachians, Canada: Exploration and Mining Geology, v. 9, p. 171-188.

Robert, F., and Kelly, W.C., 1987, Ore-forming fluids in Archean gold-bearing quartz veins at Sigma mine, Abitibi greenstone belt, Quebec, Canada: Economic Geology, v. 82, p. 1464-1482.

Robert F. and Poulsen K.H., 2001, Vein formation and deformation in greenstone gold deposits: Reviews in Economic Geology, v. 14, p. 111-155.

Robert, F., Poulsen, K.H., and Dubé, B., 1994, Structural analysis of lode gold deposits in deformed terranes and its application: Geological Survey of Canada, Short course notes, Open File Report 2850, 140 p.

Sillitoe, R. H., 1989, Gold deposits in western pacific island arcs: the magmatic connection: Economic Geology Monograph, v. 6, p. 274–291.

Sillitoe, R. H., and Bonham Jr., H. F., 1990, Sediment-hosted gold deposits: Distal products of magmatic-hydrothermal systems: Geology, v. 18, p. 157–161.

Skulski, T., Castonguay, S., van Staal, C. R., Rogers, N., McNicoll, V., Kerr, A., and Escayola, M., 2009, Baie Verte Peninsula: an evolving geological story: Geological Association of Canada, Newfoundland and Labrador Section, Annual Field Trip Guide, St. John's, Newfoundland, 60 p.

Skulski, T., Castonguay, S., McNicoll, V., van Staal, C., Kidd, W., Rogers, N., Morris, W., Ugalde, H., Slavinski, H., and Spicer, W., 2010, Tectonostratigraphy of the Baie Verte oceanic tract and its ophiolite cover sequence on the Baie Verte

Peninsula: Geological Survey, Newfoundland and Labrador Department of Natural Resources, Current Research, Report 10-1, p. 315–337.

Sparrow, B., Barrett, S., Copeland, D. A., and Walsh, M., 2017, Argyle Prospect Mineral Licences 012433M (11th year) and 020060M (5th year) Point Rousse Project, Baie Verte Peninsula, NL NTS sheet 12H/16, Assessment Report: Anaconda Mining Inc., Newfoundland and Labrador, Canada, 481 p.

Spooner, E. T. C., 1993, Magmatic sulphide/volatile interaction as a mechanism for producing chalcophile element enriched, Archean Au-quartz, epithermal Au-Ag and Au skarn hydrothermal ore fluids: Ore Geology Reviews, v. 7, p. 359–379.

Swinden, H. S., Jenner, G. A., Fryer, B. J., Hertogen, J., and Roddick, J. C., 1990, Petrogenesis and paleotectonic history of the Wild Bight Group, an Ordovician rifted island arc in central Newfoundland: Contributions to Mineralogy and Petrology, v. 105, p. 219-241.

Thomson, J.E., Charlewood, G.H., Griffin, K., Hawley, J.E., Hopkins, H., MacIntosh, C.G., Orgizio, S.P., Perry, O.S., and Ward, W., 1950, Geology of the Main Ore Zone at Kirkland Lake: Annual Report 1948, Ontario Department of Mines, p. 54-196.

van Staal, C. R., 2007, Pre-Carboniferous tectonic evolution and metallogeny of the Canadian Appalachians: in Goodfellow, W. D., ed. Mineral Deposits of Canada: A Synthesis of Major Deposit Types, District Metallogeny, the Evolution of

Geological Provinces and Exploration Methods: Geological Association of Canada, Mineral Deposits Division, Special Publications No. 5, p. 793–818.

van Staal, C. R., Barr, S. M., and Percival, J., 2012, Lithospheric architecture and tectonic evolution of the Canadian Appalachians and associated Atlantic Margin: in Percival, J. A., Cook, F. A. and Clowes, R. M., eds., Tectonic styles in Canada: the LITHOPROBE perspective: Geological Association of Canada, Special Paper 49, p. 41-95.

White, S.E. and Waldron, J.W.F. 2022: Along-strike variations in the deformed Laurentian margin in the Northern Appalachians: Role of inherited margin geometry and colliding arcs: Earth Science Reviews, Volume 226, 103931.

Williams, H., 1979, Appalachian orogen in Canada: Canadian Journal of Earth Sciences, v. 16, p. 792–807.

Williams, H. 1995, Temporal and spatial divisions, in Williams, H., ed., Geology of the Appalachians-Caledonian Orogen in Canada and Greenland: Geological Survey of Canada, Geology of Canada, no. 6 (also Geological Society of America, The Geology of North America, v. F-1), p. 21-44.

Williams, H., Colman-Sadd, S. P., and Swinden, H. S., 1988, Tectonic-stratigraphic subdivisions of central Newfoundland: Geological Survey of Canada, Current Research, Paper 88-1B, p. 91–98.

Williams, H. and Grant, A.C., 1998, Tectonic Assemblages map scale 1:3000000, Atlantic Region, Canada: Geological Survey of Canada, Open File 3657.

Williams, H. and Hiscott, R.N., 1987, Definition of the Lapetus rift-drift transition in western Newfoundland: Geology, v. 15, p. 1044–1047.

Williams, H. and St. Julien, P. 1982, The Baie Verte Brompton Line: Early Paleozoic continent ocean interface in the Canadian Appalachians. In Major Structural Zones and Faults of the northern Appalachians. Edited by P. St. Julien and J. Beland. Geological Association of Canada, Special Paper 24, p. 177–208.

Williams-Jones, A. E., Bowell, R. J., and Migdisov, A. A., 2009, Gold in solution: Elements, v. 5, p. 281–287.

Ybarra, S., Piercey, S., Layne, G. D., Copeland, D. A., and McNeil, P., 2017, Alteration halo and lithogeochemistry of the Pine Cove orogenic gold deposit, Baie Verte Peninsula, Newfoundland, Canada: GAC-Newfoundland and Labrador Section, 2017 Spring Technical Meeting, Program with Abstracts, St. John's, Newfoundland: Atlantic Geology, p. 250.

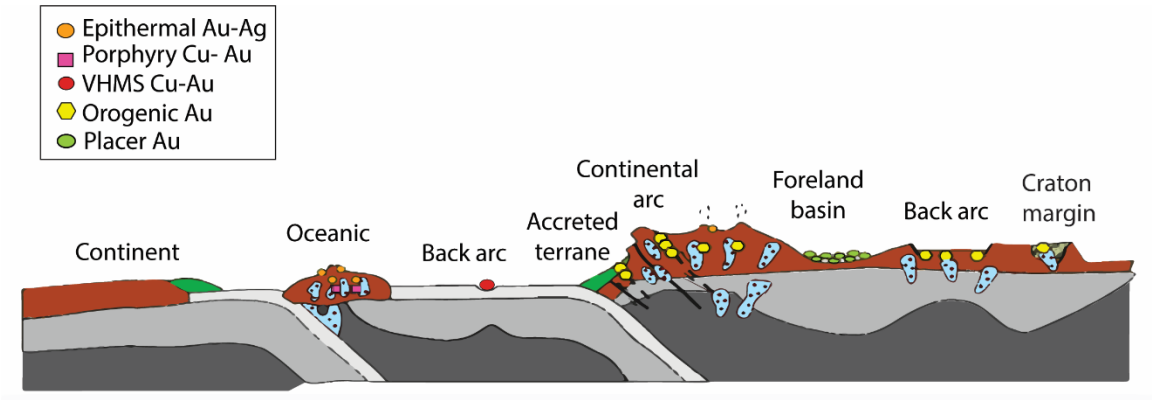

Figure 1.1. Tectonic settings in which gold deposits form. Orogenic gold deposits are found in deformed forearcs and backarcs, in addition to sheared margins of continental arc batholiths (modified after Goldfarb and Groves, 2015).

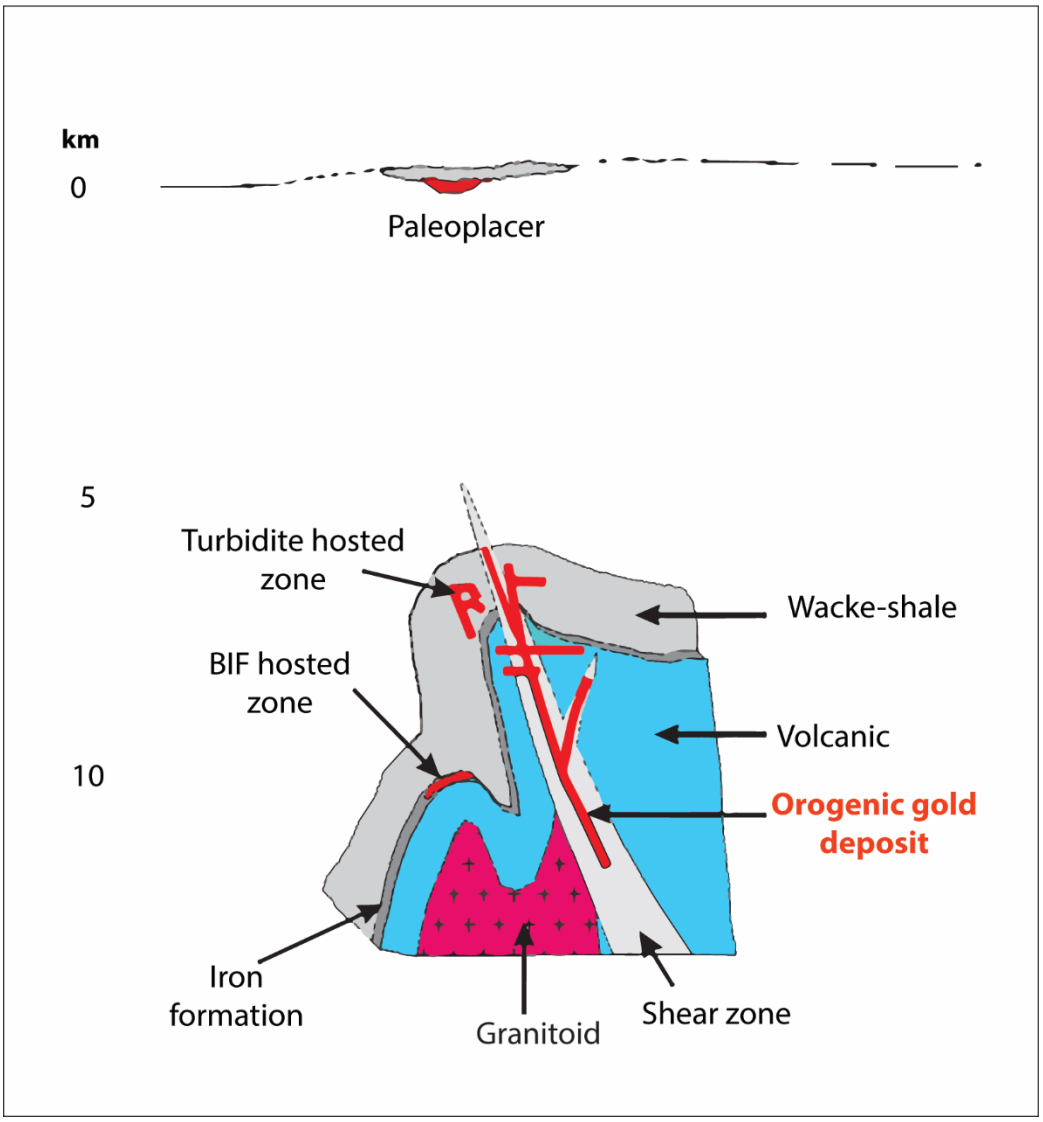

Figure 1.2. Inferred crustal levels of formation of orogenic gold deposits (modified after Poulsen et al., 2000; Dubé et al., 2001; Dubé and Gosselin, 2007).

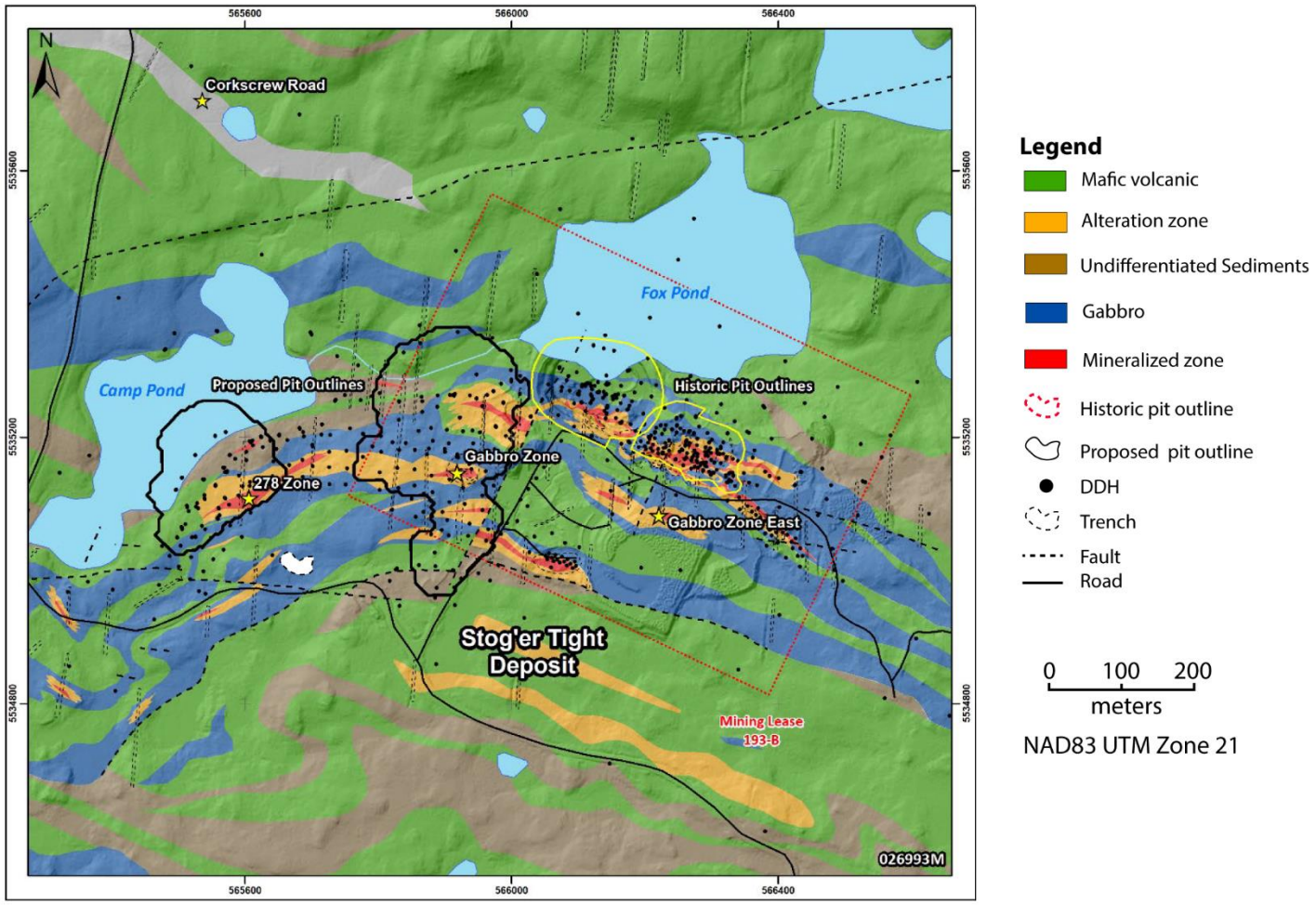

Figure 1.3. Geological map of the Stog'er Tight Area showing the Stog'er Tight Mine and the two pits constraining the 2021 Stog'er Tight Mineral Resource (modified after Kuntz et al., 2021).

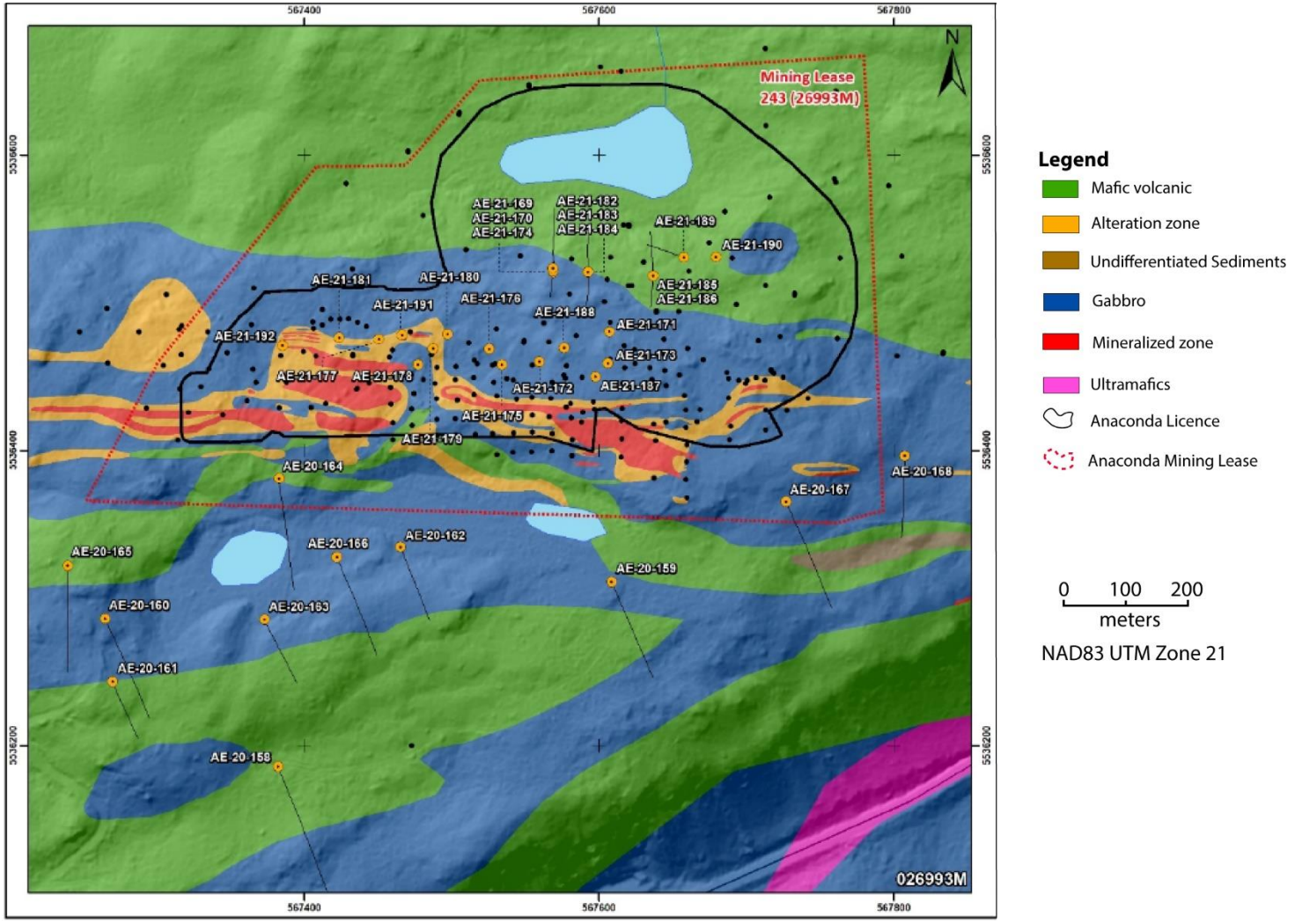

Figure 1.4. Diamond drill hole locations and geology of Argyle Deposit (modified after Kuntz et al., 2021).

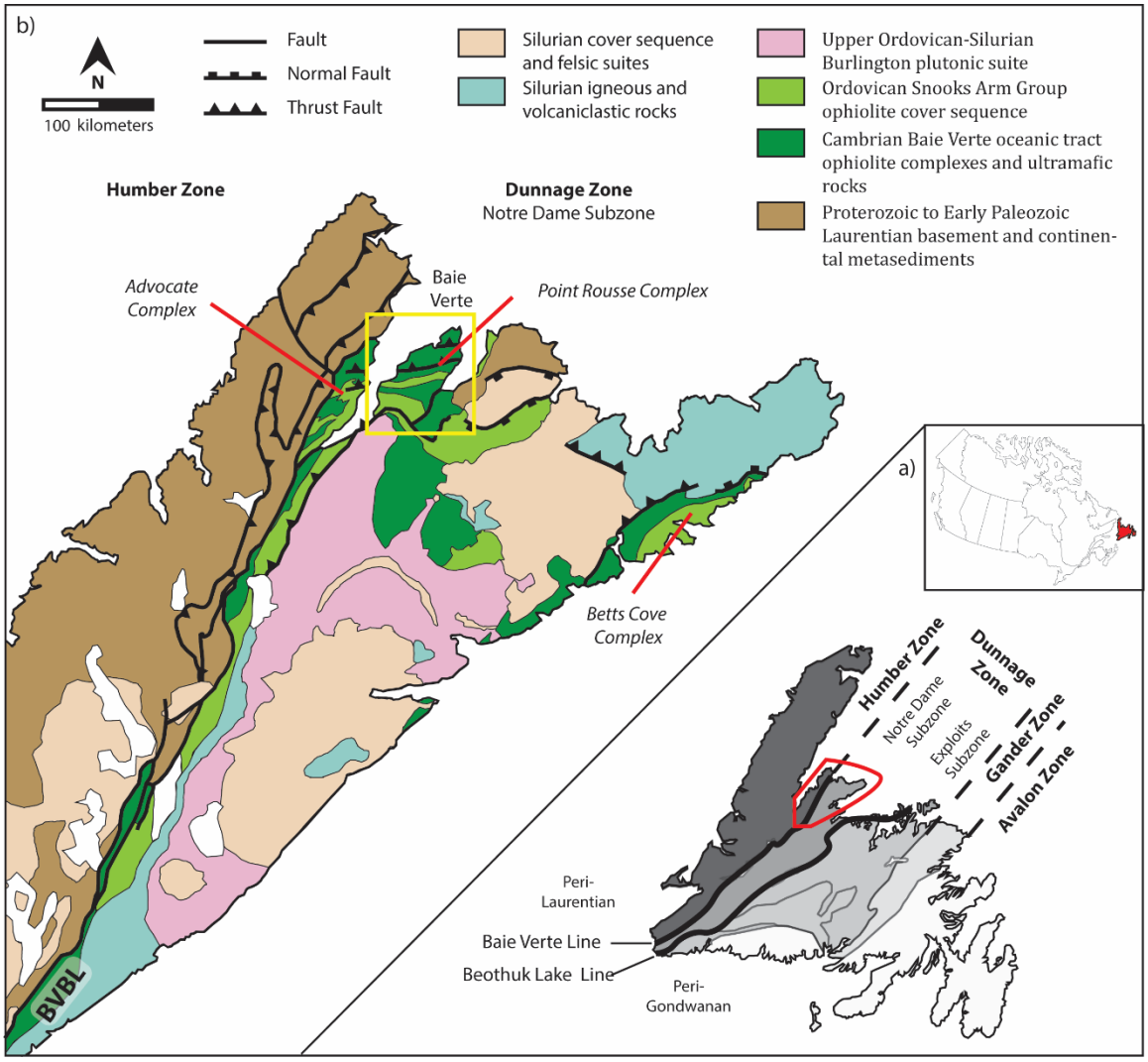

Figure 1.5. A) Simplified map of tectonostratigraphic terranes of Newfoundland (modified after Williams, 1979 and Williams et al., 1988). B) Geology map of the Baie Verte Peninsula (modified after Skulski et al., 2010 and Pawlukiewicz, 2019).

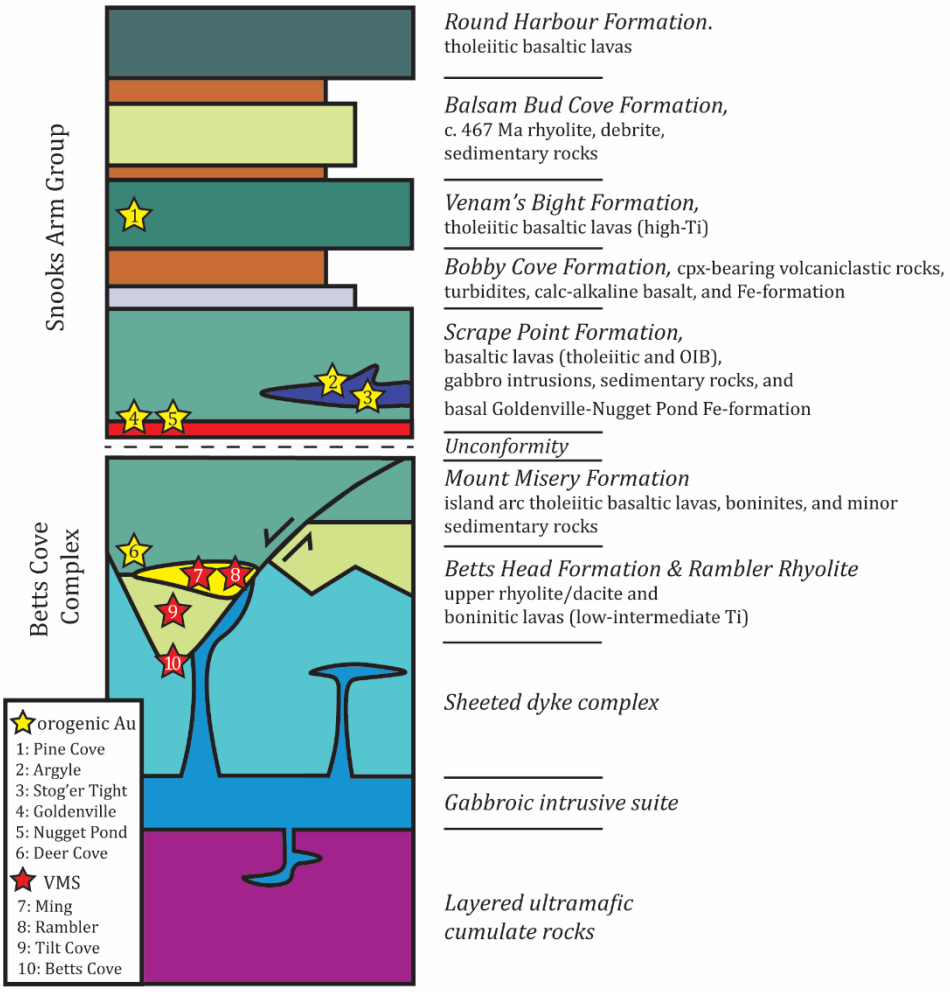

Figure 1.6. Stratigraphy of the Point Rousse Complex (modified after Skulski et al., 2009)

Chapter 2: Mineral Chemistry and Nd Isotope Geochemistry of Apatite in Orogenic Au-associated Gabbros, Baie Verte, Newfoundland

2.1. Abstract

The Baie Verte Peninsula, Newfoundland, hosts numerous gold occurrences primarily within Lower Ordovician volcanic cover sequences (Snooks Arm Group) and ophiolitic rocks of the Baie Verte oceanic tract. Gabbro-hosted orogenic Au can be found in three locations: the Stog'er Tight and Argyle deposits, and the Animal Pond prospect. All the deposits are in the hanging wall of the Scrape thrust fault at various distances from the thrust front, but typically within 100s of meters of the surface trace of the fault. Gold mineralization in all three areas is associated with pegmatoidal gabbros that are variably deformed and were metasomatically altered by orogenic Au-related hydrothermal fluids, but to different degrees. The igneous rocks contain primary igneous apatite that was partially to fully replaced during metasomatic alteration to produce secondary monazite and xenotime and that is spatially associated with hydrothermal zircon.

Both igneous and hydrothermally altered apatite have similar initial Nd isotope compositions: unaltered rocks ($\varepsilon_{Nd}(t)$= +2.34-6.60) and altered rocks ($\varepsilon_{Nd}(t)$ = +2.80-6.96), indicating the gabbroic magmas were derived from juvenile sources and that Nd isotopic compositions were not significantly changed during hydrothermal alteration. Compared to the $\varepsilon_{Nd}(t)$ of the depleted mantle reservoir at 420 Ma, the results are lower than the DM and implies involvement of Nd from a reservoir with a history of LREE-enrichment. In contrast to the Nd isotopes, the igneous and hydrothermally-altered apatite

exhibit wide variations in mineral chemistry and textures. Both are subhedral to euhedral and have homogeneous back-scattered electron (BSE) images; however, the apatite in the unaltered rocks display yellow to yellow-green cathodoluminescence (CL), whereas apatite in the altered rocks has dark green to gray CL. Apatite chemistry, as determined by electron microprobe and laser ablation inductively coupled plasma mass spectrometry, is also distinct. Magmatic apatite is enriched in Mn, Cl, Mg, REEs, U, Th and depleted in Sr, and has low Sr/Y compared to the hydrothermally influenced apatite. The apatite in fresh and altered rocks in Animal Pond Prospect, Stog'er Tight, and Argyle deposits have distinct chondrite-normalized REE patterns indicating significant changes in physicochemical conditions during ore-forming processes. Magmatic apatite has relatively flat REE distribution with negative Eu anomalies. Hydrothermally influenced apatites show two distinct REE patterns: the first group is relatively enriched in MREE producing a strong concave down pattern (hump pattern) with s positive Eu anomaly; and the second group has concave down pattern with a strong negative Eu anomaly similar to magmatic apatite. The textures and compositions are consistent with the altered apatites having undergone dissolution–re-precipitation processes and subsequent growth of hydrothermal monazite, and to a lesser extent xenotime.

This study illustrates that igneous apatite can be modified by hydrothermal fluids during fluid-rock interaction and can be used to determine igneous vs hydrothermally influenced apatite in orogenic Au, and likely other hydrothermal systems. Although the physico-chemical conditions during mineralization in orogenic gold deposits may vary between deposits, the collective textural, geochemical, and radiogenic isotopic indices of

apatite identified at orogenic gold deposits in the Baie Verte Peninsula have the potential to be vectors for the discovery of similar deposits in orogenic Au camps, globally.

2.2. Introduction

The Baie Verte Peninsula, western Newfoundland, Canada, hosts numerous orogenic gold occurrences, such as gabbro-hosted deposits (e.g., Stog'er Tight and Argyle deposit, Animal Pond prospect), basalt-hosted deposits (e.g., Pine Cove deposit), and iron formation-hosted deposits (e.g., Goldenville deposit; Ramezani et al., 2000; Evans, 2004; Castonguay et al., 2009; Skulski et al., 2009, 2010; Ybarra et al., 2017; Cullen et al., 2018).

The Baie Verte gold belt is associated with the Baie Verte line (BVL) and subsidiary faults, a regional-scale, complex brittle-ductile shear zone system in Newfoundland that separates obducted ophiolitic crust and mantle (Notre Dame subzone of the Dunnage Zone) from the Laurentian continental margin (Humber Zone; Williams, 1979; Williams and St-Julien, 1982; Castonguay et al., 2014). In this region, gabbro-hosted orogenic Au is found in three locations: the Stog'er Tight deposit, the Argyle deposit, and the Animal Pond prospect (Fig. 2.3). All the deposits are in the hanging wall of the Scrape thrust fault at various distances from the thrust front, but typically within 100s of meters of the surface trace of the fault. Gold mineralization in all three areas is associated with coarse-grained, pegmatoidal gabbros that are variably deformed and were metasomatically altered by orogenic Au-related hydrothermal fluids. The original igneous rocks contain primary igneous apatite that was subsequently partially to fully replaced

during later metasomatic alteration to produce secondary monazite and xenotime that is spatially associated with hydrothermal zircon (e.g., Ramezani et al., 2000; Piercey and Copeland, 2017).

The mineral apatite [$Ca_5(PO_4)_3(F, Cl, OH)$] has been the subject of several recent studies due to its common occurrence in a variety of geological systems including igneous rocks (Bouzari et al., 2016; Cao et al., 2021) and hydrothermal systems (Raimbault et al., 1993; Li and Zhou, 2015). The apatite crystallographic structure can incorporate a wide range of elements, including halogens, Na, Sr, Fe, Mn, U, Th, Y, and rare earth elements (REE; Piccoli and Candela, 2002; Pan and Fleet, 2002). Apatite is therefore a potential recorder of magmatic and hydrothermal processes (e.g., Sha and Chappell, 1999; Tepper and Kuehner, 1999; Belousova et al., 2002; Piccoli and Candela, 2002; Harlov and Forster, 2003; Hsieh et al., 2008; Boyce and Hervig, 2009; Chu et al., 2009; Harlov, 2015; Li and Zhou, 2015; Zeng et al., 2016). The texture, trace elements, and isotopic compositions of apatite crystallized from the magmatic system can also be used to monitor the history of magma and the fundamental chemical features of parental magmas (Tepper and Kuehner, 1999; Belousova et al., 2001; Miles et al., 2013; Bruand et al., 2017).

In this paper, a multi-method approach involving petrography, scanning electron microscopy (SEM), cathodoluminescence (CL) microscopy, mineral liberation analysis (MLA), electron probe microanalysis (EPMA), and laser ablation split stream (LASS) trace elements–Nd-Sm isotopic analysis is applied to apatite. As part of this study, textures, imaging, mineral chemistry, and Nd isotopic results from apatite grains from

various orogenic gold deposits in Baie Verte Peninsula are presented and evaluated to better understand igneous and hydrothermal processes, as well as to better understand the timing and evolution of orogenic gold deposits potentially. The results have potential implications not only for orogenic deposits on the Baie Verte Peninsula, but also for orogenic Au in similar districts globally.

2.3. Geological Setting

The island of Newfoundland forms part of the Paleozoic Appalachian-Caledonian orogenic belt, which is subdivided into Humber, Dunnage, Gander, and Avalon tectonostratigraphic zones (Williams, 1979; Williams et al., 1988; Fig. 2.1a). The Baie Verte Peninsula comprises portions of both the Humber Zone and the Notre Dame subzone of Dunnage Zone (Hibbard, 1983). These zones are tectonostratigraphically distinct and are separated from one another by the deformation zone known as the Baie Verte line (BVL; Fig. 2.1b; Williams, 1979; Hibbard, 1983; Castonguay et al., 2014).

The Humber Zone in the west represents Paleozoic rocks of the Laurentian (North American) passive continental margin that were deposited on Precambrian basement (Williams, 1979; Williams et al., 1999). The Dunnage Zone is divided into the western peri-Laurentian Notre Dame subzone and the eastern peri-Gondwanan Exploits subzone, and comprises sequences of ophiolitic and volcanic, volcaniclastic and sedimentary rocks of island arc and back-arc origins developed within the ancient Iapetus Ocean (Williams, 1979; Williams and St-Julien, 1982; Hibbard, 1983; Dunning and Krogh, 1985; Cawood and Dunning, 1993; Evans, 2004; van Staal, 2007; Skulski et al., 2009;

van Staal et al., 2012). The Gander Zone contains sedimentary rocks that were deposited along or around the eastern Iapetan margin, proximal to the Gondwanan continent (Williams et al., 1999; van Staal and Barr, 2012). The Avalon Zone is comprised of Neoproterozoic arc-related volcanic, sedimentary, and plutonic rocks that are overlain by Cambrian-Ordovician platformal sedimentary rocks (Williams et al., 1999; van Staal and Barr, 2012).

Gold mineralization in the Baie Verte Peninsula is mainly hosted by Lower Ordovician ophiolitic rocks and submarine volcano-sedimentary rocks of the Baie Verte oceanic tract (BVOT; Williams et al., 1988; Bédard et al., 1998; Evans, 2004; van Staal, 2007; Skulski et al., 2010). The stratigraphy of the ophiolite sequences on the Baie Verte Peninsula comprises the Betts Cove ophiolite and the Snooks Arm Group volcanic rocks (Skulski et al., 2010; Fig. 2.2). The Betts Cove Complex includes ultramafic cumulates overlain by gabbro, sheeted dykes, and pillow basalts, which contain numerous internal formations (Bédard et al. 2000; Skulski et al, 2010). It is unconformably overlain by the Snooks Arm Group, which comprises the Scrape Point, Bobby Cove, Venam's Bight, Balsam Bud Cove, and Round Harbour formations; this package is associated with most orogenic Au deposits on the Peninsula. The lowest part of the Snooks Arm Group, the Scrape Point Formation, contains local basaltic conglomerate cemented by jasper, overlain by red siltstone and shale and the Nugget Pond horizon, a banded iron formation that hosts the Goldenville gold deposit (Bédard et al., 2000). These rocks are covered by siltstones and tuffaceous wackes, which are overlain or interbedded with mafic tuffs and intruded by tholeiitic Fe-Ti-rich gabbros at the Argyle deposit, the Stog'er deposit, and

the Animal Pond prospect (Ramezani, 1992; Bédard, 1999; Bédard et al., 2000; Ramezani et al., 2000; Sangster et al., 2008; Skulski et al., 2010). The Bobby Cove Formation, which overlies the Scrape Point Formation comprises a lower calc-alkalic volcaniclastic member, the East Pond Member, which contains a green-grey clinopyroxene-phyric tuff (Skulski et al., 2010), and an upper member composed of volcaniclastic greywacke and siltstone interbedded with pelagic mudstone and felsic tuff beds (Cousineau and Bédard, 2000). The overlying the Venam's Bight Formation consists of tholeiitic, high-Ti basalts interbedded with volcanic breccia and hematitic mudstone or ironstone (Skulski et al., 2009, 2010; Ybarra et al., 2017). The Balsam Bud Cove Formation includes felsic tuff, rhyolite, tholeiitic basalt, red and green siltstone, shale, and sandstone (Bédard et al., 2000; Kessler and Bédard, 2000; Skulski et al., 2010). The Round Harbor Formation at the top of the Snooks Arm Group, is dominated by mostly sheet and pillowed flows of tholeiitic basalt (Bédard et al., 2000).

Castonguay et al. (2009) describe at least four phases (D_1-D_4) of regional deformation in the Baie Verte Peninsula. Poorly developed D_1 occurred as a result of obduction of Baie Verte oceanic tract ophiolites during the Taconic orogeny. D_2 represents the main tectonometamorphic phase on the Baie Verte Peninsula and is characterized by north-dipping, south-directed thrust faults and shear zones (e.g., Scrape thrust fault), which juxtaposed the Point Rousse Complex over the Pacquet Harbour Group; these are interpreted to be due to Salinic to Acadian deformation (Castonguay et al., 2009; Skulski et al., 2010; Sparrow et al., 2017). Fabrics associated with the D_3 deformation event are expressed as recumbent asymmetric folds and south dipping

extensional shear zones that affected D_1-D_2; they are attributed to the transpression associated with Devonian (Acadian) dextral transtension (Anderson et al., 2001). The D_4 deformation is defined by north-northeast trending anticlines and synclines that affect the structures of D_1-D_3, resulting regionally in double-plunging folds (Castonguay et al., 2009; Sparrow et al., 2017).

Orogenic gold mineralization in Baie Verte Peninsula is spatially and temporally related to the hanging wall sides of D_2 thrust sheets, such as Scrape and Deer Cove thrusts (Kirkwood and Dubé, 1992; Dubé et al., 1993; Evans, 2004; Skulski et al., 2009, 2010; Castonguay et al., 2009, 2014). Thrusting and orogenic gold mineralization are interpreted to be Silurian to Devonian in age, based on a radiogenic age determination and cross-cutting relationships from various deposits (Ritcey et al., 1995; Ramezani et al., 2000; Castonguay et. al, 2009; Kerr and Selby, 2012).

2.4. Baie Verte Peninsula Gabbro Hosted Orogenic Gold Deposit Characteristics

Apatite from several orogenic gold deposits in Baie Verte Peninsula, Newfoundland, was studied, including the Stog'er Tight deposit (642,000 t @ 3.02 g/t Au indicated, and 53,000 t @ 5.63 g/t Au inferred resources; Kuntz et al., 2021), the Argyle deposit (436,800 t @ 2.53 g/t Au indicated and 500 t @ 2.77 g/t Au inferred resources; Kuntz et al., 2021), and the Animal Pond Prospect (Fig. 2.4).

The gold deposits in this area have similar mineralization characteristics. The deposits are hosted in the Scrape Point and Bobby Cove formations of the Snooks Arm Group that include massive basalt flows interbedded with green mudstone, tuffs,

clinopyroxene-phyric lapilli and crystal tuffs (Fig. 2.4; Bédard et al., 2000; Skulski et al., 2009, 2010). The rocks in this study are all vari-textured gabbros that range from coarse- to fine-grained to locally pegmatoidal, and are composed of plagioclase, pyroxene, amphibole, ilmenomagnetite and apatite (Fig. 2.5). The alteration assemblages are dominated by albite, chlorite, Fe-carbonate, hematite, leucoxene, and quartz veins, with or without associated chlorite.

Gold mineralization is associated with the coarsest, pegmatoidal gabbros and is spatially linked to the presence of coarse-grained Fe-Ti minerals (Piercey and Copeland, 2017: Pawlukiewicz, 2019). Gold is always found in conjunction with pyrite as micro-veinlets and blebs, formed in response to wall-rock sulfidation. Only Argyle and Stog'er deposit have significant gold and CO_2-albite-leucoxene-pyrite alteration; Animal Pond only has minor mineralization. Previous studies have dated gold mineralization in the area as Silurian-(Devonian), based on a 420 ± 5 Ma U-Pb date for hydrothermal zircon at Stog'er Tight and a 420 ± 7 Ma Re-Os date for pyrite from Pine Cove (Ramezani et al., 2000; Kerr and Selby, 2012).

2.5. Apatite

Apatite is the most common phosphate accessory mineral that forms in a variety of igneous, sedimentary, and metamorphic rocks. Apatite is defined by the generic formula $A_5(XO_4)_3Z$ and crystallizes in the hexagonal system. The A-site accommodates large cations (e.g., Ca^{2+}, Sr^{2+}, Pb^{2+}, Ba^{2+}, Mg^{2+}, Mn^{2+}, Fe^{2+}, REE^{3+}, Eu^{2+}, Cd^{2+}, Na^{+}), which occupy two sites in VII-fold (Ca2) and IX-fold coordination (Ca1; Elliot, 2002;

Pasero, 2010). The X-site is primarily occupied by P^{5+} (as PO_4^{3+}) and can accommodate other minor highly charged cations (e.g., Si^{4+}, S^{6+}, As^{5+}, V^{5+}). The halogens F^- and Cl^-, as well as OH^-, occupy the Z site.

The apatite mineral group refers to calcium phosphate minerals with various end-member compositions, including hydroxyapatite $Ca_5(PO_4)_3(OH)$, fluorapatite $Ca_5(PO_4)_3F$, and chlorapatite $Ca_5(PO_4)_3Cl$, which have names proportional to the abundance of OH^-, F, or Cl^- ions, respectively, in their structures. The structure of apatite can contain a wide range of transition metals, rare earth elements (REEs), and anions. The following are some of the most common apatite substitutions (Elliot, 1994; Sha and Chappell, 1999, Waychunas, 2002; Hughes and Rakovan, 2015; Mao et al., 2016):

$$Sr^{2+}, Mn^{2+}, Fe^{2+}, REE, Y^{3+}, Na^{+} \leftrightarrow Ca^{2+} \quad (1)$$

$$Si^{4+}, As^{5+}, S^{6+} \text{ and } C^{4+} \leftrightarrow P^{5+} \quad (2)$$

$$Cl^{-} \text{ and } OH^{-} \leftrightarrow F^{-} \quad (3)$$

$$2Ca^{2+} \leftrightarrow Na^{+} + REE^{3+} \quad (4)$$

$$Ca^{2+} + P^{5+} \leftrightarrow REE^{3+} + Si^{4+} \quad (5)$$

The most widespread apatite in igneous rocks is fluorapatite (Piccoli and Candela, 2002). Chlorine and OH are frequently found in fluorapatite, where they can rarely reach high concentrations (Piccoli and Candela, 2002). Apatite also contains Br and I, but their concentrations are much lower than those of Cl and F. Apatite can contain a variety of cations in place of Ca and P, but their concentrations are rarely high enough to

distinguish the mineral as a distinct species (Piccoli and Candela, 2002). As a result of P being widespread in magmas, apatite is commonly found in almost all igneous rocks. Apatite can contain elements with diverse geochemical characteristics that are sensitive to melt and fluid development, such as halogens, REEs, Sr, Y, Th, and U (e.g., Sha and Chappell, 1998; Belousova et al., 2002; Shaw, 2003; Emerson et al., 2004; Bouzari et al., 2016; Bruand et al. 2017). Apatite is increasingly seen as a potential monitor of hydrothermal processes and a potential tool for mineral exploration targeting, but these have not yet been much tested in orogenic Au deposits. The presence of apatite associated with orogenic gold deposits may also provide new avenues in exploration for these deposits.

2.5.1. Apatite luminescence

Apatite group minerals show luminous characteristics with variable emission colors and in some cases complex zoning under cathodoluminescence (CL). Luminescence is controlled by transition metal, REE, and anion substitutions, the various formation conditions, and the apatite structure itself (Waychunas, 2002). Important CL activators in apatite include Mn^{2+}, Cr^{3+}, Fe^{3+}, Ti^{4+} and REE (e.g., Pr^{3+}, Nd^{3+}, Sm^{3+}, Eu3+, Tb^{3+}, Dy^{3+}, Ho^{3+}, and Er^{3+}), whereas some elements (Fe^{2+}, Co^{2+} and Ni^{2+}) inhibit or eliminate CL in apatite (Pagel et al., 2000). Cathodoluminescence microscopy is a fast method that can be sensitive to subtle variations in the trace element chemistry of apatite. The presence of traces of Mn^{2+} in magmatic apatite causes canary-yellow luminescence in CL. In general, higher REE concentrations are associated with more violet/blue luminescence (Kempe and Götze 2002; Götze at al., 2013). Where the concentrations of

these elements vary even slightly at the ppm level, the peak intensity changes, resulting in a change in the overall luminescence and, consequently allowing the growth domains in the mineral/apatite to be distinguished (Gros et al., 2016).

Several studies showed that apatite from different deposit types display diagnostic CL colors. For example, apatite occurring in granitic rocks and pegmatites display a bright yellow to yellow-orange luminescence in CL, whereas apatite in carbonatites have blue CL, and apatite in peralkaline syenite have pink-violet CL (e.g., Portnov and Gorobets, 1969; Marfunin, 1979; Mariano, 1988; Kempe and Götze, 2002).

Different apatite textures can also indicate (e.g., early magmatic, or late hydrothermal) evolutionary stages in different geological settings (Broom-Fendley et al., 2016, 2017; Chakhmouradian et al., 2017). Cathodoluminescence and backscattered electron imaging of apatite textures are very useful for understanding apatite formation history, particularly when combined with in situ chemical analyses (Campbell and Henderson, 1997; Mitchell, 2014; Bouzari et al., 2016; Broom-Fendley et al., 2016, 2017; Chakhmouradian et al., 2017; Decree et al., 2020; Mercer et al., 2020).

2.6. Sampling and Analytical Methods

2.6.1. Sample selection and preparation

Representative samples that had potential to contain apatite were selected from gabbros from the Animal Pond prospect, and the Stog'er Tight and Argyle deposits. Factors guiding the sample selection were the occurrence of different, well-characterized alteration assemblages of varying intensity, elevated Au contents (Stog'er Tight and

Argyle), and lack of alteration in host rocks with low Au contents (Animal Pond). Eight samples were selected for this research that contained various alteration intensity and proximity to mineralization, including 195939 (weak) and 195941 (distal) from the Animal Pond prospect; 195908 (strong), 195913 (strong), 16SJP001 (proximal), and 16SJP002 (proximal) from Stog'er Tight deposit; and 16SJP008 (distal) and I951379 (proximal) from Argyle deposit. Samples were chosen from geologically well characterized sections from these deposits that were part of previous studies (e.g., Piercey and Copeland, 2017; Pawlukiewicz, 2019).

In all prospects/deposits there are distinctive mineralization-related hydrothermal alteration assemblages (e.g., weak vs distal, strong vs proximal; Ramezani et al., 2000; Pawlukiewicz, 2019). The distal alteration zone (30-70 m) consists of chlorite-calcite-rutile ± epidote-albite. The proximal alteration zone (2-25 m) is defined by gabbro that is pervasively altered to sericite-quartz-ankerite ± albite-chlorite-rutile-pyrite-gold.

Apatite samples were taken from blocks of gabbroic material and not separated from the samples in order to preserve spatial relationships between apatite and other phases. The gabbroic samples were first sawed and then mounted as 25mm wide by 6mm tall epoxy pucks and were polished and used in all other petrographic and microanalytical methods, including standard petrography, CL microscopy, scanning electron microscopy (SEM)(+mineral liberation analysis (MLA) and CL-imaging), electron probe micro analysis (EPMA), and laser ablation split stream (LASS)-inductively coupled plasma mass spectrometry (ICP-MS) and multi-collector ICP-MS (MC-ICP-MS). All analyses were conducted at the Department of Earth Sciences

(TERRA) and the Core Science Facility, Memorial University of Newfoundland, Canada and details of the analytical procedures are provided below.

2.6.2. Bench-top cathodoluminescence

Thin sections were analyzed by CL microscopy using a PATCO ELM-3 Cathodoluminoscope at Memorial University of Newfoundland. The CL operating conditions were 12 kV, 0.7mA, a vacuum of ~7 Pa, using an unfocused beam. Images were acquired using a KAPPA DX-30C Peltier cooled charge-coupled device (CCD) camera, with a 5x objective lens on an Olympus BX WI-50 microscope and KAPPA software. All CL images have a field of view of 2.5 mm along the x-axis. All CL images were acquired using the same red-green-blue (RGB) settings so that CL colors could be directly compared between samples.

2.6.3. Scanning electron microscopy

Back-scattered electron (BSE) imaging was used to identify fractures and inclusions within the grains and to identify mineral phases. The BSE and cathodoluminescence imaging were performed at the Hibernia Microbeam Laboratory at Memorial University of Newfoundland using a JEOL 7100F field-emission scanning electron microscope equipped with energy dispersive spectroscopy (EDS) at 15 kV and 50 nA. Apatite grains, as well as any associated minerals, were identified using BSE imaging and confirmed by EDS, and the intensity of CL was also determined on each apatite. Cathodoluminescence and BSE images were also used to determine which

microanalytical spots would be examined in individual apatite grains, to identify potential mineral zoning, and to avoid both cracks and inclusions.

2.6.4. Scanning electron microscopy-mineral liberation analysis (SEM-MLA)

The samples were also analyzed using SEM-MLA analysis to obtain quantitative maps of mineral grain locations and to determine the sizes and shapes of grains, but also the spatial relationships in the mounts (e.g., textural relationships of hydrothermal vs igneous apatite). During analytical work, the operator can also query the position and/or shape of certain particles. The polished mounts were carbon-coated and mapped using a FEI Quanta 650 SEM (CREAIT facility, MUN) equipped with MLA software developed by JKTech, University of Queensland, Australia. Operating conditions for the SEM were a 25kV, 13nA beam current, and 12 mm working distance. A library of X-ray spectra was utilized for mineral identification that has produced 0.3% unknown minerals using a 70% match threshold. All false color mount maps are available in Appendix C. The coordinates of the apatites in the mounts were determined and these were used to locate the apatites in laser ablation ICP-MS and MC-ICP-MS.

2.6.5. Electron probe micro analysis (EPMA)

Major and minor elements in apatite were measured using a JEOL JXA-8230 SuperProbe electron probe microanalyzer equipped with five tuneable wavelength-dispersive X-ray spectrometers (WDS). All mounts were polished and coated with a ~20 nm (~200 Å) evaporated carbon film to prevent charge build up. The locations analyzed by EPMA were precisely marked on BSE and/or CL photomicrographs, so that the

analysis locations could be easily located subsequently for in situ laser ablation (LA)-ICP-MS trace element analysis and for LA-MC-ICP-MS analysis of Nd. Depending on the texture and relationship of the grains based on the BSE and/or CL images, two or more analyses were conducted per mineral grain. Samples underwent initial wavelength scans and energy dispersive spectroscopy (EDS) to ensure that the proper elements were selected and measured, to identify appropriate background positions, and to identify interferences. Apatite grains were analyzed for F, Fe, Mn, Nd, Ce, La, Cl, Ca, S, P, Na, Si, As, Mg, U, Th, Y, and Sr. The operating conditions were an accelerating voltage of 15 kV, a Faraday cup current of 20 nA, and a defocused beam diameter of 10 μm. The standards for adjustment include fluorapatite for F$K\alpha$ and Ca$K\alpha$, almandine (garnet) for Fe$K\alpha$, rhodenite for Mn$K\alpha$, NdP_5O_{14} for Nd$L\beta$, CeP_5O_{14} for Ce$L\alpha$, LaP_5O_{14} for La$L\alpha$, chlorapatite for Cl$K\alpha$, sphalerite for S$K\alpha$, apatite for P$K\alpha$, albite for Na$K\alpha$ and Si$K\alpha$, arsenopyrite for As, diopside for Mg$K\alpha$, synthetic-UO_2 for U$M\alpha$, synthetic-hutt for Th$M\alpha$, YP_5O_{14} for Y$L\alpha$, and celestite for Sr$L\alpha$, respectively. Count times were optimized for each element as follows: 10 s on peak and 5 s on background for F; 30 s on peak and 15 s on background for Ca, Fe, Mn, Nd, Ce, La, Ca, S, Si, As, Mg, U, Th, Y, and Sr; and 20 s on peak and 10 s on background for Cl, P, and Na.

As EPMA does not measure H_2O, and there is some mixing on the monovalent anion site, OH content must be calculated from F and Cl measurements. Calculations were done using an apatite formula $Ca_5(PO_4)_3(F,Cl,OH)$ using 12.5 oxygens and a modified calculation method of Ketcham (2015). Stoichiometry and total values were

used to determine whether to accept each analysis. Any analyses that had totals outside of 99-101 wt. % were discarded.

2.6.6. Laser ablation split stream (LASS) trace elements–Nd isotopes in apatite

Representative apatite grains were analyzed in situ for trace elements and Sm-Nd isotopes. Sm-Nd isotopes, paired with trace elements, were analyzed by the LASS method at the Core Science Facility, Memorial University of Newfoundland, Canada. The trace element analyses were done using a Thermo-Finnigan ELEMENT XR, a high-resolution double focusing magnetic sector inductively coupled plasma mass spectrometer (HR-ICP-MS) coupled to a GEOLAS 193 nm Excimer laser ablation system. The Sm-Nd analyses were done using a Thermo Finnigan Neptune MC-ICP-MS.

The ablated material was transported to the ICP-MS using He gas with a flow rate of 1.25 l/min, with additional Ar make-up gas added after the ablation cell and prior to introduction into the ICP-MS. Both mass spectrometers were interfaced to a GeoLas Pro 193 nm Ar–F excimer laser, operated at 10Hz, 5 J/cm^2, and 99-109 μm diameter spot size. After collecting background counts for 30 sec, each spot was ablated for 60 sec.

The apatite reference materials used in this study for the Nd-Sm LASS analyses included TH-1 that was the primary Nd-Sm reference material. Madagascar apatite (MAD02) and Durango apatite were used as secondary reference materials. NIST 610 and BCR-2G glasses were used as the external calibration standard, interspersed during the trace element analyses.

Every twelve analyses were followed by two analyses of TH-1, one analysis of MAD02, one analysis of Durango apatite, NIST610 glass and BCR-2G glass, respectively. For calibration purposes, Ca concentration determined by electron microprobe on a synthetic apatite (JMH_fluorapatite_319) was used as an internal standard. The data were reduced using Iolite software (Paton et al., 2011).

Reference materials analyzed in this study include TH-1, MAD02, and Durango apatite resulted in isotopic compositions of $^{143}Nd/^{144}Nd=0.512048\pm0.000029$, $^{143}Nd/^{144}Nd=0.511306\pm0.000026$, $^{143}Nd/^{144}Nd=0.512482\pm0.000028$, respectively, in good agreement with lab average values (Yang et al., 2014).

The initial $^{143}Nd/1^{44}Nd$ values were calculated using a present-day chondritic uniform reservoir (CHUR) value of $^{147}Sm/^{144}Nd=0.196593$ and $^{143}Nd/^{144}Nd=0.512638$, as reported by Jacobsen and Wasserburg (1980) and the $\lambda^{147}Sm$ decay constant of 6.54×10^{-12}/year from Steiger and Jäger (1977). $\varepsilon_{Nd}(t)$ were calculated using $^{143}Nd/^{144}Nd$ (CHUR) = 0.512638 from Hamilton et al. (1983) and $^{147}Sm/^{144}Nd$ (CHUR) = 0.1967 from Jacobsen and Wasserburg (1980). The $\varepsilon_{Nd}(t)$ values were calculated at 420 Ma, the interpreted age of mineralization (e.g., Ramezani et al., 2000; Kerr and Selby, 2012). The depleted mantle model ages (T_{DM}) are calculated using $^{143}Nd/^{144}Nd = 0.513113$ and $^{147}Sm/^{144}Nd = 0.2114$ (Goldstein et al., 1984).

2.7. Results

2.7.1. Textural characteristics

Apatite is the most common accessory mineral occurring in the fresh and altered gabbros. Petrographic and BSE images are generally homogenous, regardless of origin; however, CL signatures for igneous and hydrothermally influenced apatite grains have distinct features. Representative BSE images of apatite grains from the Animal Pond prospect, Stog'er Tight and Argyle deposits are presented in Figures 2.6 and 2.7. BSE and CL photomicrographs of each of the samples from this study are also presented in Appendix A-B.

2.7.1.1. Apatite in unaltered rocks

Magmatic apatite in unaltered host rocks display subhedral to euhedral crystal forms and range from ~10 to 100 μm in size, with some prismatic grains >100 μm. They commonly occur as inclusions within phenocrysts (e.g., ilmenite, Fig. 2.6c) or as individual grains within the matrix, with no concentric zoning patterns. Although many grains have homogeneous textures, some apatite grains show minor internal zoning in either BSE or CL. Rarely, apatite grains contain visible inclusions of zircon or have a distinctive dark green core and light green zones or rims in bench-top CL images (Fig. 2.6).

In fresh gabbro, apatite commonly coexists with ilmenite and magnetite (Figs. 2.6a, 6c, and 6d). Apatite coexisting with ilmenite displays a euhedral crystal shape and has a bright reflection in BSE and CL images. Apatite coexisting with calcite displays anhedral crystal shapes and contains voids and fractures. Under BSE images, some igneous apatites have mineral inclusions, including zircon and ilmenite. Most of the

mineral inclusions in the rims of apatites are zircons (Figs. 2.5e, f). Under CL, apatite in unaltered gabbros displays strong yellow to yellow-green luminescence. Calcite, characterized by red luminescence, is commonly observed with apatite in fresh rocks (Figs. 2.5g-i).

2.7.1.2. Apatite in altered rocks

Apatite in hydrothermally altered rocks (i.e., hydrothermally influenced apatite), occurs as homogeneous subhedral to anhedral grains, locally rounded, with a grain size ranging from 10 to 100 μm; larger grains of 100-200 μm are also common in some samples. Apatite commonly occurs in altered and mineralized rocks as inclusions in other mineral phases (e.g., pyrite, Fig, 2.7) or as individual grains within the matrix of the gabbro (Fig. 2.7). Hydrothermally influenced apatite usually coexists with secondary hydrothermal minerals, including zircon, monazite, and xenotime (Fig. 2.7) and/or with pyrite associated with gold mineralization (Fig. 2.8). Phosphate minerals, including monazite and xenotime, are abundant in mineralization-related hydrothermal alteration zones (Figs. 2.7a-c). These finer-grained minerals occur as inclusions in apatite or are scattered throughout the other mineral phases associated with the gangue minerals proximal to hydrothermally influenced apatite. Acicular textures are also observed in some apatites (Fig. 2.7e).

Apatite grains in altered gabbros are similar to those occurring in unaltered gabbros in petrographic and BSE images; however, they have distinctive dark green to gray luminescence. In some cases, the apatite retains green luminescence commonly on

the outside margins of apatite crystals, whereas in pervasively altered and/or mineralized rocks they have a distinct dull gray luminescence (Fig. 2.7j). Apatite grains with green and gray luminescence in the altered rocks typically occur with calcite (Figs. 2.7j, 7k, and 7l). A subset of the apatite grains occurring in hydrothermally altered gabbros display complex CL features with heterogeneous patchy patterns and are brighter in SEM-CL images.

2.7.2. Apatite major and trace elements geochemistry

The major, minor and trace element composition of the studied apatite grains is summarized in Appendices D and E with concentrations in weight percent (wt%) for EPMA and ppm for LASS analyses.

Electron probe microanalyses data indicate that apatite grains from gabbro-hosted Au deposits are all fluorapatite (Fig. 2.9a) and contain high F (1.44-5.33 wt. %) and low Cl (0.001-0.58 wt. %); a negative correlation occurs between F and Cl (Fig. 2.9b). The presence of F contents higher than ~3.77 wt. % in some apatite grains is possibly due to poor precision or peak overlap in fluorine (Stormer et al. 1993; Piccoli and Candela, 2002).

Major elements in apatite vary from ~37.3–44.9 wt. % P_2O_5 and ~48.8–57.8 wt. % CaO. Apatite shows distinct major element compositions between fresh and altered rock samples. Apatite in altered samples have generally higher P_2O_5, CaO, and F, and lower SiO_2 contents compared to apatite from fresh/unaltered gabbro samples (Fig. 2.10). Further, apatites in fresh rocks have higher contents of MnO (0.02-0.17 wt. %), Cl (0.02-

0.58 wt. %), and FeO (0.10-3.55 wt. %) compared to the apatite in altered rocks (MnO=0.01-0.16 wt. %, Cl=0.01-0.4 wt. %, FeO=0.01-2.2 wt. %; Fig. 2.10-11).

Strontium concentrations are highly variable across all analyzed apatites ranging from 480-2370 ppm with apatite grains from mineralized rocks containing the greatest concentrations of Sr (584-2370 ppm) compared to the unmineralized rocks (480-1350 ppm). Concentrations of Y in apatite from the unaltered/fresh rocks (485-3390 ppm) are higher than apatite in altered rocks (57.7-1700 ppm; Fig. 2.12).

Magmatic apatites have total REE concentrations ranging from 2104 to 16008 ppm, and they show a relatively flat REE distribution with negative Eu anomalies (Figs. 2.15a-b). They are relatively enriched in LREE compared to apatite grains in altered rocks (Fig. 2.12d) with $(La/Yb)_N$ between 2.00-11.73. Ce/Ce* ratios are between 0.91-1.17 and Eu/Eu* ratios are between 0.21-0.91 in magmatic apatite. Hydrothermally altered apatite have much lower total REE concentrations than magmatic apatite grains, varying between 116 to 9305 ppm, and show two distinct REE patterns: the first group is relatively enriched in MREE producing a strong concave down pattern (hump pattern) with positive Eu anomaly, whereas the second group have concave down patterns with a strong negative Eu anomaly similar to magmatic apatite (Figs. 2.15c-d). One population of apatite from the strong alteration (all from sample: 195908) that is very uniform and distinctive with the depleted REE that does not show a continuum with the other ones with higher LREE or the proximal ones (Fig. 2.15c). LREE in hydrothermally influenced apatite show a depletion in compared to magmatic apatites with $(La/Yb)_N$ = 0.53 to 25.58, Ce/Ce* ratios are between 0.81-1.25, and Eu/Eu* ratios are between 0.46-1.61.

Thorium content in apatite from fresh gabbro samples has an average concentration of 7.18 ppm, whereas in altered apatite has an average concentration of 4.08 ppm (Fig. 2.12c). A similar trend is observed for U, where apatite from fresh gabbro have an average value of 3.16 ppm and 1.17 ppm for apatite in samples with hydrothermal alteration (Fig. 2.12c).

2.7.3. In situ Nd isotopic compositions of apatite

Results of in situ Sm-Nd isotope analysis of apatite are presented in Appendix F. Samarium and Nd isotopes were measured on individual apatite grains to calculate $\varepsilon_{Nd}(t)$, which is used to constrain the REE sources of the apatite.

The measured $^{143}Nd/^{144}Nd$ ratios of apatite from samples of unaltered gabbros range from 0.512215 to 0.512848. The initial $^{143}Nd/^{144}Nd$ ratios of magmatic apatite range from 0.512150 to 0.512435, corresponding to an $\varepsilon_{Nd}(t)$ range of +2.30-6.60 with an average of +5.18 (n = 113). The measured $^{143}Nd/^{144}Nd$ ratios of apatite from altered gabbros range from 0.512670 to 0.513400. The initial $^{143}Nd/^{144}Nd$ ratios range from 0.512233 to 0.512454 with $\varepsilon_{Nd}(t)$ range of +2.80-6.96 with an average of +5.23 (n = 90).

2.8. Discussion

Apatite is a common accessory mineral in igneous rocks and in hydrothermal ore deposits (Frietsch and Perdahl, 1995, Sha and Chappell, 1999, Belousova et al., 2002, Pan and Fleet, 2002). In igneous rocks, the composition of apatite is primarily determined by the magma composition, though it can also be significantly modified by a variety of magmatic processes, such as fractional crystallization and magma mixing, as well as

post-crystallization hydrothermal processes (e.g., Boudreau et al. 1993; Sha and Chappell 1999; Belousova et al. 2001; Chu et al. 2009; Bruand et al. 2014, 2016, 2017; Harlov 2015; McCubbin and Jones 2015; Bouzari et al. 2016; Palma et al. 2019). The texture of apatite grains can also be used to determine the magmatic and hydrothermal history of the rock (Harlov and Förster, 2003; Harlov et al., 2005; Bouzari et al., 2016; Cao et al., 2021). In addition, apatite trace element composition has been used to determine the composition of magmatic fluids, the oxidation state of magma, and the effects/consequences/course of assimilation and fractionation (Tepper and Kuehner, 1999; Belousova et al., 2002; O'Reilly and Griffin, 2000; Patiño-Douce et al., 2011); thus, it has been shown to be a useful tool for distinguishing magmatic and hydrothermal processes (e.g., Krneta et al., 2017). In the following sections, we will discuss the possible effects of these factors on textural and compositional variations observed in apatite from the variably altered gabbro-hosted orogenic Au deposits on the Baie Verte Peninsula, Newfoundland.

2.8.1. Apatite textures

Apatite textures may change during igneous and metasomatic events (Harlov, 2015). In unaltered apatite from Animal Pond, displays primary igneous growth zoning with a distinctive dark-green core and a light green rim in bench-top CL, possibly due to variable Mn^{2+} concentrations in the apatite and/or crystallization under changing redox conditions (Fig. 2.6g; Kempe and Götze, 2002; Mitchell, 2014). Other samples from unaltered gabbros have yellow-to-yellow green CL signatures, typical of igneous apatite,

likely due to the presence of traces of Mn^{2+} in the apatite (e.g., Roeder et al., 1987; Kempe and Götze 2002).

In the early stages of alteration, the margins of the apatite likely reacted with hydrothermal fluids, which produced BSE-dark rims and BSE-bright cores that are present in apatites from sample 195913 (strongly altered, Stog'er Tight deposit; Fig. 2.7f). In proximal altered samples (16SJP001, 16SJP002, I951379), secondary REE minerals, such as monazite and xenotime, are associated with hydrothermal apatite (Figs. 2.7a-c). Monazite and xenotime inclusions are found only in hydrothermally altered samples and are interpreted to have formed due to hydrothermal alteration. The monazite-xenotime associations with apatite in altered gabbros lead to complex intergrowth textures and CL and mineral chemistry. For example, these apatites display dark green to gray luminescence and they exhibit depletions in Mn, Cl, and REE that are interpreted to have been the reason for the loss in luminescence. Moreover, it is interpreted that depletion in these elements was due to hydrothermal fluid leaching of Mn-Cl-REE from the original igneous apatites (Bouzari et al., 2016; Cao et al., 2021). The following section will investigate this further and the links between luminescence features and apatite compositions.

2.8.2. Apatite composition variations

Researchers have shown that apatite texture, chemistry, and isotope compositions can be modified by hydrothermal fluids (Harlov and Förster, 2003; Harlov et al., 2005; Migdisov and Williams-Jones, 2014; Li and Zhou, 2015; Zhao et al., 2015; Betkowski et

al., 2016; Bouzari et al., 2016; Zeng et al., 2016; Li et al., 2018; Palma et al., 2019). Moreover, apatite composition is dependent on the composition of the parent magma/fluid-apatite partition coefficients and is also influenced by the growth of competing igneous and hydrothermal minerals during apatite crystallization (Sha and Chappell, 1999; Belousova et al., 2002; Palma et al., 2019).

In the apatite from this study, regardless of origin, the halogen compositions show that all apatite, regardless if they are fresh or altered, are close to the fluorapatite end-member with constant F and low Cl contents (Fig. 2.10a-b). Compared to apatites in altered rocks, apatites in fresh gabbro contain more Mn, Mg, S, and Cl (Figs. 2.10, 2.11, 2.12a), suggesting magmatic apatite was modified by later hydrothermal fluids during water-rock reactions associated with orogenic Au formation.

These major element chemical differences also influence the cathodoluminescence responses in the different types of apatite grains. For example, apatite grains from fresh rocks display yellow to yellow-green luminescence proportional to their Mn and Cl contents, whereas apatite grains from altered rocks display dark green or gray luminescence reflecting their low Mn and Cl contents, similar to that observed in other ore systems (e.g., Bouzari et al., 2016).

The major element variations are echoed in the trace element features in the apatites. For example, apatite from altered rocks, contain much lower total REE concentrations (116 to 9305 ppm) compared to the magmatic apatite grains (2105 to 16009 ppm). Further, hydrothermally influenced apatite is depleted in LREE and Y

(Fig. 2.12d) and has lower La/Yb_N, and La/Sm_N, but higher Sr/Y ratios with minor exceptions (Figs. 2.12 and 2.13). Such trace element signatures are consistent with fluid-rock interaction influencing apatite compositions and co-precipitation of trace element-bearing mineral phases (Harlov and Forster, 2003; Harlov, 2015, Palma et al., 2019).

Dissolution-re-precipitation is common in hydrothermal apatites associated with fluid-rock interaction and results in apatites that have grown in multiple stages and have variable compositions (Harlov et al. 2002; Putnis 2009; Zeng et al. 2016). During the transformation of magmatic apatite to hydrothermal apatite, REE released from magmatic apatite typically form REE-Y-Th-(U)-rich minerals such as monazite and xenotime (Li and Zhou 2015). The depletion in LREE in the hydrothermally altered apatite, and proximity of monazite and xenotime within or around the grains and as inclusions in apatite (Figs. 2.7, 2.12) are consistent with this (Broom-Fendley et al., 2016; Decree et al., 2020; Song et al., 2018).

The formation of monazite and xenotime from apatite involves REE^{3+} remobilization through coupled substitutions ($REE^{3+} + Si^{4+} \leftrightarrow Ca^{2+} + P^{5+}$, or $REE^{3+} + Na^{+} \leftrightarrow 2Ca^{2+}$), which results in REE^{3+} leaching from primary apatite and mass transfer into the fluid, whereas Ca^{2+} and P^{5+} are incorporated in the replaced apatite (Harlov, 2015). Experimental work has also shown that hydrothermal processes can concentrate REEs in the presence of the right transporting ligands, but that LREE are more easily mobilized by metasomatic fluids than HREE (Reed et al., 2000). This would be consistent with what is observed in the hydrothermally influenced apatite from Stog'er Tight and Argyle, which have depletion in LREE and low Th and U (Figs. 2.12c-d). This depletion and

spatial association with monazite-xenotime is consistent with primary fluorapatite having been partially altered and dissolved, with LREE, Th, U, and P released to the carbonic/orogenic fluids, and then subsequently re-precipitated as monazite and lesser xenotime either nearby or as inclusions in apatite.

In addition, hydrothermally modified apatites have two distinct REE patterns, one group is they have some HREE and, in particular, the LREE stripped for growing xenotime and monazite and zircon producing a strong concave down pattern with a positive Eu anomaly; the other group has a concave-down pattern with a strong negative Eu anomaly similar to magmatic apatite, and also has relatively flat REE distributions with negative Eu anomalies with a few displaying very slight LREE enrichment (Fig. 2.15). These features can be also explained by the precipitation of varying amounts of monazite and xenotime proximal to hydrothermal apatite in Stog'er Tight and Argyle, as fluid leaching of apatite leads to LREE and minor HREE (plus Y) release from apatite to hydrothermal fluids (Harlov and Forster, 2002; Harlov and Forster, 2003, Harlov and Forster, 2005; Budzyn et al., 2011; Zang et al., 2020). However, MREEs are commonly retained in apatite during dissolution-precipitation processes due to their higher compatibility in the apatite crystal structure (Prowatke and Klemme, 2006). The varying patterns are due to varying intensity of dissolution-reprecipitation with those hump-shaped pattern apatites having seen more elemental losses during fluid-rock interaction, whereas and those with more normal patterns having been altered but less intensely. This further demonstrates that the intensity of alteration can be detected using trace elements in apatite.

2.8.2.1. Eu anomalies in apatite

The concentration of Eu, which exists as both divalent and trivalent ions in apatite, is controlled by coupled substitutions, allowing Eu to directly substitute for Ca. Eu^{3+} is more readily incorporated into apatite than Eu^{2+} given its similarity in ionic radius to Ca^{2+} compared to Eu^{3+} (Shannon, 1976; Cao et al., 2012), with large Eu^{2+}/Eu^{3+} ratios leading to negative Eu anomalies, whereas small Eu^{2+}/Eu^{3+} ratios lead to positive Eu anomalies in apatite. Cao et al. (2012) suggested that Eu^{2+}/Eu^{3+} ratios in magmatic environments are influenced by oxygen fugacity of the magma. During igneous crystallization, crystallization sequence like plagioclase feldspars and magnetite, or crystallization prior to apatite saturation, can deplete a melt in Eu^{2+} and lead to apatite with negative Eu anomalies (Mao et al., 2016; Krneta et al., 2017). In contrast, dissolution of plagioclase, liberation of Eu^{2+} from plagioclase during fluid-rock interaction could potentially result in hydrothermal apatite that would have potentially positive Eu anomalies. However, if this took place at higher pH fluid-rock conditions where Eu^{3+} is more prevalent it may not result in positive Eu anomalies (>7 at 300 °C, Brugger et al., 2008).

In this study, apatites show both negative and positive Eu anomalies, independent of their origin (Fig. 2.15). Apatites from the distal and weakly altered samples have negative Eu anomalies and Eu/Eu*<1.0. They are intergrown with plagioclase suggesting that apatites formed from the Eu-depleted melt that was left over after Eu^{2+} was incorporated into plagioclase, which has a much higher partition coefficient for Eu than apatite leading to Eu depletions in apatite. Apatites more proximal to mineralization and

in strongly altered samples have higher Eu/Eu*, LREE, and Sr and lower Mn, which are all indicative of increased alteration. The plagioclase in these gabbros generally exhibits sericite alteration, which likely resulted in the liberation of Eu and Sr from plagioclase, which was then incorporated into the hydrothermally influenced apatite, whereas Mn was exchanged with the fluid and transported away from the apatite (ankerite where the excess Mn and Mg are deposited; Figs. 2.13-2.15). This work clearly illustrates the importance of careful integration of petrography, mineral paragenesis and assemblage identification, SEM and CL imaging, and mineral chemistry to determine the origin of Eu/Eu* values in apatite and such integrated approaches are critical for determining the origin and significance of the Eu/Eu* ratio in apatite.

2.8.2.2. The oxidation state of apatite during precipitation: insights from Eu/Eu and Ce/Ce**

The spatial distribution patterns of REE in hydrothermal systems are largely determined by fluid compositions, temperature, pH, and redox conditions (Brugger et al. 2008; Krneta et al. 2017). The magmatic and hydrothermally influenced apatite in Baie Verte gold deposits have distinct chondrite-normalized REE patterns (Fig. 2.15), indicating significant changes in physicochemical conditions during ore-forming processes. According to findings presented herein, the different distribution patterns of REE and trace elements in different types of apatite are mainly dependent on the changes of fluid compositions and/or oxidation state of magmas.

The substitutions of variable valence elements (Mn, Eu, Ce, and S) in apatite have been shown to be influenced by oxygen fugacity (Drake, 1975; Streck and Dilles, 1998;

Sha and Chappell, 1999; Cao et al., 2012; Miles et al., 2014; Pan et al., 2016). The Eu/Eu* and Ce/Ce* values in apatite from this study indicate that the samples crystallized under a variety of relative oxidation states, ranging from moderately reduced (unaltered apatites) to moderately oxidized (altered apatites) to oxidized conditions (altered-hydrothermal apatites with ore, Fig. 2.14a). Orogenic Au fluids generally transport gold as $Au(HS)_2^-$ and are generally near-neutral pH and weakly reducing. Therefore, it is not likely that these alteration-related apatites formed under oxidizing conditions but have apparent "oxidized" signatures due to the sericite forming reaction that caused plagioclase breakdown and donation of elements to the apatite and other alteration phases. Moreover, the gabbros at Stog'er, Argyle, and Animal Pond all have E-MORB to OIB signatures, none of which have significant negative Nb anomalies, common to "arc" rock (e.g., Pawlukiewicz. 2019), which typically form under oxidized conditions (e.g., Richards, 2015). These magmas also crystallized ilmeno-magnetite, which would suggest they were not high fO_2 magmas (e.g., Buddington and Lindsley, 1964).

There is a clear distinction between apatite that are weakly altered to distal having more igneous chondrite normalized signatures, higher Mn contents, and reducing to moderately oxidized Eu/Eu*-Ce/Ce* signatures compared to apatite with altered signatures with hump shaped or variable chondrite normalized REE patterns, lower Mn contents, and apparent oxidized Eu/Eu*-Ce/Ce* signatures (Figs. 2.14a-b). Apatite from the strong/proximal alteration samples overlap but tend towards low Mn and high Eu/Eu* and Sr, suggesting the change of apatite compositions is not caused by variation of oxidation conditions but by the fluid-assisted breakdown of the plagioclase. This

liberated Sr and Eu, which was then incorporated into apatite, and the subsequent release of the Mn^{2+} from the apatites into the ore fluid, and possibly into the coeval hematite alteration seen at these deposits.

These observations illustrate that it requires integration of multiple lines of evidence, including awareness of co-crystallizing phases and nature of fluid-rock and elemental exchange reactions, to fully understanding the oxidation state during precipitation of apatite. Further, using geochemistry alone and Eu/Eu* and Ce/Ce* ratios in apatite are insufficient to document redox conditions during apatite crystallization.

2.8.3. Neodymium isotopic composition variations

The initial $^{143}Nd/^{144}Nd$ values of magmatic and hydrothermally influenced apatites at the time of mineralization (ca. 420 Ma) range from 0.512217 to 0.512435 and 0.512233 to 0.512454, with corresponding $\varepsilon_{Nd}(t)$ = +2.30-6.60 and +2.80-6.96, respectively (Fig. 2.16 and Appendix F). These results suggest that both the igneous and hydrothermally influenced apatites in gabbros associated with Baie Verte gold deposits had relatively homogenous Nd isotopic compositions and similar Nd isotopic sources. Moreover, the samples all have strongly positive $\varepsilon_{Nd}(t)$ values of +2.30 to +6.96 indicating derivation from juvenile sources (Fig. 2.15c), and the general homogeneity of signals across all apatite populations suggests that the Nd isotopic compositions were not significantly affected by hydrothermal alteration. Notably, however, compared to $\varepsilon_{Nd}(t)$ of the depleted mantle reservoir at 420 Ma ($\varepsilon_{Nd}(t)$ = +9.3), the results are lower than the DM and implies involvement of Nd into the apatites from a reservoir with a history of

LREE-enrichment (i.e., Sm/Nd > CHUR) as illustrated by the lithogeochemistry of the host units of these gabbros and the gabbros themselves. Some insight is provided by depleted mantle model (T_{DM}) ages. For samples with $^{147}Sm/^{143}Nd<0.16$, the value considered reliable for depleted mantle model ages (Hamilton et al., 1983), apatite have T_{DM} ages that range from 0.60 Ga to 1.28 Ga (Fig 2.16d.). These ages, while having a considerable range, are consistent with the ages of basement domains within the Baie Verte Peninsula and rocks of the peri-Laurentian realm, and are consistent with at least some Nd having been derived from basement domains during apatite formation. Thus, it is possible that the gabbroic rocks are emplaced over Grenvillian basement then metamorphosed, altered together in the Silurian.

2.8.4. Vectors to Mineralization

Apatite can be used as a petrogenetic indicator, indicator of magmatic-hydrothermal and hydrothermal processes in ore systems, and as an indicator mineral in surficial exploration geochemistry (Sha and Chappell, 1999; Belousova et al., 2002a; Belousova et al., 2002b; Cao et al., 2013; Ding et al., 2015; Bouzari et al., 2016; Mao et al., 2016, Pan et al., 2016; Nathwani et al., 2020; O'Sullivan et al., 2020).

This study contributes to enhancing our understanding of the origin of apatite and its utility in understanding hydrothermal processes and potentially exploration for orogenic gold deposits in the Baie Verte region. In general, there is a strong correlation between hydrothermal mineral assemblages and apatite luminescence and chemistry (e.g., Mn, Cl Sr, Y, and REE concentrations). These data suggest that textural and chemical

features of apatite could be helpful for vectoring towards mineralization on the Baie Verte Peninsula, but potentially application in other greenschist-facies mafic-hosted gold environments worldwide where apatite may also likely be common. From this work, key vectors to mineralization within the Animal Pond Prospect, and Stog'er and Argyle deposits include:

Mineral assemblages: apatite that is spatially associated with gold is typically associated with subhedral to euhedral pyrite where gold typically occurs as a fine inclusion within pyrite or in fractures near pyrite grain margins. The reaction of Au (as $Au(HS)_2^-$) and CO_2-Na-REE-Y-bearing fluids with Fe-Ti-rich host rocks resulted in wall rock sulfidation and pyrite formation, which led to gold deposition (Piercey and Copeland, 2017). Gold is also associated with not only hydrothermally influenced apatite, but also hydrothermal zircon, monazite ($(Ce,La)PO_4$) and xenotime (YPO_4) and these phosphate minerals are widely distributed throughout the Au-related hydrothermal alteration zones (see also Ramezani et al., 2000). The deposition of gold occurred concurrently with dissolution and precipitation processes in apatite, resulting in leaching of REE from apatite and the subsequent precipitation of coeval hydrothermal monazite and xenotime.

CL of apatite: cathodoluminescence reveals significant differences between magmatic and hydrothermally influenced apatite. Therefore, cathodoluminescence imaging can provide a fast-screening tool to assess hydrothermally influenced apatite from an orogenic Au deposit before detailed analysis by electron microprobe. The physical–chemical conditions of hydrothermal fluids can be potentially inferred from

apatite textures (e.g., heterogeneous patchy patterns and spatial association with hydrothermal monazite and xenotime). The occurrence of apatite grains with subdued grey/dark green colors under CL provides a specific characteristic to identify apatites that have been influenced by hydrothermal activity.

Geochemistry: hydrothermally influenced apatite generally has LREE-, Cl- and Mn-depletion, elevated Sr and Sr/Y ratios, and higher Eu/Eu* values, and humped MREE-rich, convex chondrite normalized REE patterns, compared to igneous apatite which have LREE-rich signatures and distinctive chondrite-normalized REE patterns. These features are a product of orogenic Au fluid-rock interaction and the destruction and subsequent redistribution of elements from primary igneous phases into secondary hydrothermal phosphates, including apatite, monazite, and xenotime.

Collectively these features may be applicable to apatite in orogenic Au systems, but also may be useful for discriminating apatite in heavy mineral concentrates in stream sediments and other surface media during surficial exploration in projects.

2.8.5. Conclusions

The studied apatite, representing a range of alteration types and intensities from three gabbro hosted orogenic gold deposits (Stog'er and Argyle deposits and the Animal Pond Prospect) in Baie Verte, Newfoundland Appalachians, demonstrate that apatite textural features determined through/by CL and BSE imaging, halogen concentrations, and apatite major and trace element concentrations can be used to unravel the magmatic and hydrothermal history of the orogenic gold deposits. The in situ geochemical analyses

show that magmatic and hydrothermally influenced apatites contain similar $\varepsilon_{Nd}(t)$ values but exhibit considerable textural and compositional variations depending on intensity of alteration and mineral associations. The following conclusions can be summarized:

(1) textural observations on apatite from the Animal Pond prospect, Stog'er, and Argyle deposits suggest the modification of primary (magmatic) apatites by interaction with hydrothermal fluids;

(2) apatites in fresh rocks show homogeneous textures and distinct luminescence (yellow-to-yellow-green). Magmatic apatite contains the highest concentrations of Mn, Mg, and Cl;

(3) apatites in altered rocks show dark green to gray luminescence, are depleted in Mn, Cl, LREE (low La/Yb_N, La/Sm_N), Th, and U, and enriched in Sr and Sr/Y compared to apatite in the fresh rocks. This is compatible with the altered apatites having experienced fluid interactions that caused REE-Mn-Cl-Th-U remobilization and subsequent growth of hydrothermal monazite and lesser xenotime inclusions;

(4) the apatite in fresh and altered rocks in Animal Pond Prospect, Stog'er Tight, and Argyle deposits have distinct chondrite-normalized REE patterns indicating significant changes in physicochemical conditions during ore-forming processes. Magmatic apatite has LREE enriched with concave downwards patters, with negative Eu anomalies although they are relatively flat compared to many of the altered apatites. Hydrothermally influenced apatites show two distinct REE patterns, the first group is relatively enriched

in MREE producing a strong concave down pattern (hump pattern) with positive Eu anomaly; the second group is concave down pattern with a strong negative Eu anomaly similar to magmatic apatite;

(5) the deposition of gold occurred concurrently with the dissolution and precipitation of apatite, which caused the leaching of REE from apatite and the coeval precipitation of hydrothermal monazite and xenotime;

(6) Nd isotopic data indicates that the gabbroic magmas were derived from juvenile sources and that Nd isotopic compositions were not changed during hydrothermal alteration. Compared to $\varepsilon_{Nd}(t)$ of the depleted mantle reservoir at 420 Ma, the results are lower than the DM and implies involvement of Nd into the apatites from a reservoir with a history of LREE-enrichment; and

(7) this study illustrates that igneous apatite can be modified by hydrothermal fluids during fluid-rock interaction and can be used to determine igneous vs hydrothermally influenced apatite in orogenic Au and likely other hydrothermal systems.

2.8.6. References

Anderson, S., Jamieson, R. A., Reynolds, P., and Dunning, G., 2001, Devonian extension in northwestern Newfoundland: $^{40}Ar/^{39}Ar$ and U-Pb data from the Ming's Bight area, Baie Verte Peninsula: Journal of Geology, v. 109, p. 191–211.

Bédard, J. H., 1999, Petrogenesis of boninites from the Betts Cove ophiolite, Newfoundland, Canada: identification of subducted source components: Journal of Petrology, v. 40, p. 1853–1889.

Bédard, J. H., Lauziere, K., Tremblay, A., Sangster, A. L., Douma, S., and Dec, T., 2000, Betts Cove ophiolite and its cover rocks: Geological Survey of Canada Bulletin, v. 550, 76 p.

Bédard, J.H., Lauziere, K., Tremblay, A., Sangster, A.L., and Tellier, M., 1998, Evidence from Betts Cove ophiolite boninites for forearc seafloor spreading: Tectonophysics, v. 284, p. 233-245.

Belousova, E. A., Walters, S., Griffin, W. L., and O'reilly, S. Y., 2001, Trace-element signatures of apatites in granitoids from the Mt Isa Inlier, northwestern Queensland: Australian Journal of Earth Sciences, v. 48, p. 603-619.

Belousova, E.A., Griffin, W.L., O'Reilly, S.Y., and Fisher, N.I., 2002a, Apatite as an indicator mineral for mineral exploration: Trace-element compositions and their relationship to host rock type: Journal of Geochemical Exploration, v. 76, p. 45–69.

Belousova, E.A., Griffin, W.L., O'Reilly, S.Y., and Fisher, N.I., 2002b, Igneous zircon: Trace element composition as an indicator of source rock type: Contributions to Mineralogy and Petrology, v. 143, p. 602–622.

Betkowski, W. B., Harlov, D. E., and Rakovan, J. F., 2016, Hydrothermal mineral replacement reactions for an apatite-monazite assemblage in alkali-rich fluids at 300–600° C and 100 MPa: American Mineralogist, v. 101, p. 2620-2637.

Boudreau, A. E., Love C., Hoatson, D. M., 1993, Variation in the composition of apatite in the Munni Munni Complex and associated intrusions of the West Pilbara Block, Western Australia: Geochimica et Cosmochimica Acta, v. 57, p. 4467–4477.

Bouzari, F., Hart, C.J.R., Bissig, T., and Barker, S., 2016, Hydrothermal alteration revealed by apatite luminescence and chemistry: A potential indicator mineral for exploring covered porphyry copper deposits: Economic Geology, v. 111, p. 1397–1410.

Boyce, J. W., and Hervig, R. L., 2009, Apatite as a monitor of late-stage magmatic processes at Volcán Irazú, Costa Rica: Contributions to Mineralogy and Petrology, v. 157, p. 135-145.

Broom-Fendley, S., Styles, M. T., Appleton, J. D., Gunn, G., and Wall, F., 2016, Evidence for dissolution-reprecipitation of apatite and preferential LREE mobility in carbonatite-derived late-stage hydrothermal processes: American Mineralogist, v. 101, p. 596-611.

Broom-Fendley, S., Brady, A. E., Wall, F., Gunn, G., and Dawes, W., 2017, REE minerals at the Songwe Hill carbonatite, Malawi: HREE-enrichment in late-stage apatite: Ore Geology Reviews, v. 81, p. 23-41.

Bruand, E., Storey, C., Fowler, M., 2014, Accessory mineral chemistry of high Ba–Sr granites from northern Scotland: constraints on petrogenesis and records of whole-rock signature; Journal of Petrology, v. 55, p. 1619–1651.

Bruand, E., Storey, C., and Fowler, M., 2016, An apatite for progress: Inclusions in zircon and titanite constrain petrogenesis and provenance, Geology, v. 44, p. 91-94.

Bruand, E., Fowler, M., Storey, C., Darling, J., 2017, Apatite trace element and isotope applications to petrogenesis and provenance: American Mineralogist, v. 102, p. 75–84.

Brugger, J., Etschmann, B., Pownceby, M., Liu, W., Grundler, P., and Brewe, D., 2008, Oxidation state of europium in scheelite: tracking fluid–rock interaction in gold deposits: Chemical Geology, v. 257, p. 26-33.

Buddington, A. F. and Lindsley, D. H., 1964, Iron-titanium oxide minerals and dynthetic equivalents: Journal of Petrology, v. 5, p. 310-357.

Budzyń, B., Harlov, D. E., Williams, M. L., and Jercinovic, M. J., 2011, Experimental determination of stability relations between monazite, fluorapatite, allanite, and REE-epidote as a function of pressure, temperature, and fluid composition: American Mineralogist, v. 96, p. 1547-1567.

Campbell, L. S., and Henderson, P., 1997, Apatite paragenesis in the Bayan Obo REE-Nb-Fe ore deposit: Inner Mongolia, China: Lithos, v. 42, p. 89-103.

Cao, M.J., Li, G.M., Qin, K.Z., Seitmuratova, E.Y., and Liu, Y.S., 2012, Major and trace element characteristics of apatites in granitoids from Central Kazakhstan:

Implications for petrogenesis and mineralization: Resource Geology, v. 62, p. 63–83.

Cao, M.J, Evans, N. J., Hollings, P., Cooke, D. R., McInnes, B. I., and Qin, K., 2021, Apatite texture, composition, and O-Sr-Nd isotope signatures record magmatic and hydrothermal fluid characteristics at the Black Mountain porphyry deposit, Philippines: Economic Geology, v. 116, p. 1189-1207.

Cao, M. J., Zhou, Q. F., Qin, K. Z., Tang, D. M., and Evans, N. J., 2013, The tetrad effect and geochemistry of apatite from the Altay Koktokay No. 3 pegmatite, Xinjiang, China: implications for pegmatite petrogenesis: Mineralogy and Petrology, v. 107, p. 985-1005.

Castonguay, S., Skulski, T., van Staal, C., and Currie, M., 2009, New insights on the structural geology of the Pacquet Harbour Group and Point Rousse Complex, Baie Verte Peninsula, Newfoundland: Newfoundland and Labrador Department of Natural Resources, Geological Survey, Report 09-1, p. 147–158.

Castonguay, S., van Staal, C. R., Joyce, N., Skulski, T., and Hibbard, J. P., 2014, Taconic metamorphism preserved in the Baie Verte Peninsula, Newfoundland Appalachians: Geochronological evidence for ophiolite obduction and subduction and exhumation of the leading edge of the Laurentian (Humber) margin during closure of the Taconic Seaway: Geoscience Canada, v. 41, p. 459–482.

Cawood, P.A., and Dunning, G.R., 1993, Silurian age for movement on the Baie Verte Line: implications for accretionary tectonics in the Northern Appalachians: Geological Society of America, Abstracts with Programs, v. 25, p. A422.

Chakhmouradian, A. R., Reguir, E. P., Zaitsev, A. N., Couëslan, C., Xu, C., Kynický, J., Mumin, A. H., and Yang, P., 2017, Apatite in carbonatitic rocks: Compositional variation, zoning, element partitioning and petrogenetic significance: Lithos, v. 274, p. 188-213.

Chu, M., Wang, K., Griffin, W., Chung, S., O'Reilly, S., Pearson, N., and Iizuka, Y., 2009, Apatite composition: Tracing petrogenetic processes in Transhimalayan granitoids: Journal of Petrology, v. 50, p. 1829–1855.

Cousineau, P. A., and Bédard, J. H., 2000, Sedimentation in a subaqueous arc/back-arc setting: the Bobby Cove Formation, Snooks Arms Group, Newfoundland: Precambrian Research, v. 101, p. 111-134.

Cullen, M., Pitman, C., Copeland, D. A., McNeill, P., and Slepcev, G., 2018, Mineral resource and mineral reserve update on the Point Rousse Project, Baie Verte, Newfoundland and Labrador, Canada, NI-43-101 Technical Report: Anaconda Mining Inc., Newfoundland and Labrador, Canada, 285 p.

Decrée, S., Cawthorn, G., Deloule, E., Mercadier, J., Frimmel, H., and Baele, J. M., 2020, Unravelling the processes controlling apatite formation in the Phalaborwa Complex (South Africa) based on combined cathodoluminescence, LA-ICPMS

and in-situ O and Sr isotope analyses: Contributions to Mineralogy and Petrology, v. 175, p. 1-31.

Ding, T., Ma, D., Lu, J., and Zhang, R., 2015, Apatite in granitoids related to polymetallic mineral deposits in southeastern Hunan Province, Shi–Hang zone, China: implications for petrogenesis and metallogenesis; Ore Geology Reviews, v. 69, p. 104-117.

Drake, M. J., 1975, The oxidation state of europium as an indicator of oxygen fugacity: Geochimica et Cosmochimica Acta, v. 39, p. 55-64.

Dubé, B., Lauzière, K., and Poulsen, H. K., 1993, The Deer Cove deposit: an example of "thrust"- related breccia-vein type gold mineralization in the Baie Verte Peninsula, Newfoundland: Geological Survey of Canada, Current Research, Paper 93-1D, p. 1–10.

Dunning, G. R., Krogh, T. E., 1985, Geochronology of ophiolites of the Newfoundland Appalachians: Canadian Journal of Earth Sciences, v. 22, p. 1659-1670.

Elliot, J.C., 1994, Structure and chemistry of the apatites and other calcium orthophosphates: Elsevier, Amsterdam, 389 p.

Emerson, N. R., Simo, J. T., Byers, C. W., and Fournelle, J., 2004, Correlation of (Ordovician, Mohawkian) K-bentonites in the upper Mississippi valley using apatite chemistry: implications for stratigraphic interpretation of the mixed

carbonate-siliciclastic Decorah Formation: Palaeogeography, Palaeoclimatology, Palaeoecology, v. 210, p. 215-233.

Evans, D. T. W., 2004, Epigenetic gold occurrences, Baie Verte Peninsula, (NTS 12H/09, 16 and 12I/01) Newfoundland: Government of Newfoundland and Labrador, Department of Natural Resources, Geological Survey, Mineral Resource Report No. 11, 157 p.

Frietsch, R., Perdahl, J. A., 1995, Rare-earth elements in apatite and magnetite in Kiruna-type iron-ores and some other iron-ore types: Ore Geology, v. 9, p. 489–510.

Gelcich, S., Davis, D. W., and Spooner, E. T., 2005, Testing the apatite-magnetite geochronometer: U-Pb and 40Ar/39Ar geochronology of plutonic rocks, massive magnetite-apatite tabular bodies, and IOCG mineralization in Northern Chile: Geochimica et Cosmochimica Acta, v. 69, p. 3367-3384.

Goldstein, S. L., O'nions, R. K., and Hamilton, P. J., 1984, A Sm-Nd isotopic study of atmospheric dusts and particulates from major river systems: Earth and planetary Science Letters, v. 70, p. 221-236.

Goldfarb, R. J. and Groves, D. I., 2015, Orogenic gold: common or evolving fluid and metal sources through time: Lithos, v. 233, p. 2–26.

Götze, J., 2012, Application of cathodoluminescence microscopy and spectroscopy in geosciences: Microscopy and Microanalysis, v. 18, p. 1270-1284.

Götze, J., Schertl, H. P., Neuser, R. D., Kempe, U., and Hanchar, J. M., 2013, Optical microscope-cathodoluminescence (OM–CL) imaging as a powerful tool to reveal internal textures of minerals: Mineralogy and Petrology, v. 107, p. 373-392.

Gros, K., Słaby, E., Förster, H. J., Michalak, P. P., Munnik, F., Götze, J., and Rhede, D., 2016, Visualization of trace-element zoning in fluorapatite using BSE and CL imaging, and EPMA and μPIXE/μPIGE mapping: Mineralogy and Petrology, v. 110, 809-821.

Hamilton, P. J., O'nions, R. K., Bridgwater, D., and Nutman, A., 1983, Sm-Nd studies of Archaean metasediments and metavolcanics from West Greenland and their implications for the Earth's early history: Earth and Planetary Science Letters, v. 62, p. 263-272.

Harlov, D.E., 2015, Apatite: a fingerprint for metasomatic processes: Elements, v. 11, p. 171–176.

Harlov, D.E., and Förster, H.J., 2003, Fluid-induced nucleation of REE phosphate minerals in apatite: Nature and experiment. Part II. Fluorapatite: American Mineralogist, v. 88, p. 1209–1229.

Harlov, D.E., Andersson, U.B., Förster, H.J., Nyström, J.O., Dulski, P., and Broman, C., 2002, Apatite-monazite relations in the Kiirunavaara magnetite-apatite ore, northern Sweden: Chemical Geology, v. 191, p. 47–72.

Harlov, D.E., Wirth, R., and Förster, H.J., 2005, An experimental study of dissolution-reprecipitation in fluorapatite: Fluid infiltration and the formation of monazite: Contributions to Mineralogy and Petrology, v. 150, p. 268–286.

Hibbard, J., 1983, Geology of the Baie Verte Peninsula, Newfoundland: Government of Newfoundland and Labrador, Department of Mines and Energy, Mineral Development Division, Memoir 2, 280 p.

Hsieh, P. S., Chen, C. H., Yang, H. J., and Lee, C. Y., 2008, Petrogenesis of the Nanling Mountains granites from South China: constraints from systematic apatite geochemistry and whole-rock geochemical and Sr–Nd isotope compositions.: Journal of Asian Earth Sciences, v. 33, p. 428-451.

Hughes, J.M., and Rakovan, J.F., 2015, Structurally robust, chemically diverse: Apatite and apatite supergroup minerals: Elements, v. 11, p. 165–170.

Jacobsen, S. B. and Wasserburg, G. J., 1980, Sm-Nd Isotopic Systematics of Chondrites and Achondrites: Meteoritics, v. 15, 307 p.

Kempe, U., and Götze, J., 2002, Cathodoluminescence (CL) behaviour and crystal chemistry of apatite from rare-metal deposits: Mineralogical Magazine, v. 66, p. 151–172.

Kerr, A. and Selby, D., 2012, The timing of epigenetic gold mineralization on the Baie Verte Peninsula, Newfoundland, Canada: new evidence from Re-Os pyrite geochronology: Mineralium Deposita, v. 47, p. 325–337.

Kessler, L. G., and Bédard, J. H., 2000, Epiclastic volcanic debrites-evidence of flow transformations between avalanche and debris flow processes, Middle Ordovician, Baie Verte Peninsula, Newfoundland, Canada: Precambrian Research, v. 101, 135-161.

Ketcham, R. A., 2015, Calculation of stoichiometry from EMP data for apatite and other phases with mixing on monovalent anion sites: American Mineralogist, v. 100, p. 1620-1623.

Kirkwood, D., and Dubé, B., 1992, Structural control of sill-hosted gold mineralization: the Stog'er Tight gold deposit, Baie Verte Peninsula, northwestern Newfoundland: Geological Survey of Canada, Current Research, Paper 92-1D, p. 211–221.

Krneta, S., Ciobanu, C. L., Cook, N. J., Ehrig, K., and Kontonikas-Charos, A., 2017, Rare earth element behaviour in apatite from the Olympic Dam Cu–U–Au–Ag deposit, South Australia: Minerals, v. 7, 135 p.

Kuntz, G., Robinson, J., McNeill, P., Bullock, K., and Budgell C., 2021, Mineral resource and mineral reserve update on the Point Rousse Project, Baie Verte, Newfoundland and Labrador, Canada, NI-43-101 Technical Report: Anaconda Mining Inc., Newfoundland and Labrador, Canada, 271 p.

Li, X.C., and Zhou, M.F., 2015, Multiple stages of hydrothermal REE remobilization recorded in fluorapatite in the Paleoproterozoic Yinachang Fe- Cu-(REE) deposit, Southwest China: Geochimica et Cosmochimica Acta, v. 166, p. 53–73.

Mao, M., Rukhlov, A.S., Rowins, S.M., Spence, J., and Coogan, L.A., 2016, Apatite trace element compositions: A robust new tool for mineral exploration: Economic Geology, v. 111, p. 1187–1222.

Mariano, A. N., 1988, Some further geological applications of cathodoluminescence, in: Marshall D. J. (ed.) Cathodoluminescence of geological materials, Unwin Hyman, Boston, p. 94-123.

Marfunin, A.S., 1979, Spectroscopy, luminescence and radiation centers in minerals: Springer-Verlag Berlin, 352 p.

McCubbin, F. M., Jones, R. H., 2015, Extraterrestrial apatite: planetary geochemistry to astrobiology: Elements, v.11, p. 183–188.

McDonough, W.F., Sun, S., 1995, The composition of the Earth: Chemical Geology, v.120, p. 223–253.

Mercer, C.N., Watts, K.E., Gross, J., 2020, Apatite trace element geochemistry and cathodoluminescent textures – a comparison between regional magmatism and the Pea Ridge IOAREE and Boss IOCG deposits, southeastern Missouri iron metallogenic province, USA: Ore Geology Reviews, v.116, 103129 p.

Migdisov, A. A., and Williams-Jones, A. E., 2014, Hydrothermal transport and deposition of the rare earth elements by fluorine-bearing aqueous liquids: Mineralium Deposita, v. 49, p. 987-997.

Miles, A. J., Graham, C. M., Hawkesworth, C. J., Gillespie, M. R., Hinton, R., 2014, Evidence for distinct stages of magma history recorded by the compositions of accessory apatite and zircon: Contributions to Mineralogy and Petrology, v. 166, p. 1-19.

Mitchell, R. H., and Coulson, I. M., 2014, Cathodoluminescence of apatite: Cathodoluminescence and its Application to Geoscience, v. 45, p. 143-167.

Nathwani, C. L., Loader, M. A., Wilkinson, J. J., Buret, Y., Sievwright, R. H., and Hollings, P., 2020, Multi-stage arc magma evolution recorded by apatite in volcanic rocks: Geology, v. 48, p. 323-327.

O'Reilly, S. Y., and Griffin, W. L., 2000, Apatite in the mantle: implications for metasomatic processes and high heat production in Phanerozoic mantle: Lithos, v. 53, p. 217-232.

O'Sullivan, G., Chew, D., Kenny, G., Henrichs, I., and Mulligan, D., 2020, The trace element composition of apatite and its application to detrital provenance studies: Earth-Science Reviews, v. 201, p. 103044.

Pagel, M., Barbin, V., Blanc, P., and Ohnenstetter, D., 2000, Cathodoluminescence in geosciences: an overview and perspectives. In Pagel M., Barbin V., Blanc P., and Ohnenstetter D. (eds), Cathodoluminescence in Geosciences: Springer Verlag, p. 1-21.

Palma, G., Barra, F., Reich, M., Valencia, V., Simon, A.C., Vervoort, J., Leisen, M., and Romero, R., 2019, Halogens, trace element concentrations, and Sr-Nd isotopes in apatite from iron oxide-apatite (IOA) deposits in the Chilean iron belt: evidence for magmatic and hydrothermal stages of mineralization: Geochimica et Cosmochimica Acta, v. 246, p. 515–540.

Pan, Y.M., and Fleet, M.E., 2002, Compositions of the apatite-group minerals: Substitution mechanisms and controlling factors: Reviews in Mineralogy and Geochemistry, v. 48, p. 13–49.

Pan, L. C., Hu, R. Z., Wang, X. S., Bi, X. W., Zhu, J. J., and Li, C., 2016, Apatite trace element and halogen compositions as petrogenetic-metallogenic indicators: examples from four granite plutons in the Sanjiang region, SW China: Lithos, v. 254, p. 118-130.

Pasero, M., Kampf, A. R., Ferraris, C., Pekov, I. V., Rakovan, J., and White, T. J., 2010, Nomenclature of the apatite supergroup minerals: European Journal of Mineralogy, v. 22, p. 163-179.

Patiño-Douce A. E., Roden M. F., Chaumba J., Fleisher C., and Yogodzinski G., 2011, Compositional variability of terrestrial mantle apatites, thermodynamic modeling of apatite volatile contents, and the halogen and water budgets of planetary mantles: Chemical Geology, v. 288, p. 14– 31.

Paton, C., Hellstrom, J., Paul, B., Woodhead, J., and Hergt, J., 2011, Iolite: freeware for the visualisation and processing of mass spectrometric data: Journal of Analytical Atomic Spectrometry, v. 26, p. 2508-2518.

Pawlukiewicz, M., 2019, Hydrothermal reconstruction and lithogeochemistry of the Argyle orogenic gold deposit, Baie Verte, Newfoundland, Canada, MSc thesis, Memorial University of Newfoundland, St. John's, NL, Canada, 421 p.

Piccoli P. M., Candela P. A., 2002, Apatite in igneous systems: Reviews in Mineralogy and Geochemistry, v. 48, p. 55–292.

Piercey, S. J. and Copeland, D. A., 2017, Host-rock reactivity in the generation of gabbro-hosted orogenic Au in the Baie Verte Peninsula, Newfoundland, Canada: GAC-Newfoundland and Labrador Section, 2017 Spring Technical Meeting, Program with Abstracts, St. John's, Newfoundland, v. 53, p. 250.

Portnov, A.M. and Gorobets, B.S., 1969, Luminescence of apatite from different rock types: Doklady Akademia Nauk SSSR, v. 184, p. 110 -115 (in Russian).

Prowatke, S., and Klemme, S., 2006, Trace element partitioning between apatite and silicate melts: Geochimica et Cosmochimica Acta, v.70, p. 4513-4527.

Putnis, A., 2009, Mineral replacement reactions: Reviews in Mineralogy and Geochemistry, v. 70, p. 87-124.

Raimbault, L., Baumer, A., Dubru, M., Benkerrou, C., Croze, V., and Zahm, A., 1993, REE fractionation between scheelite and apatite in hydrothermal conditions: American Mineralogist, v. 78, p. 1275-1285.

Ramezani, J., 1992, The geology, geochemistry and U-Pb geochronology of the Stog'er Tight Gold Prospect, Baie Verte Peninsula, Newfoundland, M.Sc. thesis, Memorial University of Newfoundland, St. John's, Newfoundland, 312 p.

Ramezani, J., Dunning, G. R., and Wilson, M. R., 2000, Geologic setting, geochemistry of alteration, and U-Pb age of hydrothermal zircon from the Silurian Stog'er Tight Gold Prospect, Newfoundland Appalachians, Canada: Exploration and Mining Geology, v. 9, p. 171-188.

Reed M. J., Candela P. A., and Piccoli P. M., 2000, The distribution of rare earth elements between monzogranitic melt and the aqueous volatile phase in experimental investigations at200 MPa and 800 oC: Contributions to Mineralogy and Petrology, v.140, p. 251–262.

Richards, J. P., 2015, The oxidation state, and sulfur and Cu contents of arc magmas: implications for metallogeny: Lithos, v. 233, p. 27-45.

Ritcey, D. H., Wilson, M. R., and Dunning, G. R., 1995, Gold mineralization in the Paleozoic Appalachian Orogen; constraints from geologic, U/Pb, and stable isotope studies of the Hammer Down Prospect, Newfoundland: Economic Geology, v. 90, p. 1955-1965.

Roeder, P.L., MacArthur, D., Ma, X.-P., Palmer, G.R. and Mariano, A.N., 1987, Cathodoluminescence and microprobe study of rare-earth elements in apatite: American Mineralogist, v. 72, p. 801-811.

Sangster A. L., Douma S., and Lavigne J., 2008, Base metal and gold deposits of the Betts Cove Complex, Baie Verte Peninsula, Newfoundland, in: Goodfellow WD (ed) Mineral deposits of Canada: a synthesis of major deposit types, district metallogeny, the evolution of metallogenic provinces, and exploration methods: Geological Association of Canada, Mineral Deposits Division, Special Publications No. 5, p. 703–723.

Sha, L.K., and Chappell, B.W., 1999, Apatite chemical composition, determined by electron microprobe and laser-ablation inductively coupled plasma mass spectrometry, as a probe into granite petrogenesis: Geochimica et Cosmochimica Acta, v. 63, p. 3861–3881.

Shannon, R.D., 1976, Revised effective ionic radii and systematic studies of interatomic distances in halides and chalcogenides: section A: crystal physics, diffraction, theoretical and general crystallography, v. 32, p. 751–767.

Shaw, G.H., 2003, Trace element chemistry of volcanic apatite phenocrysts as a tool for fingerprinting altered volcanic ash beds: Assessing interbed and intrabed variation at local and regional scales: GSA Bulletin, v. 115, p. 933-942.

Skulski, T., Castonguay, S., van Staal, C. R., Rogers, N., McNicoll, V., Kerr, A., and Escayola, M., 2009, Baie Verte Peninsula: an evolving geological story:

Geological Association of Canada, Newfoundland and Labrador Section, Annual Field Trip Guide, St. John's, Newfoundland, 60 p.

Skulski, T., Castonguay, S., McNicoll, V., van Staal, C., Kidd, W., Rogers, N., Morris, W., Ugalde, H., Slavinski, H., and Spicer, W., 2010, Tectonostratigraphy of the Baie Verte oceanic tract and its ophiolite cover sequence on the Baie Verte Peninsula: Geological Survey, Newfoundland and Labrador Department of Natural Resources, Current Research, Report 10-1, p. 315–337.

Song, D., Glorie, S., Xiao, W., Collins, A.S., Gillespie, J., Jepson, G., and Li, Y., 2018, Tectonothermal evolution of the southwestern Alxa Tectonic Belt, NW China: constrained by apatite U-Pb and fission track thermochronology: Tectonophysics, v. 722, p. 577–594.

Sparrow, B., Barrett, S., Copeland, D. A., and Walsh, M., 2017, Argyle Prospect Mineral Licences 012433M (11th year) and 020060M (5th year) Point Rousse Project, Baie Verte Peninsula, NL NTS sheet 12H/16, Assessment Report: Anaconda Mining Inc., Newfoundland and Labrador, Canada, 481 p.

Steiger, R.H. and Jager, E., 1977, Subcommission on geochronology: convention on the use of decay constants in geo and cosmochronology: Earth Planetary Science Letters, v. 36, p. 359-362.

Streck, M. J., and Dilles, J. H., 1998, Sulfur evolution of oxidized arc magmas as recorded in apatite from a porphyry copper batholith: Geology, v. 26, p. 523-526.

Stormer, J. C., Pierson, M. L., and Tacker, R. C., 1993, Variation of F and Cl X-ray intensity due to anisotropic diffusion in apatite during electron microprobe analysis: American Mineralogist, v. 78, p. 641-648.Taylor, S.R., and McLennan, S.M., 1985, The continental crust: Its composition and evolution: Oxford, Blackwell Scientific Publications, p. 31.

Tepper J. and Kuehner S., 1999, Complex zoning in apatite from the Idaho Batholith; a record of magma mixing and intracrystalline trace element diffusion: American Mineralogist, v. 4, p. 581–595.

van Staal, C. R., 2007, Pre-Carboniferous tectonic evolution and metallogeny of the Canadian Appalachians: in Goodfellow, W. D., ed. Mineral Deposits of Canada: A Synthesis of Major Deposit Types, District Metallogeny, the Evolution of Geological Provinces and Exploration Methods: Geological Association of Canada, Mineral Deposits Division, Special Publications No. 5, p. 793–818.

van Staal, C. R., Barr, S. M., and Percival, J., 2012, Lithospheric architecture and tectonic evolution of the Canadian Appalachians and associated Atlantic Margin: in Percival, J. A., Cook, F. A. and Clowes, R. M., eds., Tectonic styles in Canada: the LITHOPROBE perspective: Geological Association of Canada, Special Paper 49, p. 41-95.

Waychunas, G.A., 2002, Apatite luminescence: Reviews in Mineralogy and Geochemistry, v. 48, p. 710–742.

Webster, J. D., and Piccoli, P. M., 2015, Magmatic apatite: A powerful, yet deceptive, mineral: Elements, v. 11, p. 177-182.

Williams, H., 1979, Appalachian orogen in Canada: Canadian Journal of Earth Sciences, v. 16, p. 792–807.

Williams, H., Colman-Sadd, S. P., and Swinden, H. S., 1988, Tectonic-stratigraphic subdivisions of central Newfoundland: Geological Survey of Canada, Current Research, Paper 88-1B, p. 91–98.

Williams, H., and Grant, A.C., 1998, Tectonic Assemblages map scale 1:3000000, Atlantic Region, Canada: Geological Survey of Canada, Open File 3657.

Williams, H. and St. Julien, P. 1982, The Baie Verte Brompton Line: Early Paleozoic continent ocean interface in the Canadian Appalachians. In Major Structural Zones and Faults of the northern Appalachians. Edited by P. St. Julien and J. Beland. Geological Association of Canada, Special Paper 24, pp.177–208.

Williams-Jones, A. E., Bowell, R. J., and Migdisov, A. A., 2009, Gold in solution: Elements, v. 5, p. 281–287.

Yang, Y. H., Wu, F. Y., Yang, J. H., Chew, D. M., Xie, L. W., Chu, Z. Y., and Huang, C., 2014, Sr and Nd isotopic compositions of apatite reference materials used in U–Th–Pb geochronology: Chemical Geology, v. 385, p. 35-55.

Ybarra, S., Piercey, S., Layne, G. D., Copeland, D. A., and McNeil, P., 2017, Alteration halo and lithogeochemistry of the Pine Cove orogenic gold deposit, Baie Verte

Peninsula, Newfoundland, Canada: GAC-Newfoundland and Labrador Section, 2017 Spring Technical Meeting, Program with Abstracts, St. John's, Newfoundland: Atlantic Geology, p. 250.

Zeng, L. P., Zhao, X. F., Li, X. C., Hu, H., and McFarlane, C., 2016, In situ elemental and isotopic analysis of fluorapatite from the Taocun magnetite-apatite deposit, Eastern China: Constraints on fluid metasomatism: American Mineralogist, v. 101, p. 2468-2483.

Zhang, X.B., Guo, F., Zhang, B., Zhao, L., Wu, Y.M., Wang, G.Q., Alemayehu, M., 2020, Magmatic evolution and post-crystallization hydrothermal activity in the early cretaceous Pingtan intrusive complex, SE China: records from apatite geochemistry: Contributions to Mineralogy and Petrology, v. 175, p. 25.

Zhao, X. F., Zhou, M. F., Gao, J. F., Li, X. C., and Li, J. W., 2015, In situ Sr isotope analysis of apatite by LA-MC-ICPMS: constraints on the evolution of ore fluids of the Yinachang Fe-Cu-REE deposit, Southwest China: Mineralium Deposita, v. 50, p. 871-884.

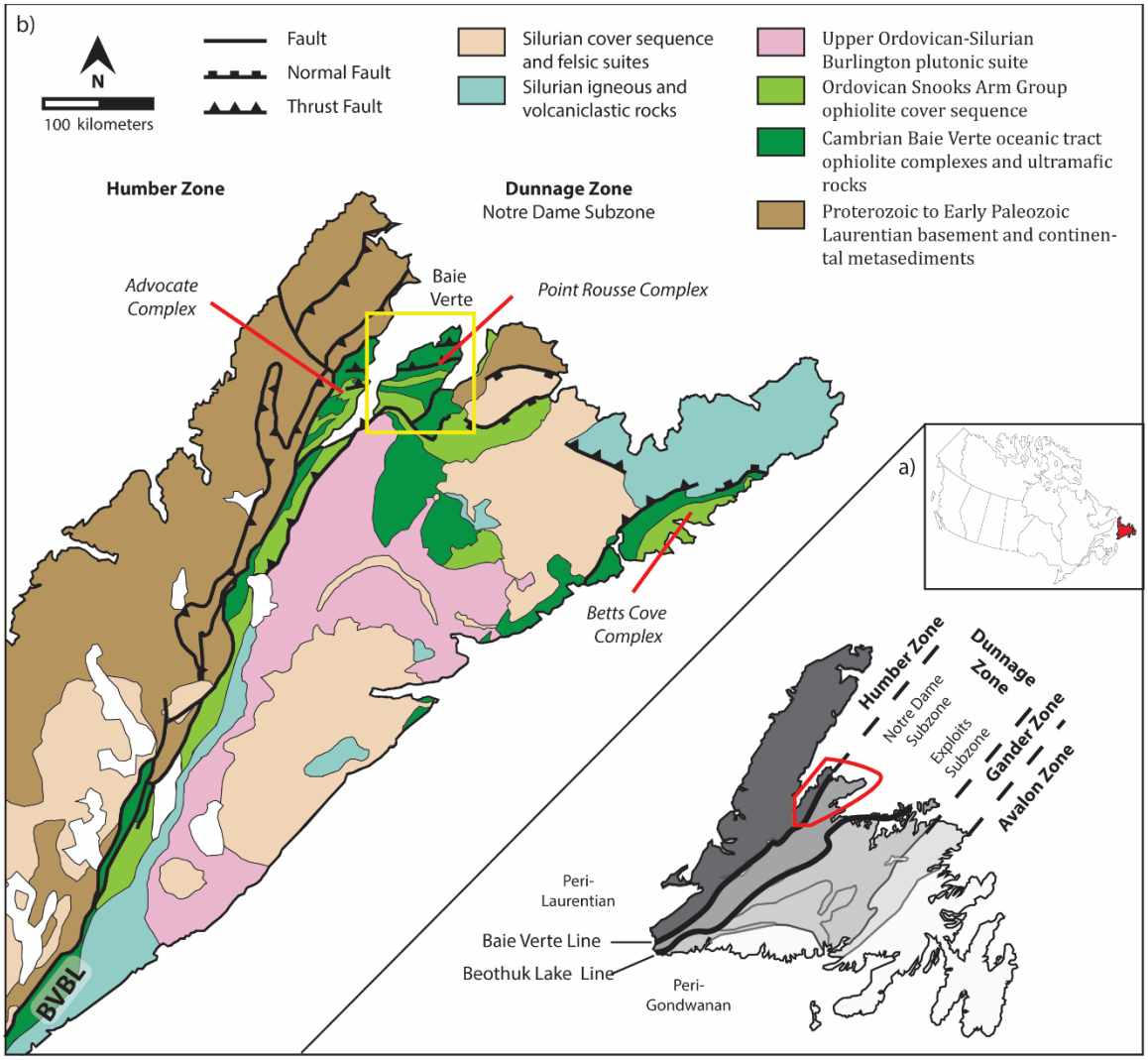

Figure 2.1. a) Simplified map of tectonostratigraphic terranes of Newfoundland (modified after Williams, 1979 and Williams et al., 1988); b) Geology map of the Baie Verte Peninsula (modified after Skulski et al., 2010).

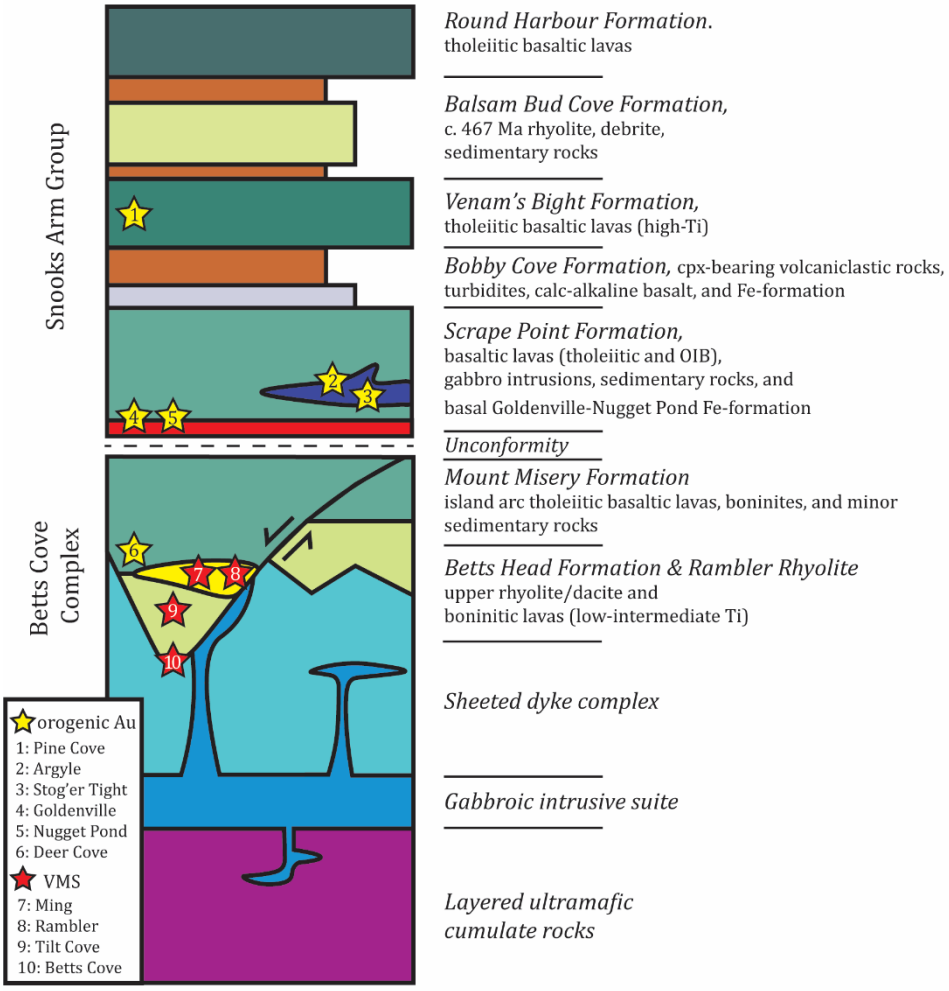

Figure 2.2. Stratigraphy of the Point Rousse Complex (modified after Skulski et al., 2009).

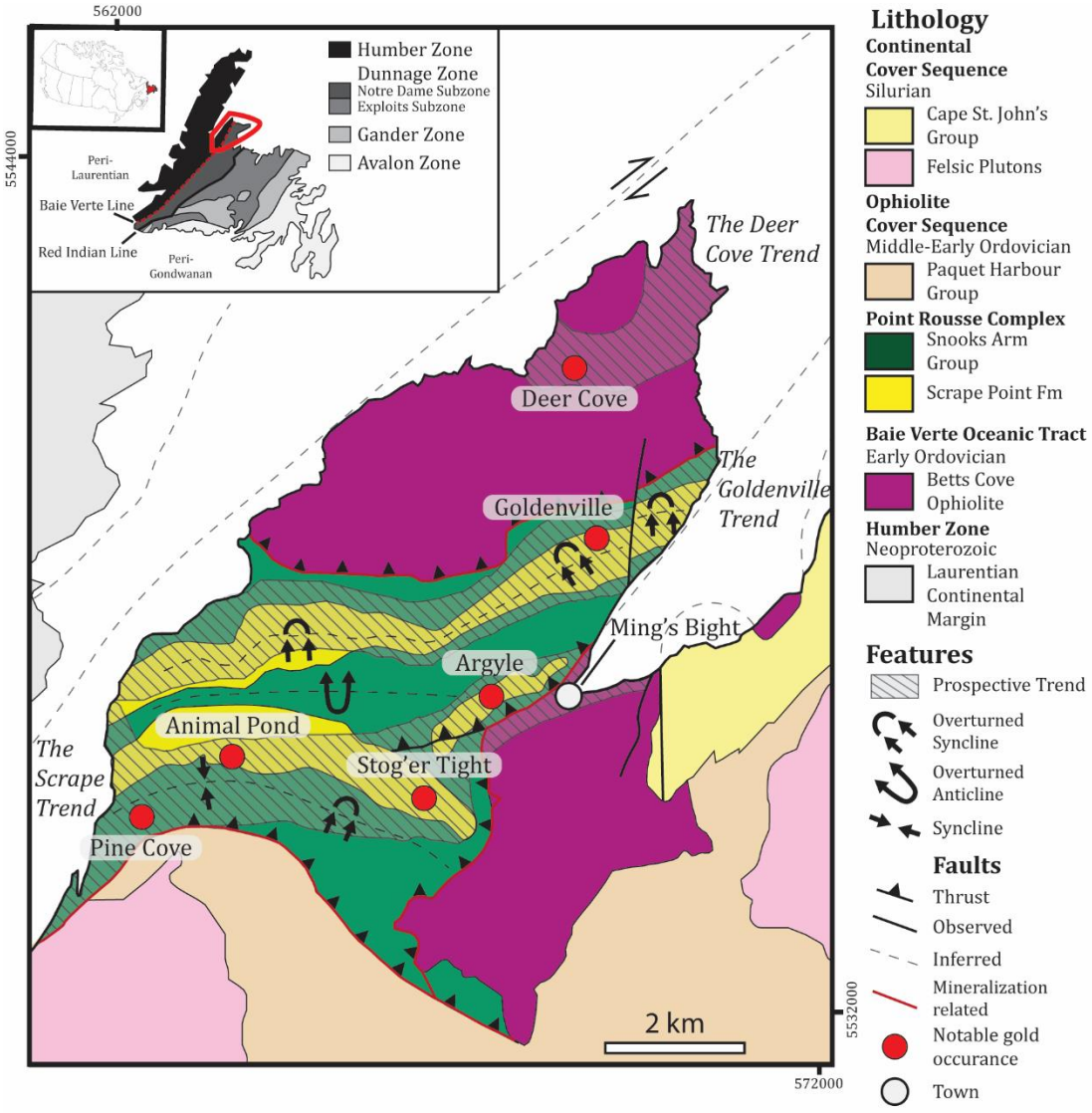

Figure 2.3. Geological map of the Point Rousse Peninsula showing the various deposits (modified after Skulski et al., 2010 and Pawlukiewicz, 2019).

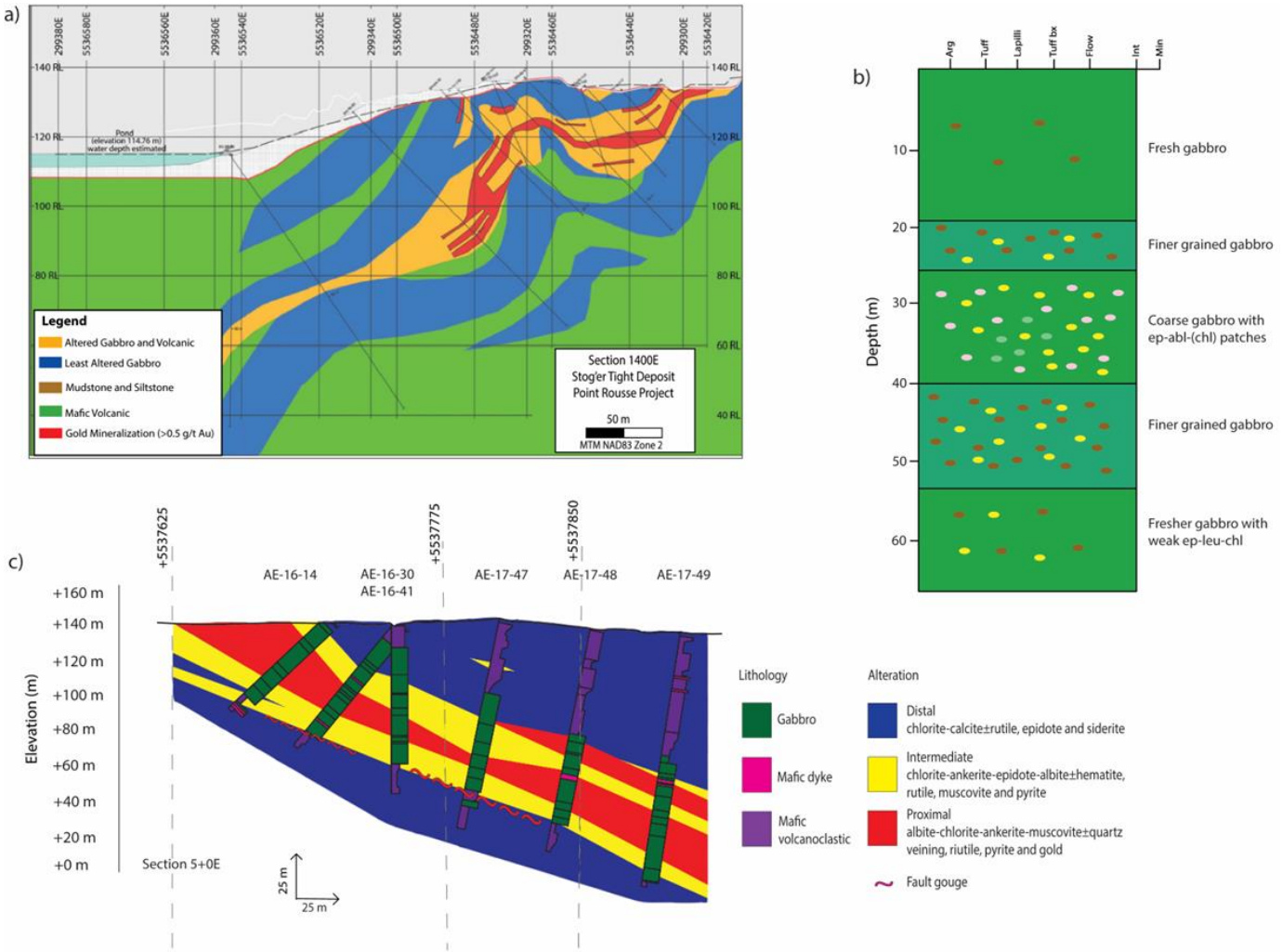

Figure 2.4. a-c) Cross sections through Stog'er Tight and Argyle deposits and b) stratigraphic section from Animal Pond showing gabbro-hosted mineralization.

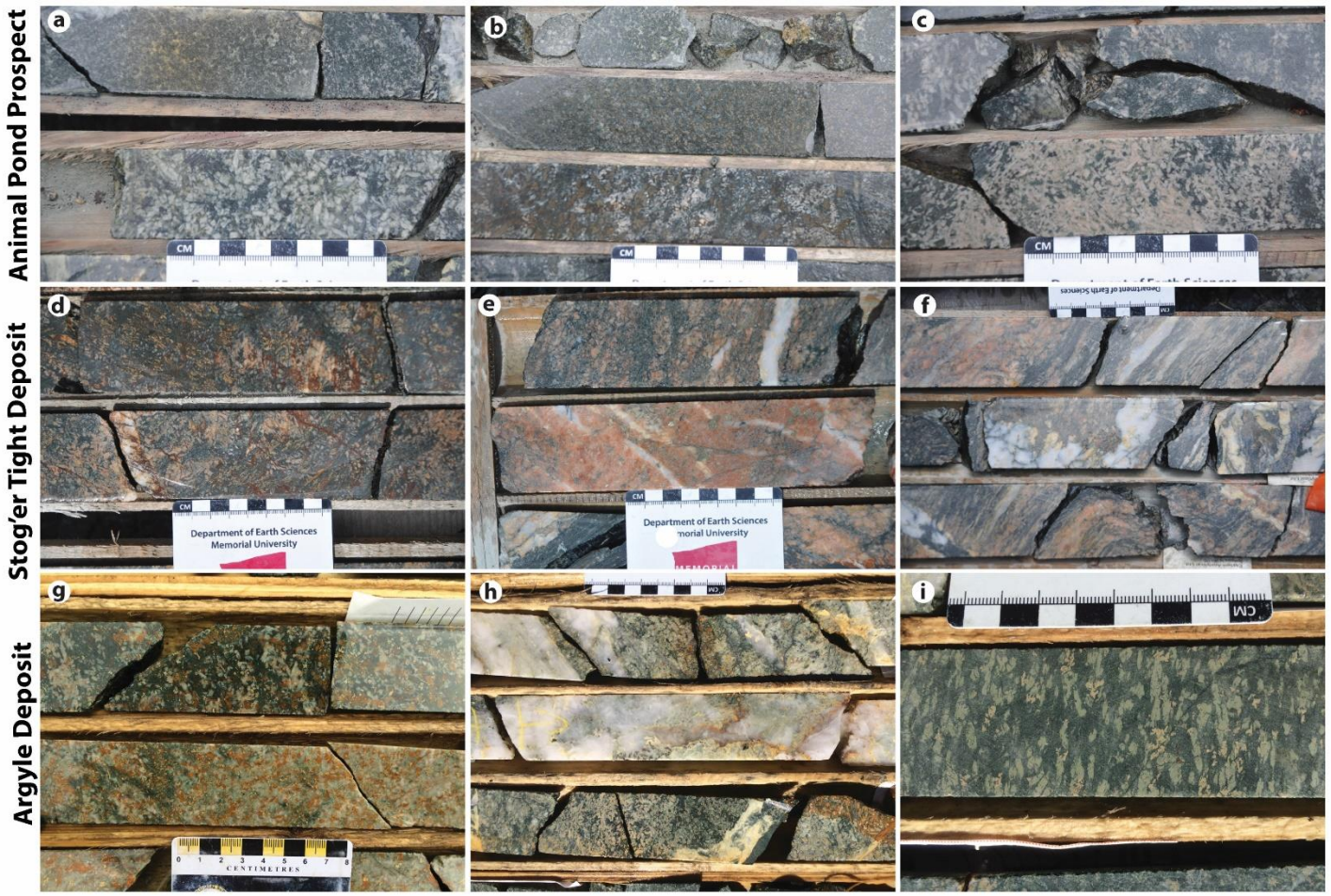

Figure 2.5. Photographs of samples of various gabbros from the Animal Pond prospect, Stog'er Tight and Argyle deposits: a) pegmatoidal plagioclase-rich gabbro with relict cumulate textures and weak albite alteration; b) medium-grained gabbro with minor brown, leucoxene alteration; c) medium- to coarse-grained gabbro with pinkish albite alteration of feldspar with minor chlorite-epidote in the matrix; d) medium grained albite-chlorite-hematite altered gabbro; e) brick red albite-chlorite-Fe-carbonate-hematite altered gabbro with quartz veins and "sooty" pyrite grains that contain gold. This type

of sample is typical of high grade mineralization in Stog'er Tight; f) foliated albite-hematite-chlorite altered gabbro with quartz veins that are cross cutting the foliation as well as those that are parallel to the foliation; g) medium-grained gabbro with chlorite, albite, and hematite alteration; h) albite-chlorite-carbonate altered gabbro with cross-cutting quartz veins; and i) gabbro with feldspars partly altered to albite and beige coloured leucoxene (titanite-rutile intergrown?).

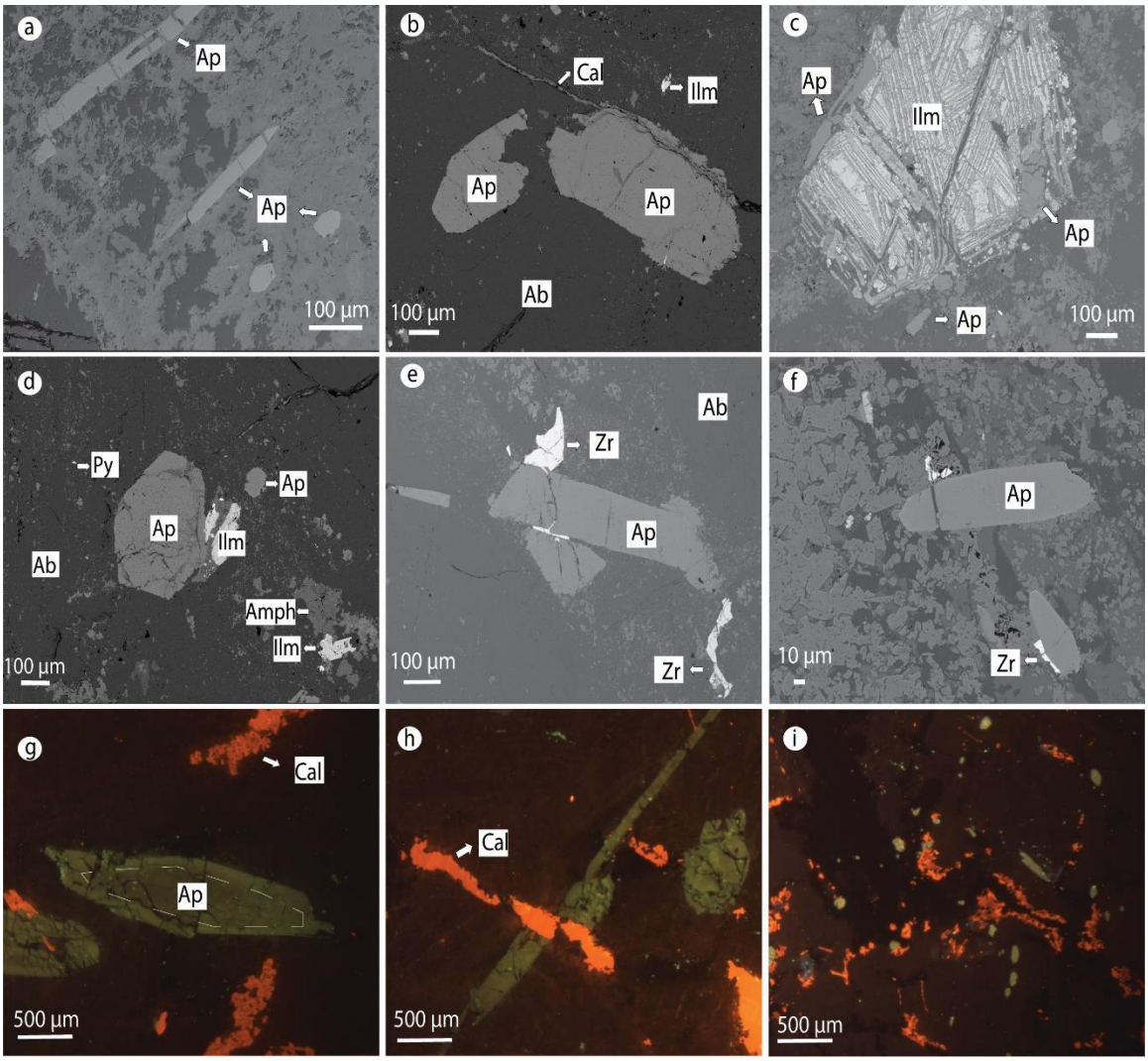

Figure 2.6. Representative back-scattered electron and cathodoluminescence photomicrographs illustrating the key petrographic features of the magmatic apatite; a) needle-shaped or fine-grained apatite intergrown with albite in Argyle deposit; b) apatite grain from the Animal Pond prospect showing no internal texture; c) apatite occurring as an inclusion within titanomagnetite with exsolved ilmenite ; d) apatite coexisting with ilmenite displaying a euhedral crystal shape and has a bright reflection in the Animal Pond prospect; e-f) apatite coexisting with zircon in the Animal Pond prospect; g) apatite showing distinct dark core-light rim zonation from the Animal Pond prospect; h-i) euhedral to subhedral apatite grains showing yellow and yellow-green luminescence in Argyle deposit. Abbreviations: Ab= Albite, Amph= Amphibole, Ap = Apatite, Cal=Calcite, Ilm= Ilmenite, Py = Pyrite, Zr = Zircon.

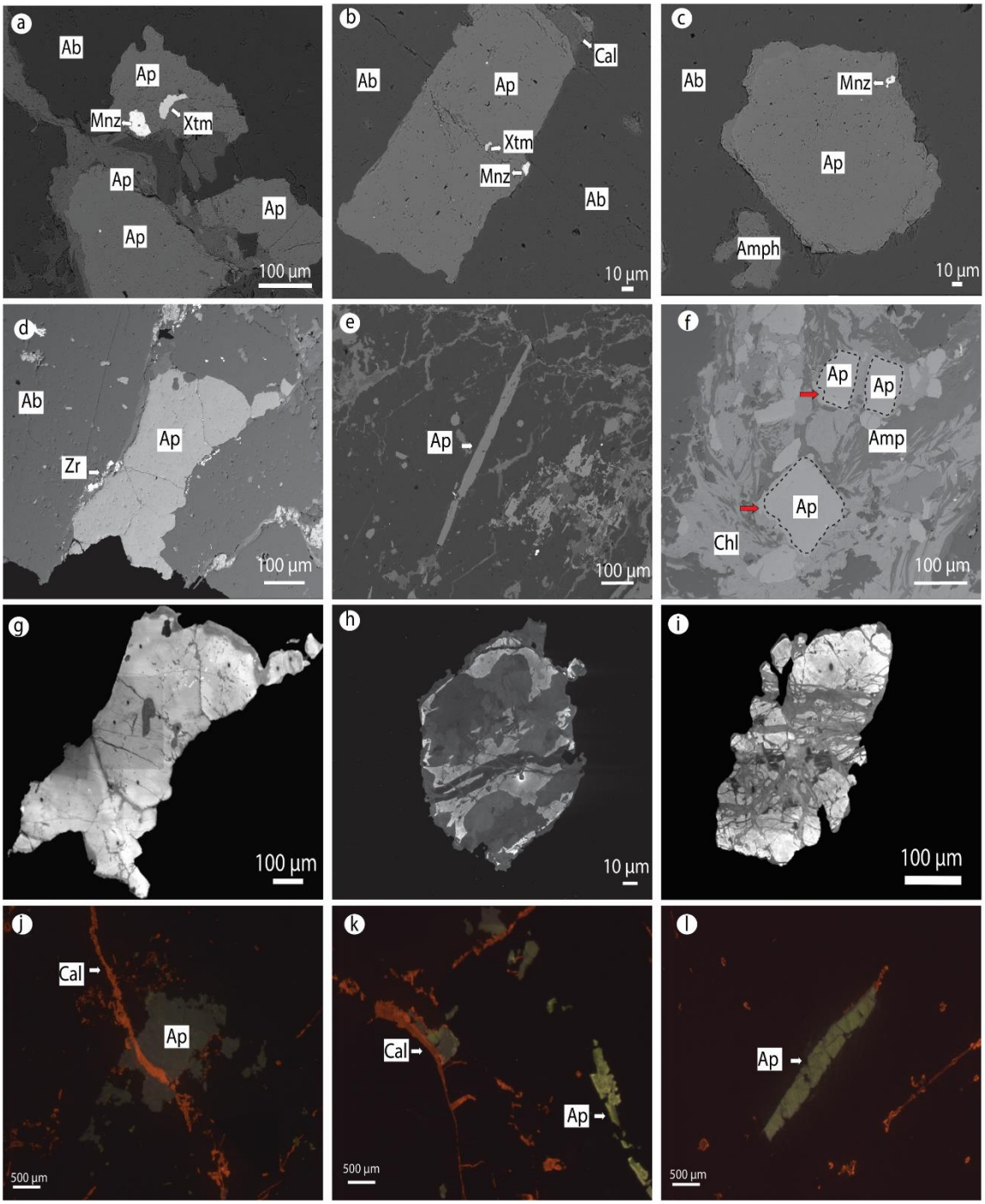

Figure 2.7. Representative back-scattered electron and cathodoluminescence photomicrographs illustrating the key petrographic features of the hydrothermally influenced apatite: a-d) hydrothermally influenced apatite coexisting with secondary hydrothermal minerals, including monazite, xenotime, and zircon in Stog'er Tight deposit; e) acicular apatite in Argyle deposit; f) apatite grains showing dark rims and bright cores in the early stages of alteration in Stog'er Tight deposit; g-i) apatite grains displaying complex CL features with heterogeneous patchy pattern from Stog'er Tight and Argyle deposits; j-l) apatite grains

showing distinct dark green to gray luminescence from Stog'er and Argyle deposits. Abbreviations: Ab= Albite, Amph= Amphibole, Ap = Apatite, Cal=Calcite, Chl= Chlorite, Mnz= Monazite, Xtm= Xenotime, Zr = Zircon.

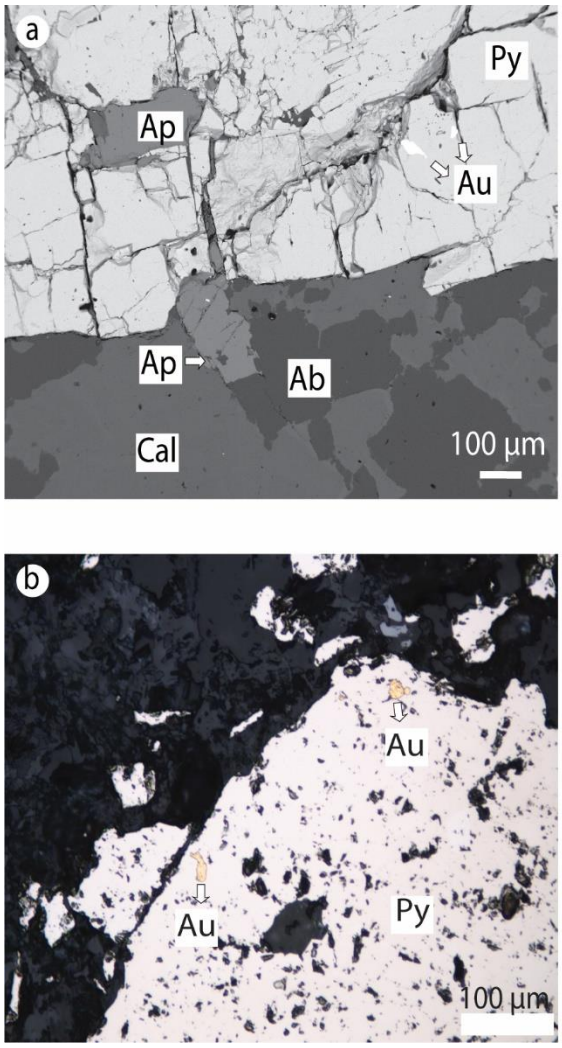

Figure 2.8. Photomicrographs of apatite associated with orogenic gold within pyrite: a) backscatter image of the hydrothermally inflenced apatite grain with gold inclusions within pyrite crystal in the most altered zones from Stog'er Tight deposit; and b) gold infilling voids and fractures within pyrite from Argyle deposit. Abbreviations: Ap = apatite, Py= pyrite, Au=gold, Ab=albite, Cal=calcite.

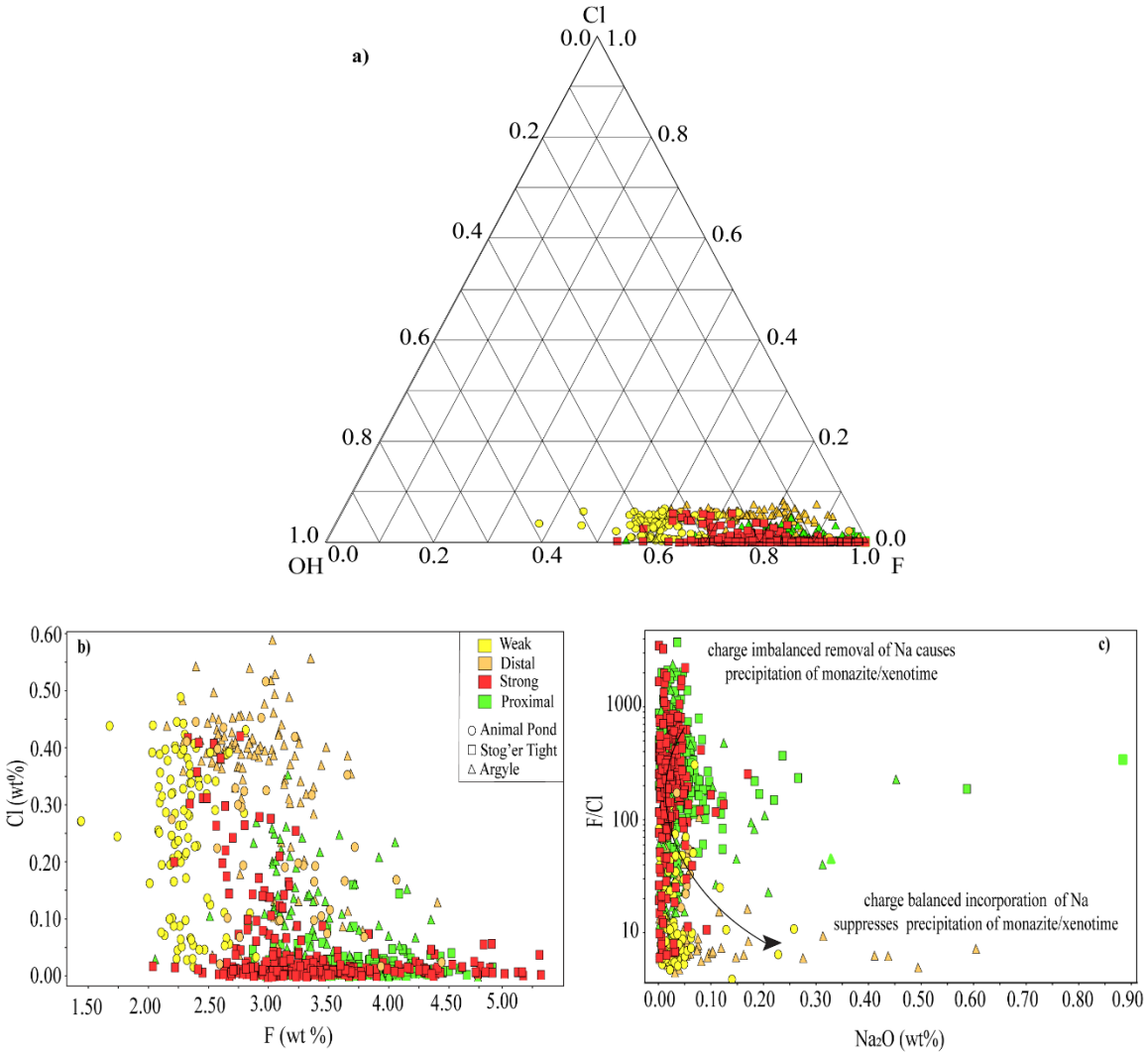

Figure 2.9. Diagrams illustrating the halogen and Na_2O contents of apatite from the Animal Pond prospect, Stog'er Tight and Argyle deposits. a) Ternary OH-Cl-F plot (using Approach 3 of Ketcham, 2015); b) Cl versus F plot; c) F/Cl ratio and Na_2O contents.

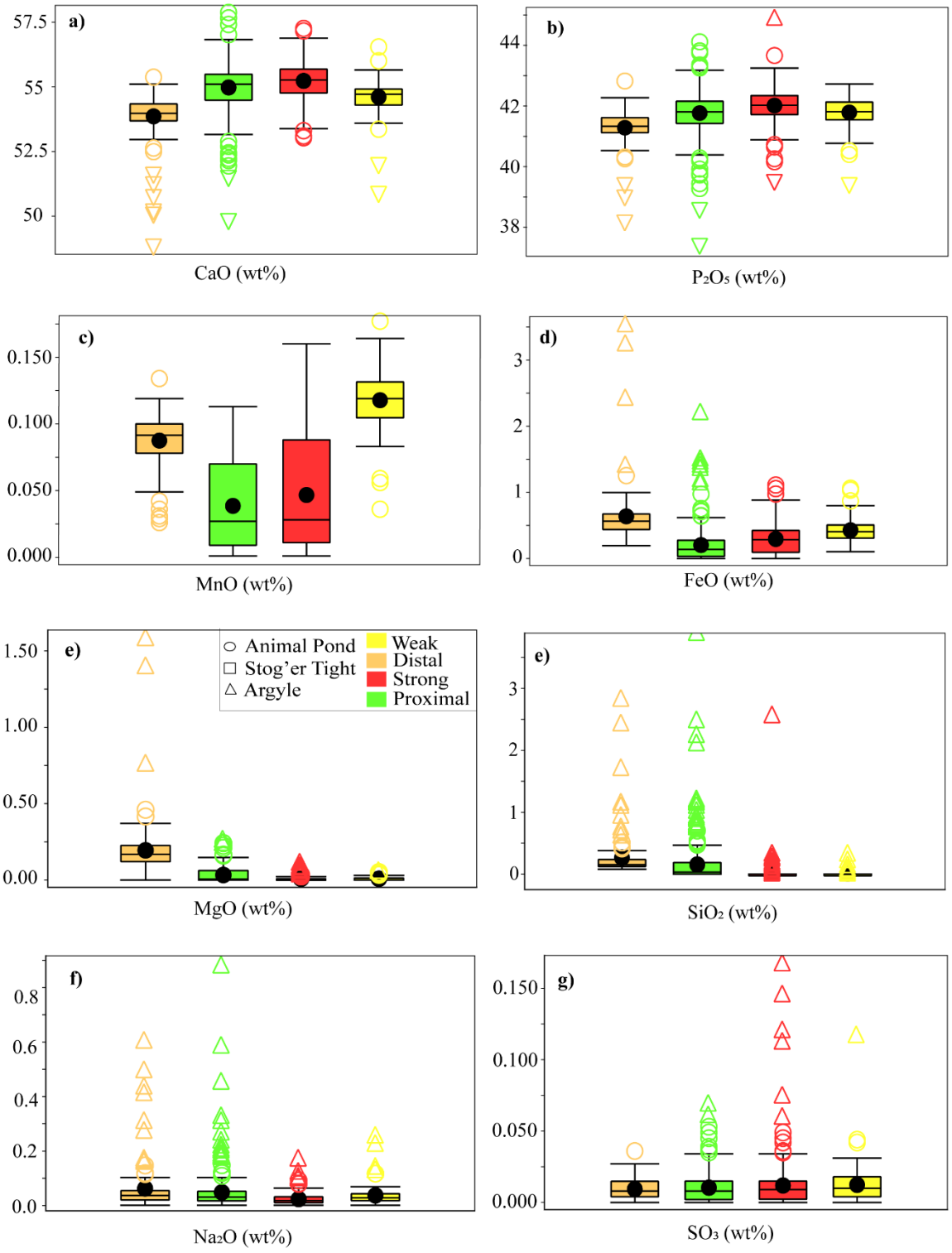

Figure 2.10. Box-and-whisker plots showing the major element contents of fluorapatite from the Animal Pond prospect, Stog'er Tight and Argyle deposits (based on EPMA analysis). Line =median value; square = mean value; box = interquartile range; triangle= a far outlier; circle= an outlier.

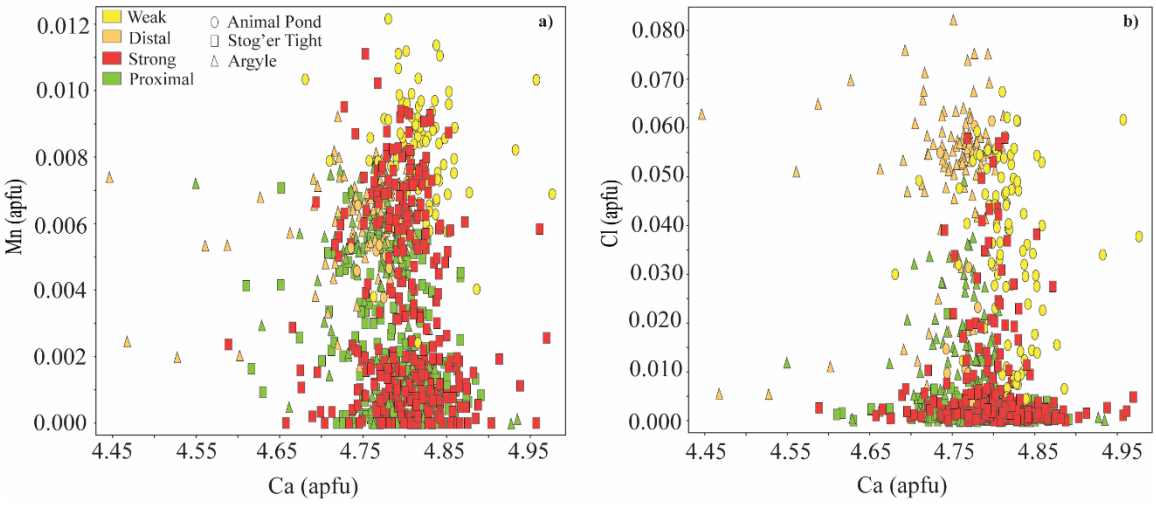

Figure 2.11. Trace element composition of apatite in unaltered and altered host rocks, showing that altered samples are typically depleted in Mn and Cl (apfu = atomic per formula unit).

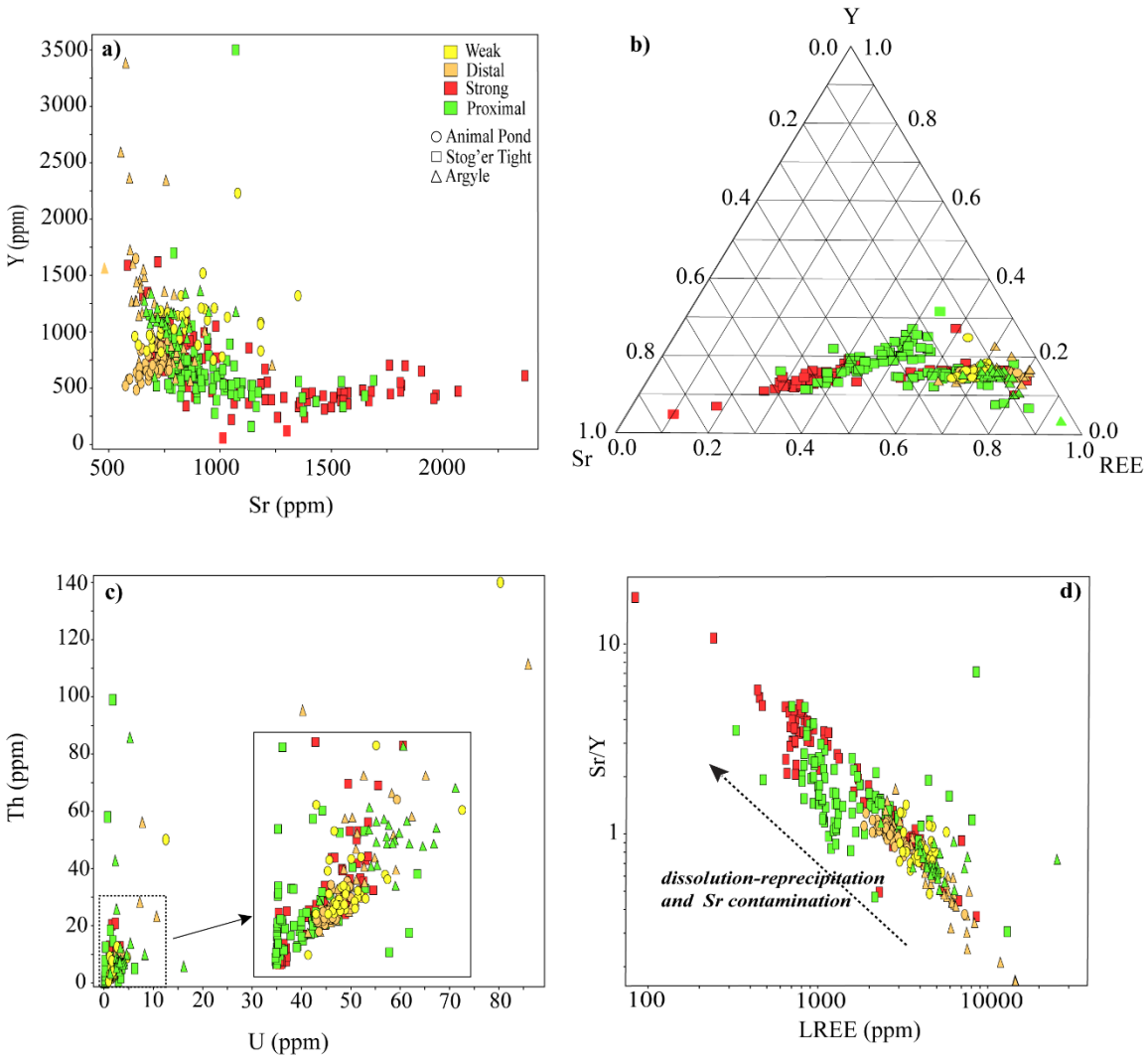

Figure 2.12. Diagrams displaying trace-element variations of fluorapatite from the Animal Pond prospect, Stog'er Tight and Argyle deposits: a) Y (ppm) versus Sr (ppm); b) ternary Sr-Y-REE plot; c) Th (ppm) versus U (ppm); and d) Sr/Y versus LREE (La + Ce + Pr + Nd) (ppm).

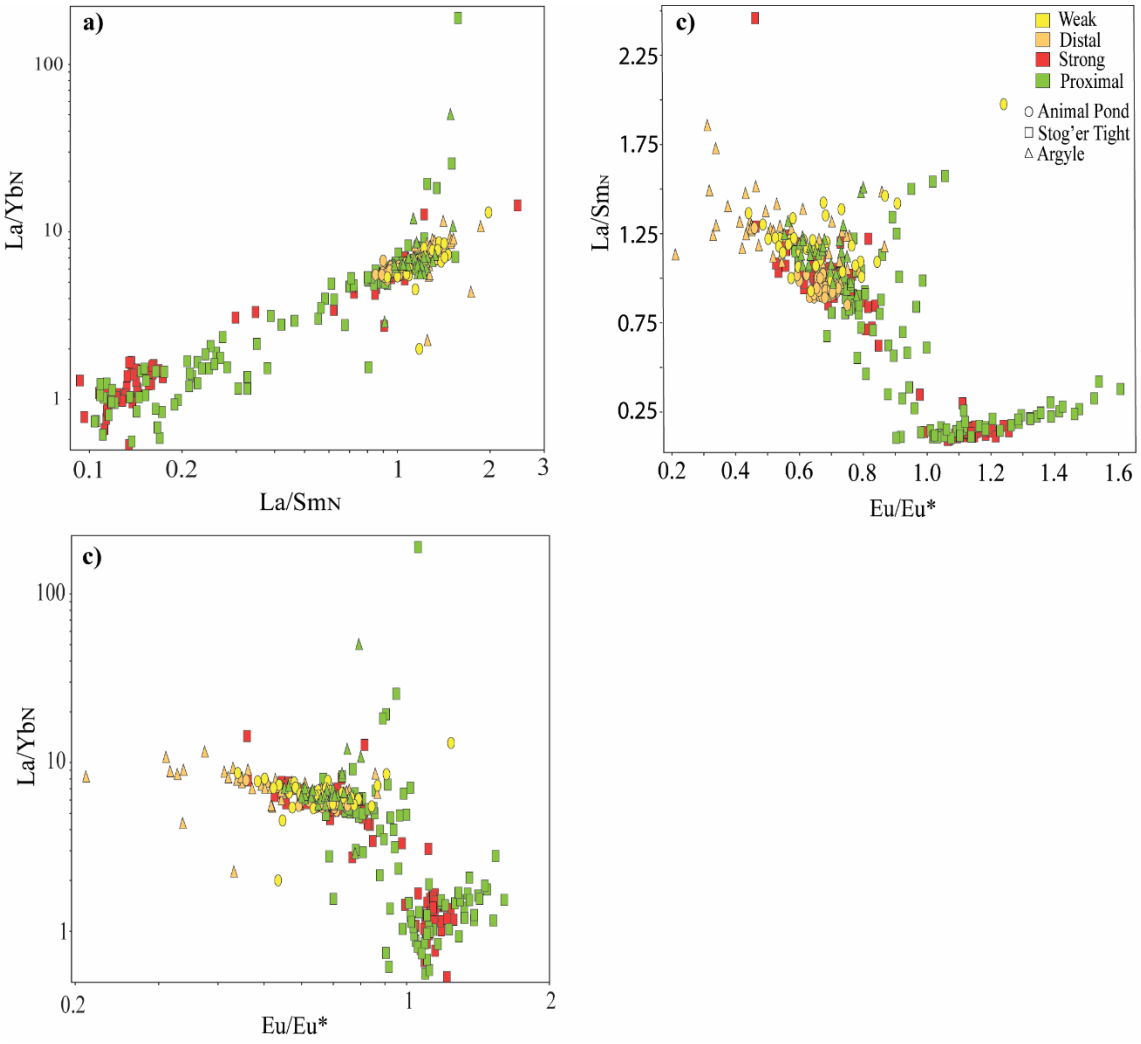

Figure 2.13. Binary plots of trace element concentrations and ratios of fluorapatite from the Animal Pond prospect, Stog'er Tight and Argyle deposits, illustrating differences between magmatic and hydrothermal apatite. a) La/Yb_N versus La/Sm_N; b) La/Sm_N versus Eu/Eu*; c) La/Yb_N versus Eu/Eu*. Normalizing (N) values taken from Taylor and Mclennan (1985).

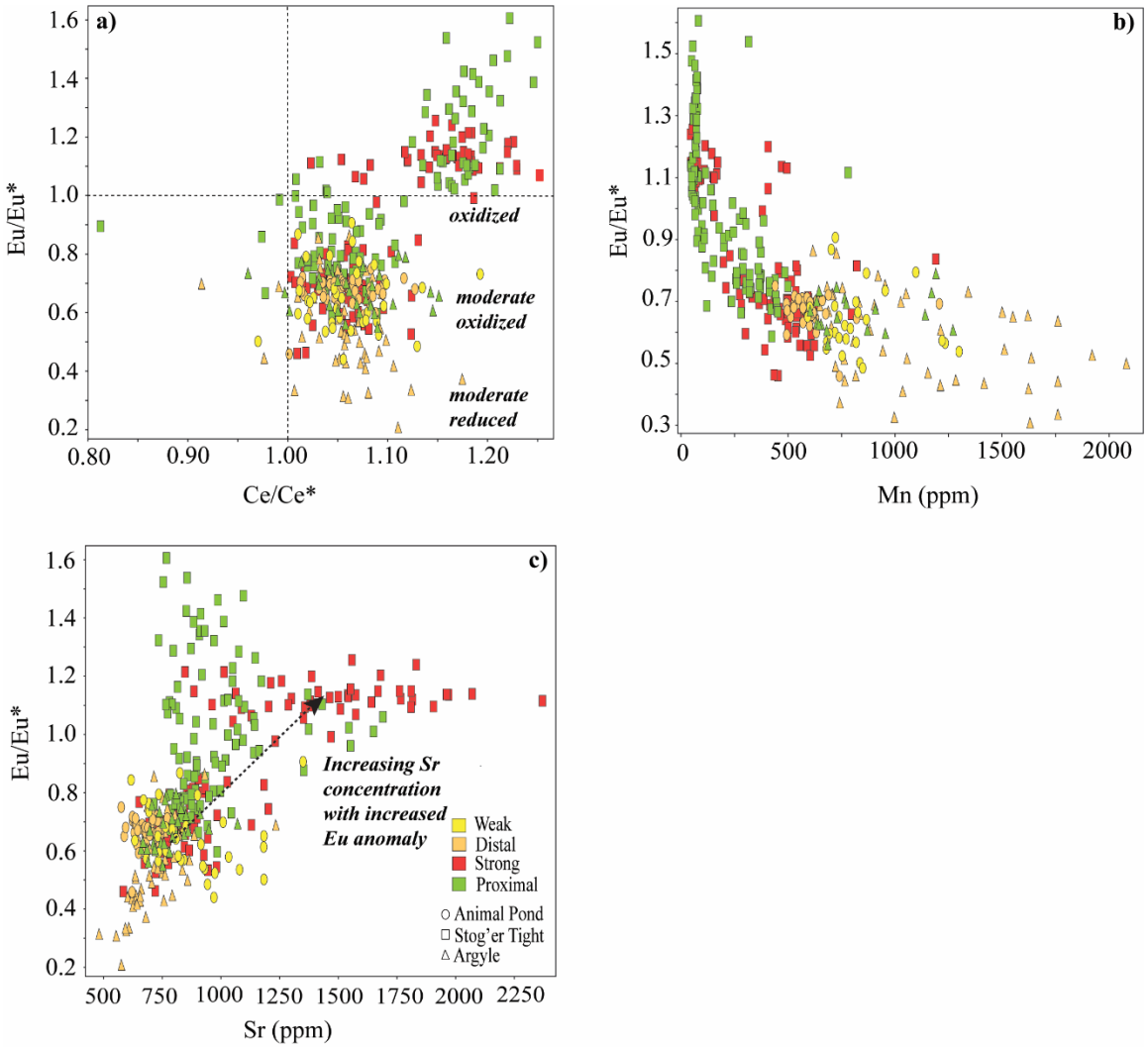

Figure 2.14. a) Eu/Eu* versus Ce/Ce* in fluoroapatite (Mercer et al., 2020); b-c) Eu/Eu* versus Mn, and Sr contents in the fluorapatite; Eu/Eu* = $(Eu)_{CN}/[(Sm)_{CN} \times (Gd)_{CN}]^{0.5}$; Ce/Ce* = $Ce_{CN}/[(La_{CN} \times Nd_{CN})]^{0.5}$. CN – chondrite normalized. Normalization values are from Taylor and Mclennan (1985).

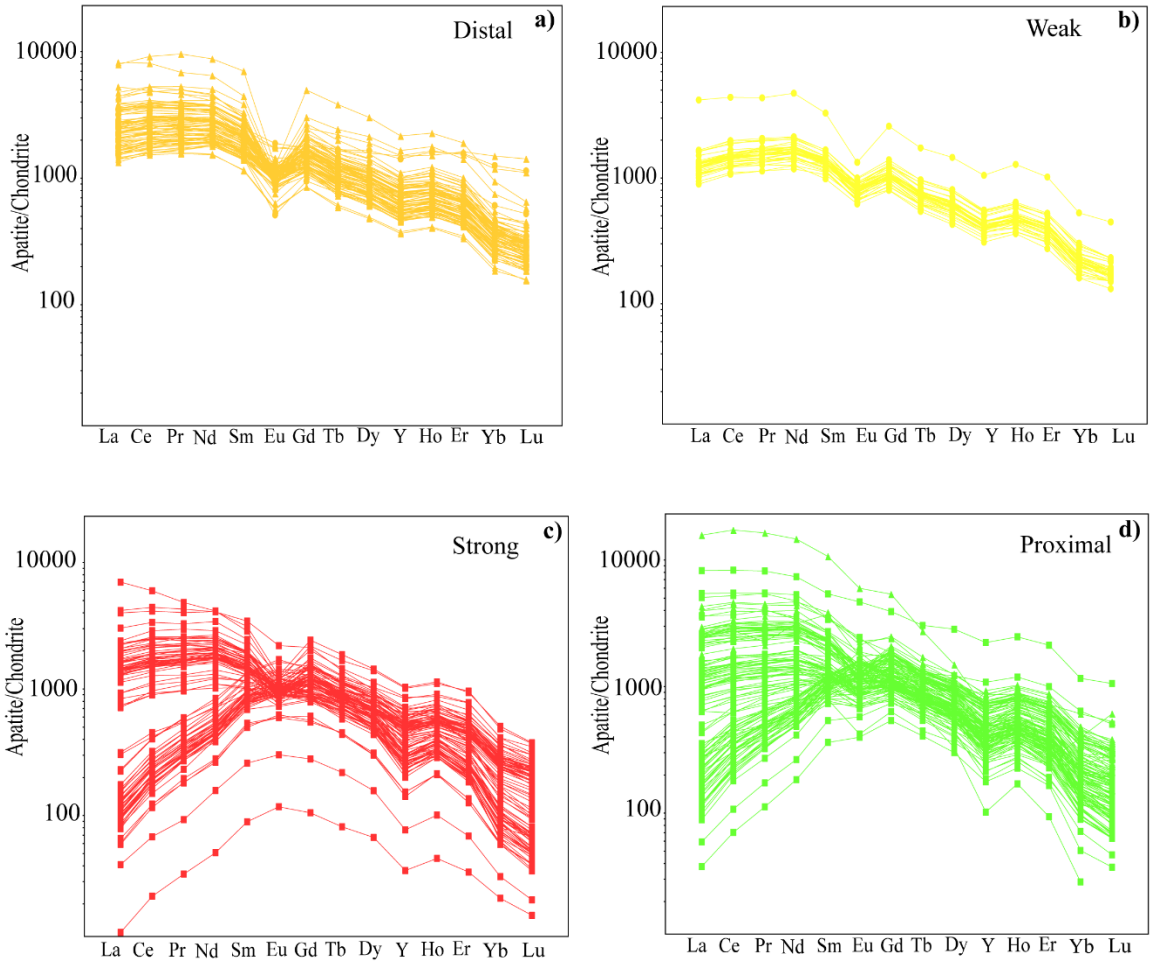

Figure 2.15. Chondrite-normalized REE and Y diagrams in fluorapatite (chondrite values from McDonough and Sun, 1995).

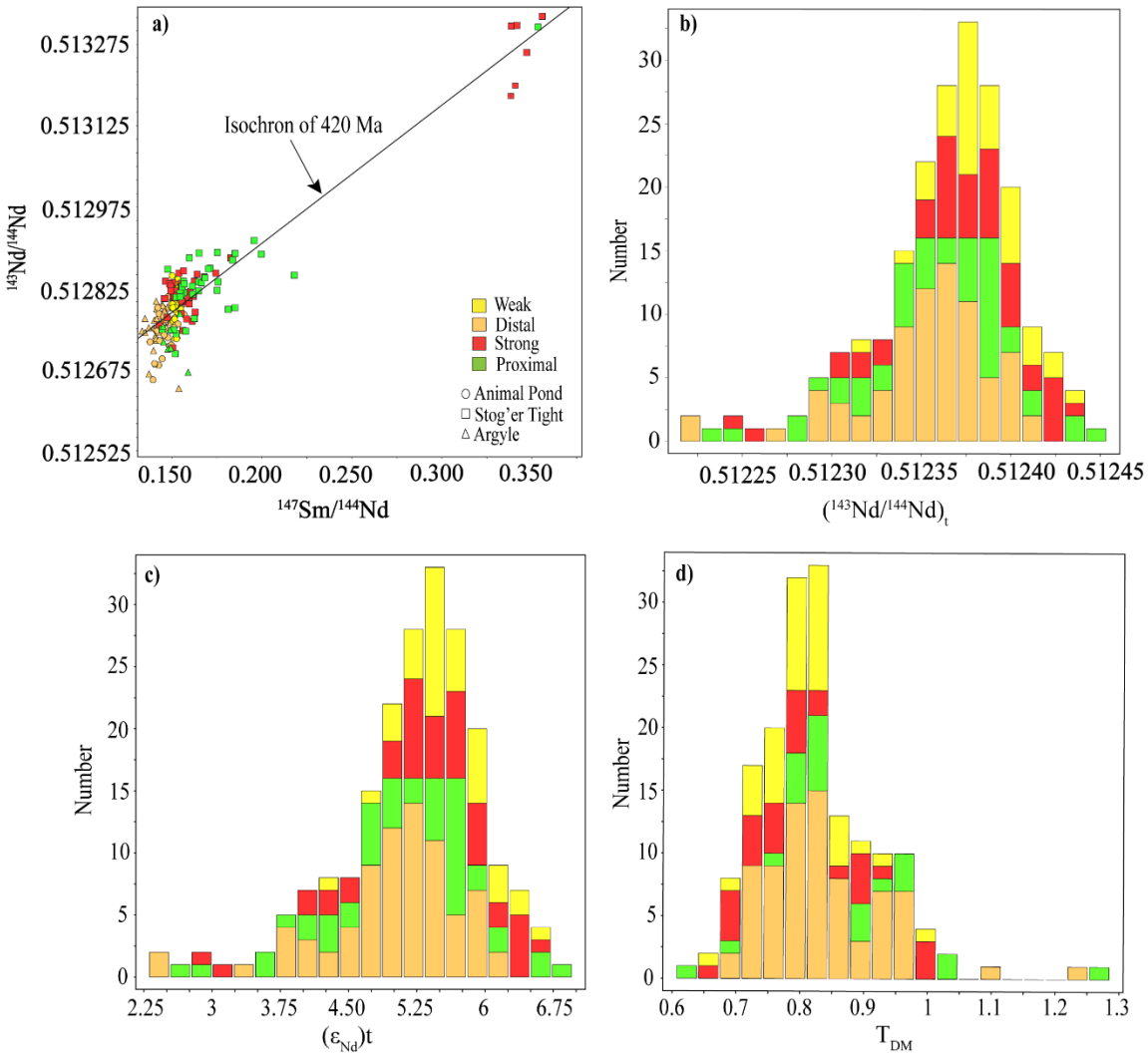

Figure 2.16. a) Plot of $^{143}Nd/^{144}Nd$ versus $^{147}Sm/^{144}Nd$ for fluorapatite. A 420 Ma Sm-Nd isochron is shown for reference; b) Histogram of $(^{143}Nd/^{144}Nd)_t$ distribution for the fluorapatite; c) Histogram of $(\varepsilon_{Nd})t$ (420 Ma) distribution for the fluorapatite; d) Histogram of T_{DM} distribution for the fluorapatite.

Chapter 3: Summary and Future Work

3.1. Summary

This thesis has documented the combination of mineral textures, major-, minor-, and trace element chemistry, and Nd isotope geochemistry of representative apatite from several gabbro hosted orogenic gold deposits, including the Stog'er Tight and Argyle deposits and Animal Pond prospect on the Baie Verte Peninsula, Newfoundland, Canada. Apatite from these deposits record both magmatic and hydrothermal stages of mineralization associated with fluid-aided and coupled dissolution-precipitation processes. The results contribute to a better understanding of the evolution of orogenic gold systems on the Baie Verte Peninsula and elsewhere in the Appalachian-Caledonide orogen.

The following conclusions are drawn from this study:

(1) Cathodoluminescence reveals significant differences between magmatic and hydrothermally influenced apatite in the Baie Verte Peninsula. Apatites in fresh rocks show homogeneous textures and distinct luminescence (yellow-to-yellow green), whereas apatite in altered rocks shows complex textures with heterogeneous patchy patterns and dark green to gray luminescence. Apatite texture observations from the Animal Pond prospect, Stog'er and Argyle deposits suggest the modification of primary (magmatic) apatites by interaction with hydrothermal fluids.

(2) Apatite chemistry, as determined by electron microprobe and laser ablation inductively coupled plasma mass spectrometry, is also distinct for these two

cathodoluminescence end-members. Hydrothermally influenced apatite generally has LREE-, Cl- and Mn-depletion, elevated Sr and Sr/Y ratios, and higher Eu/Eu* values, and MREE-rich, convex chondrite normalized REE patterns, compared to igneous apatite, which have LREE-rich signatures and distinctive chondrite-normalized REE patterns. These features are interpreted to be the product of orogenic Au-bearing fluid-rock interaction and the destruction and subsequent redistribution of elements from primary igneous phases into secondary hydrothermal phosphates, including residual apatite, monazite, and xenotime.

(3) The deposition of gold occurred concurrently with the dissolution and reprecipitation of apatite, which caused the leaching of REE from apatite and the precipitation of coeval hydrothermal monazite and xenotime.

(4) Both igneous and hydrothermally altered apatite have similar initial Nd isotope compositions. Isotopic data indicates that the gabbroic magmas were derived from juvenile sources and that Nd isotopic compositions were not changed during hydrothermal alteration. Compared to $\varepsilon_{Nd}(t)$ of the depleted mantle reservoir at 420 Ma, the results are lower than the DM and implies involvement of Nd into the apatites from a reservoir with a history of LREE-enrichment. T_{DM} ages are consistent with the ages of basement domains within the Baie Verte Peninsula and the peri-Laurentian realm and are consistent with at least some Nd having been derived from basement domains during orogenic Au bearing apatite formation either via mantle-derived magmatism or from orogenic Au-related hydrothermal fluids.

(5) This study shows that textural features, revealed by CL and BSE imaging, halogen concentrations, trace element and isotopic compositions of apatite can be used to unravel the ore forming processes as well as the genesis of orogenic gold deposits.

3.2. Suggestions for Future Research

As in every project, additional work is still required to understand the ore-forming processes and to better define exploration vectors for orogenic Au on the Baie Verte Peninsula. Recommended areas for future work include:

(1) LA-ICPMS U/Pb geochronology of hydrothermal zircon, apatite, monazite, and xenotime from new larger samples to constrain the absolute timing of gold mineralization.

(2) Re-Os of pyrite to constrain the timing of the various stages of mineralization within the gold deposit.

(3) Whole rock tracer radiogenic isotopes (e.g., Sm-Nd, Lu-Hf) of gabbro to get information about possible metal and REE sources.

(4) O isotope compositions of apatite in fresh and altered rocks and in situ S isotope analysis and trace element mapping of representative pyrite grains could provide valuable insight into potential sources of fluids and metals in gold deposits.

APPENDIX A: Representative BSE images of apatites from the Animal Pond Prospect, Stog'er Tight and Argyle deposits

Sample : **195941** (Animal Pond), Alt: Distal

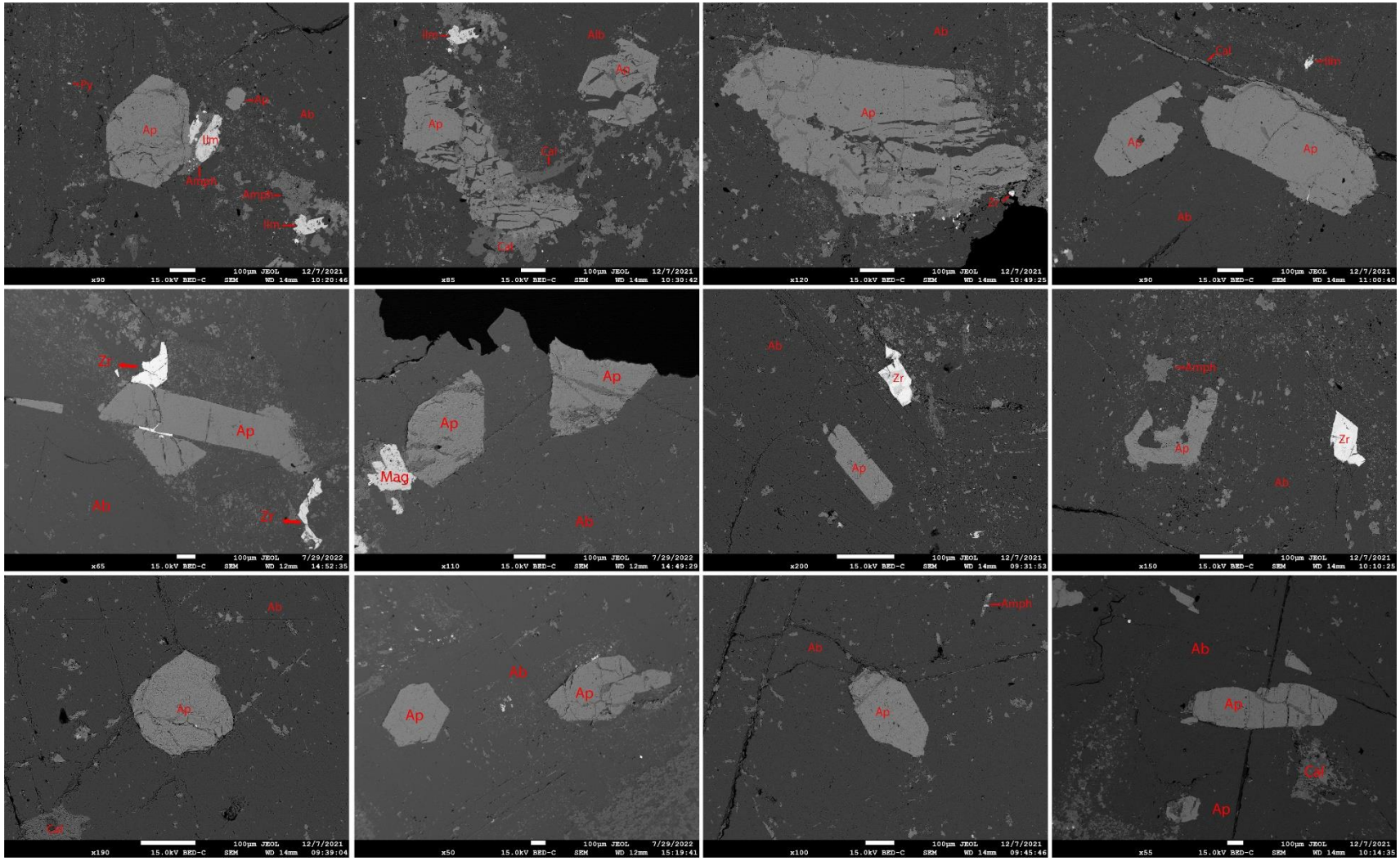

Sample : **195939** (Animal Pond), Alt: Weak

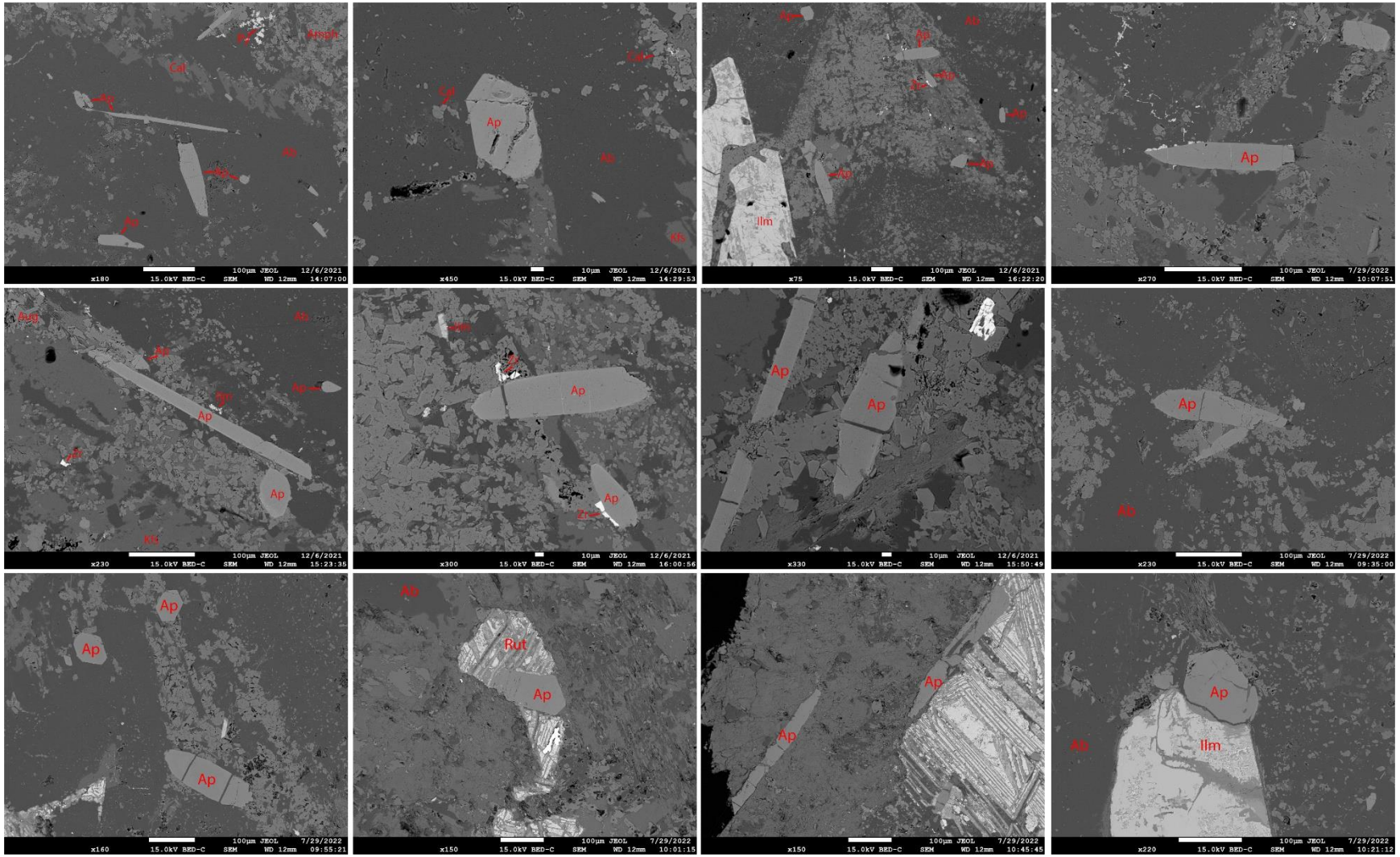

Sample : **195913** (Stog'er Tight), Alt: Strong

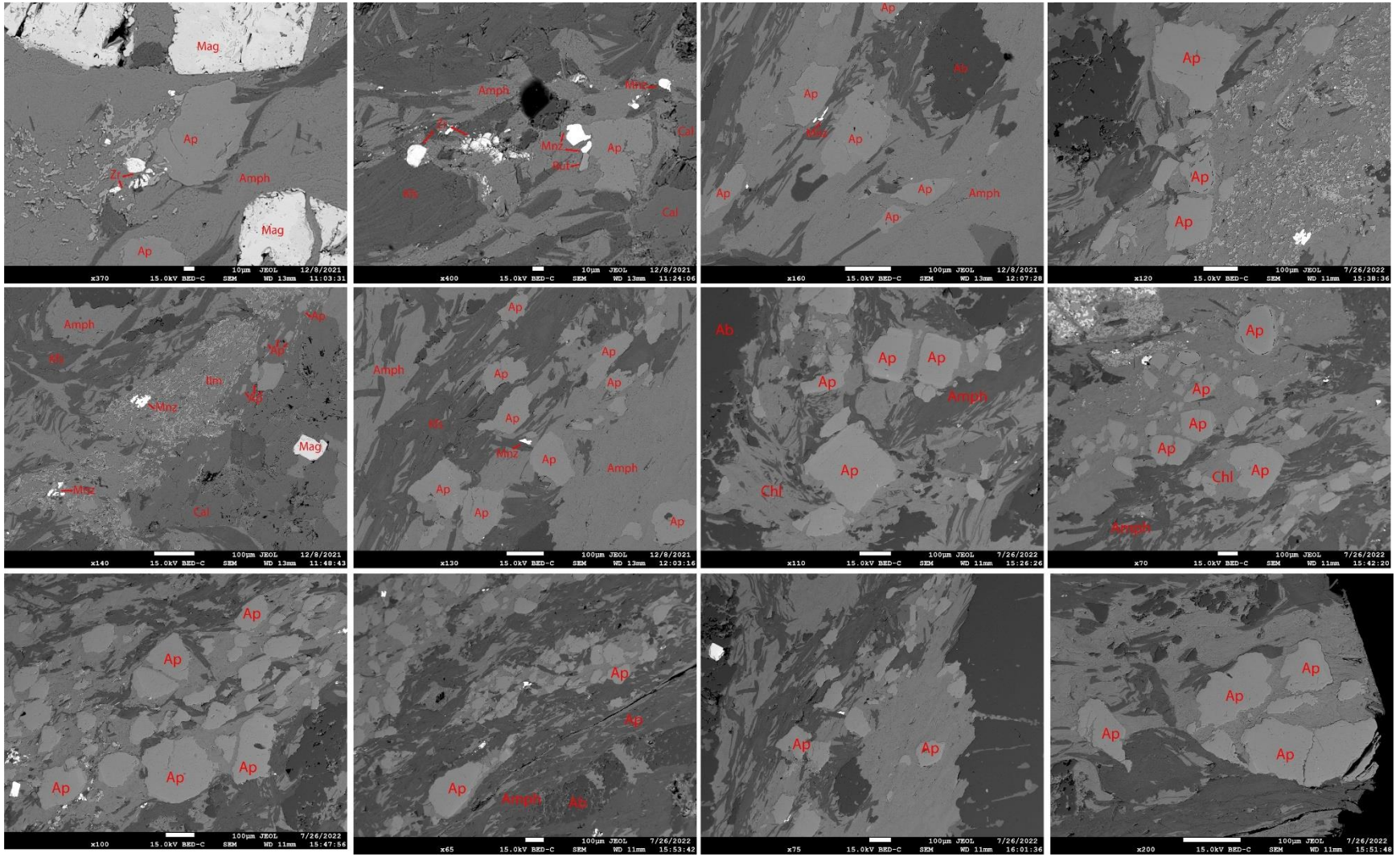

Sample : **195908** (Stog'er Tight), Alt: Strong

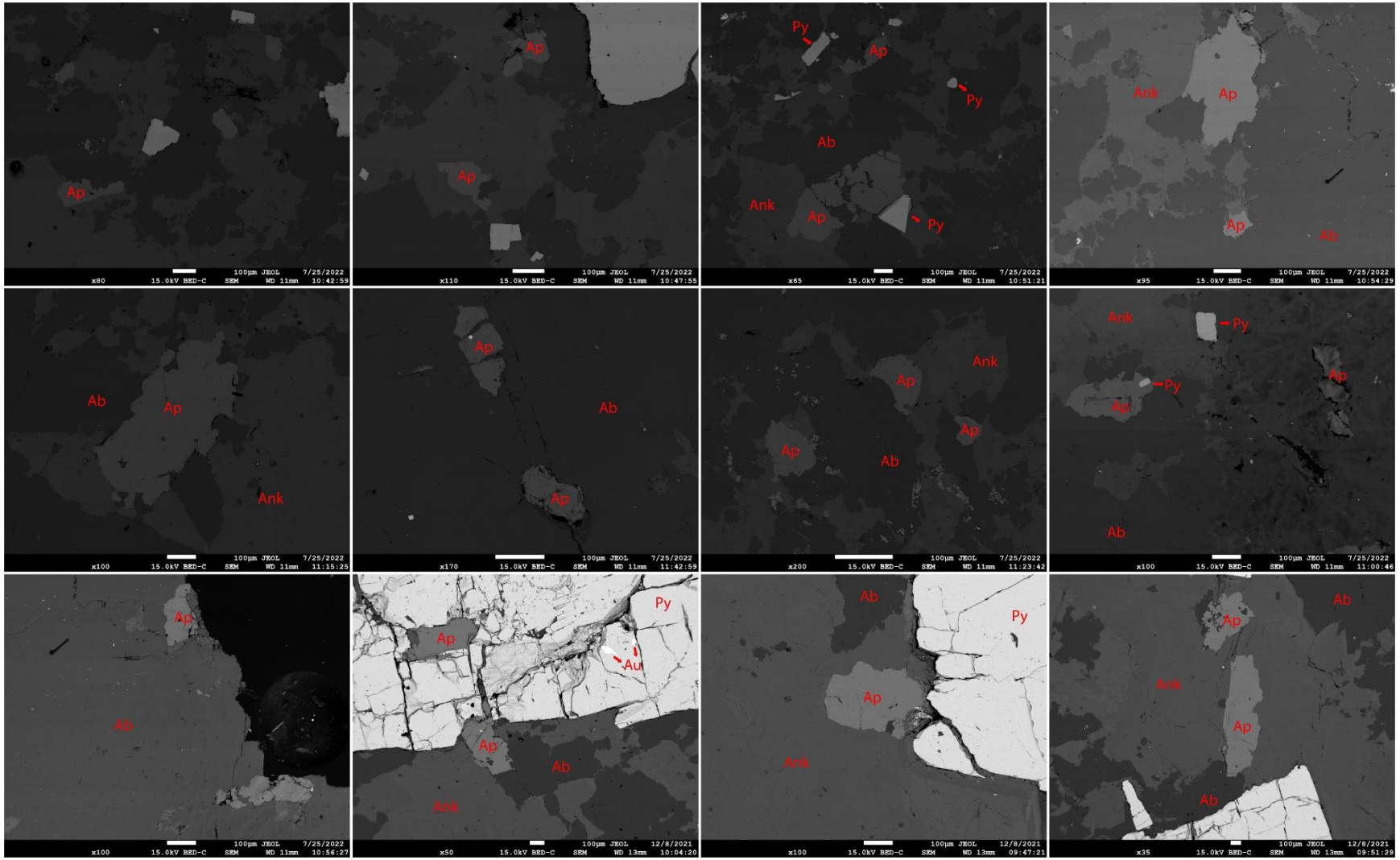

Sample : **16SJP008** (Argyle), Alt: Distal

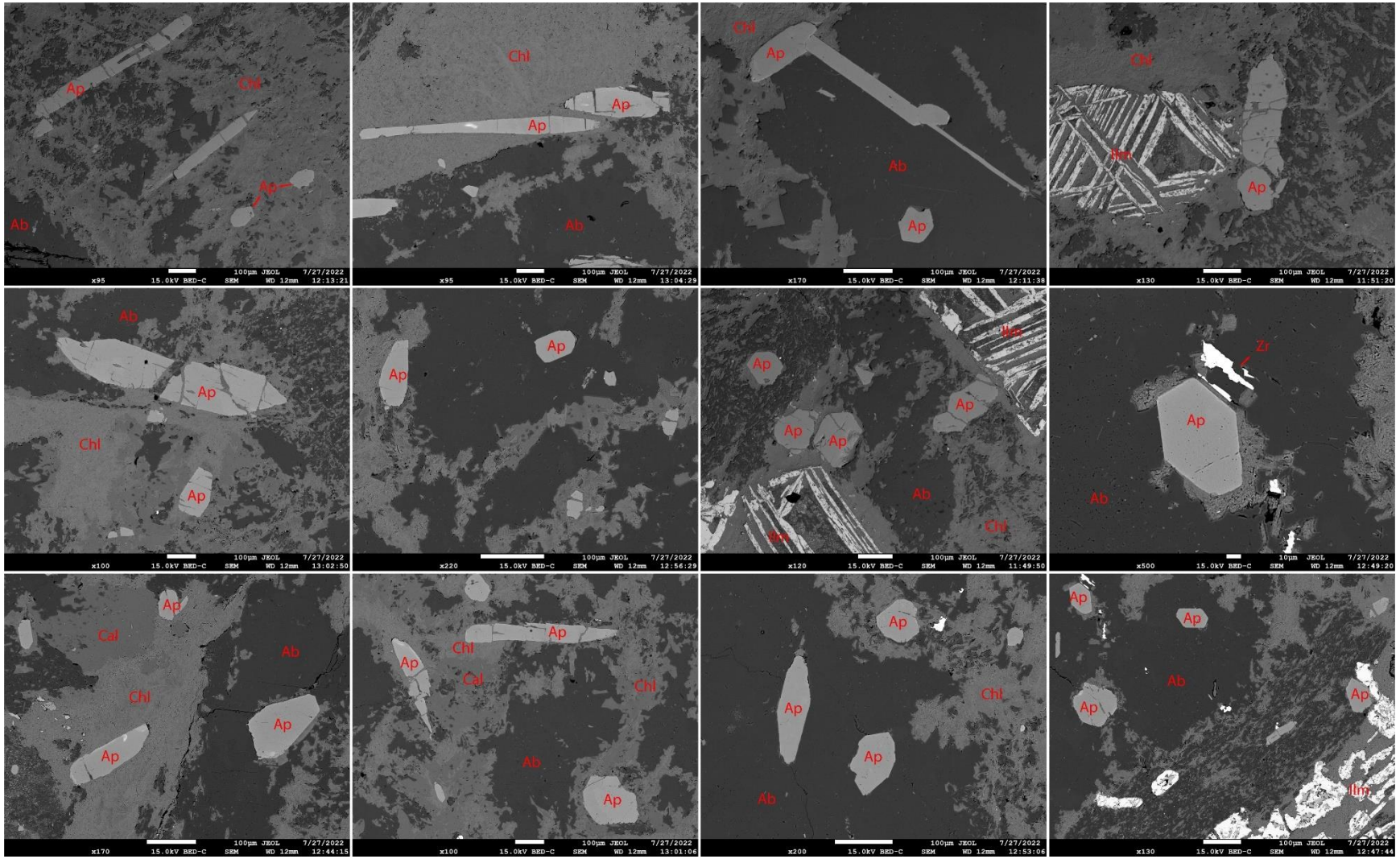

Sample : **16SJP002** (Stog'er Tight), Alt: Proximal

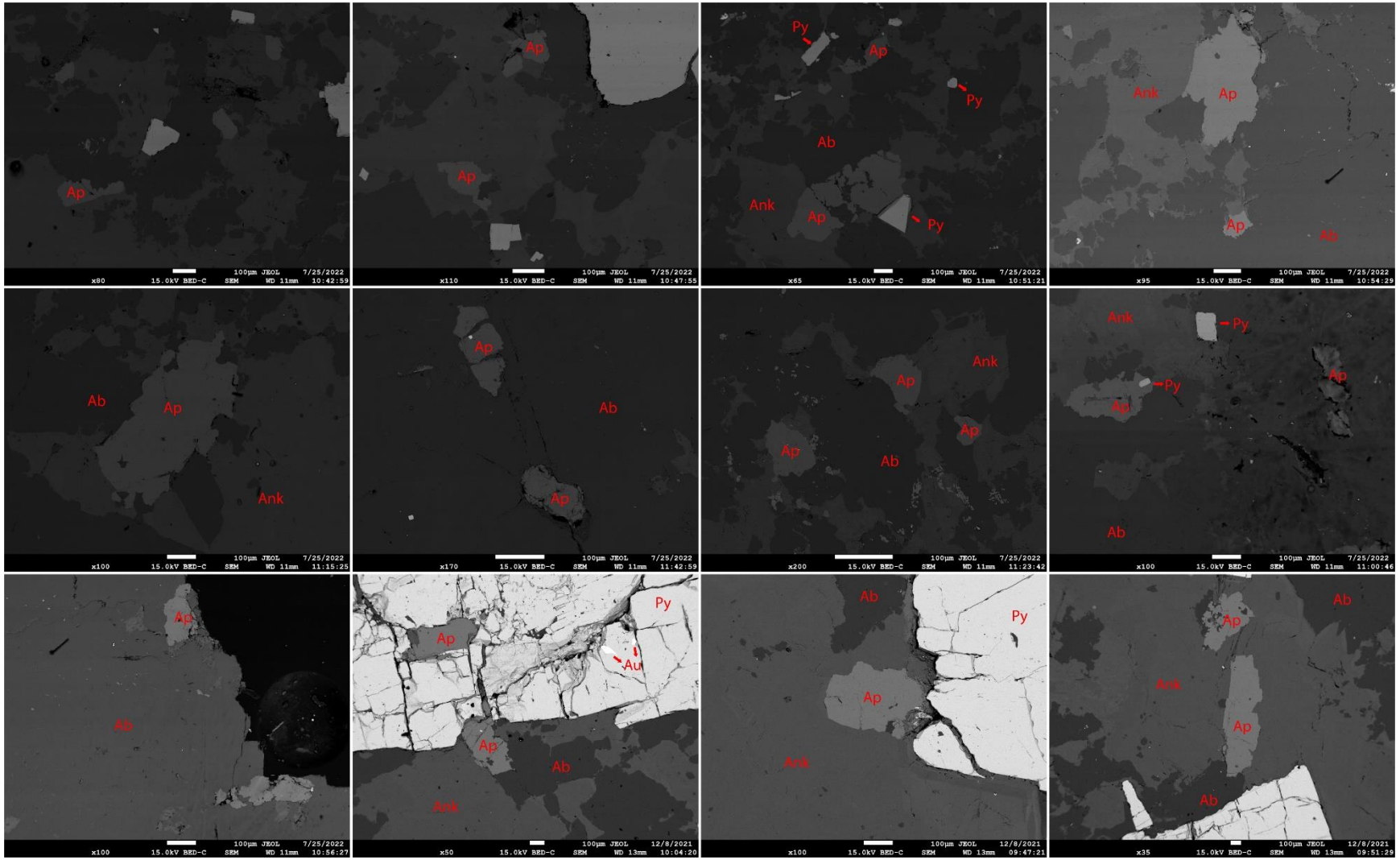

Sample : **16SJP001** (Stog'er Tight), Alt: Proximal

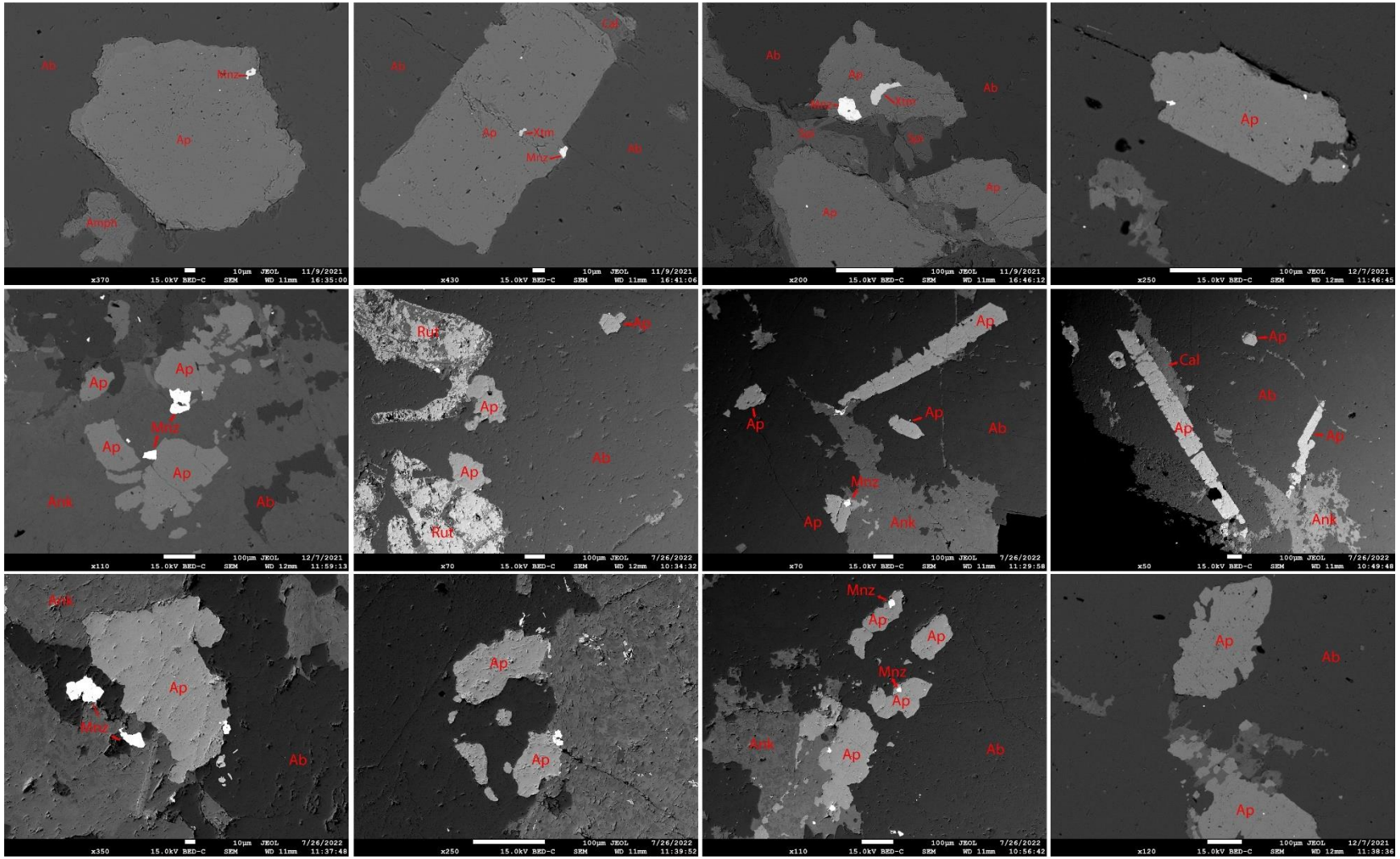

Sample : **I951379** (Argyle), Alt: Proximal

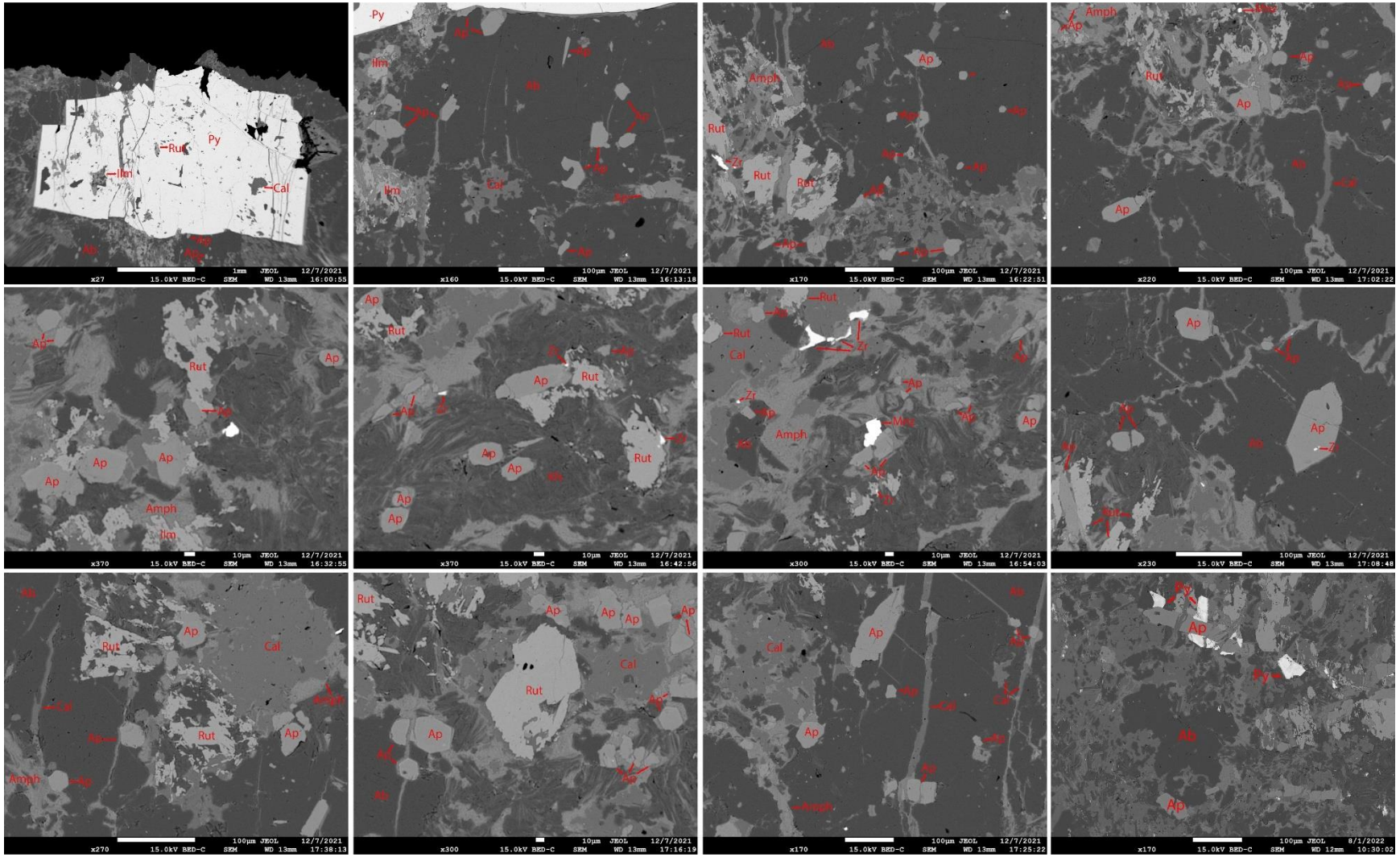

APPENDIX B: Representative CL images of apatites from the Animal Pond Prospect, Stog'er Tight and Argyle deposits

Sample : **195941** (Animal Pond), Alt: Distal

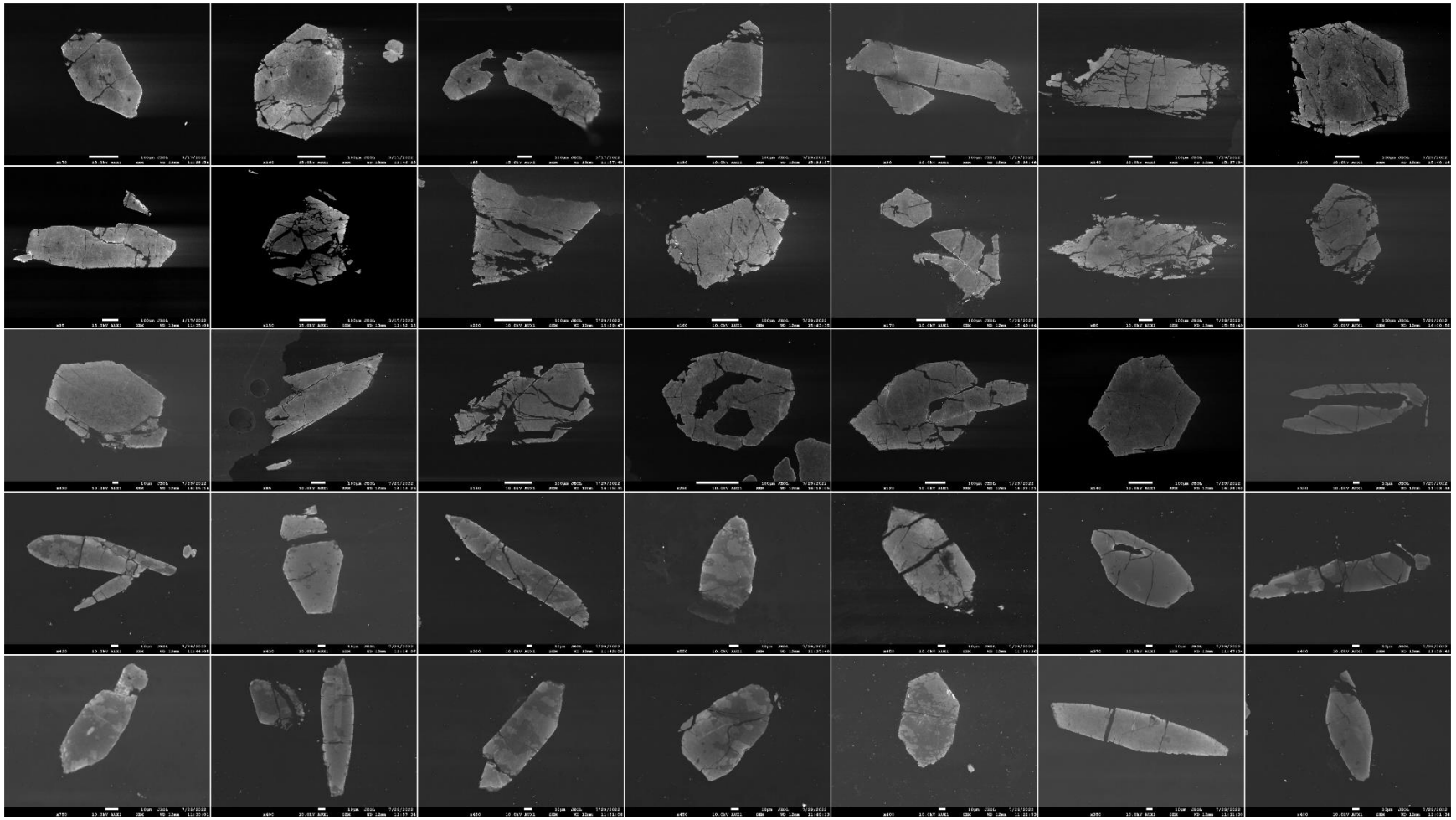

Sample : **16SJP008** (Argyle), Alt: Distal

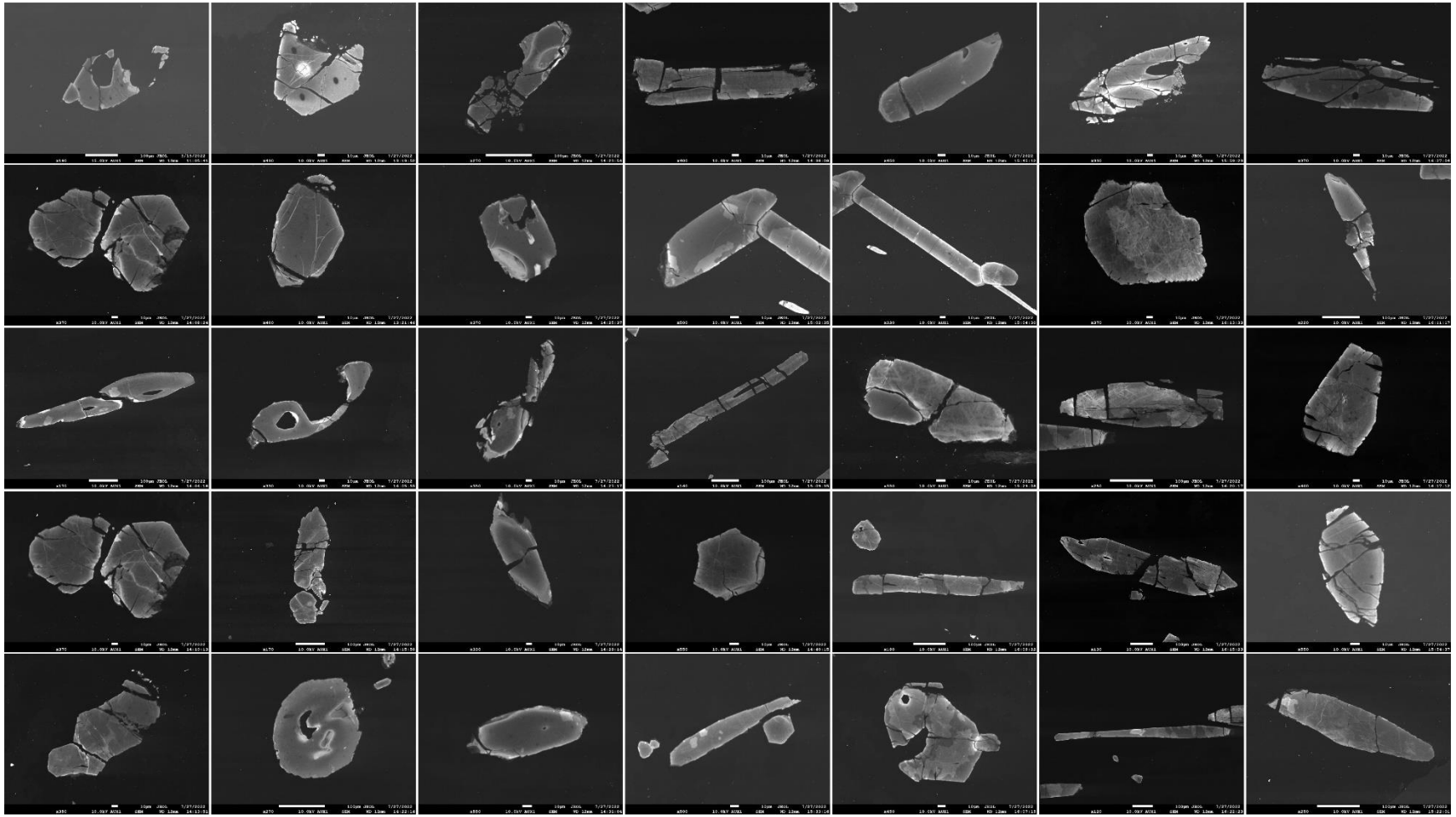

Sample : **195939** (Animal Pond), Alt: Weak

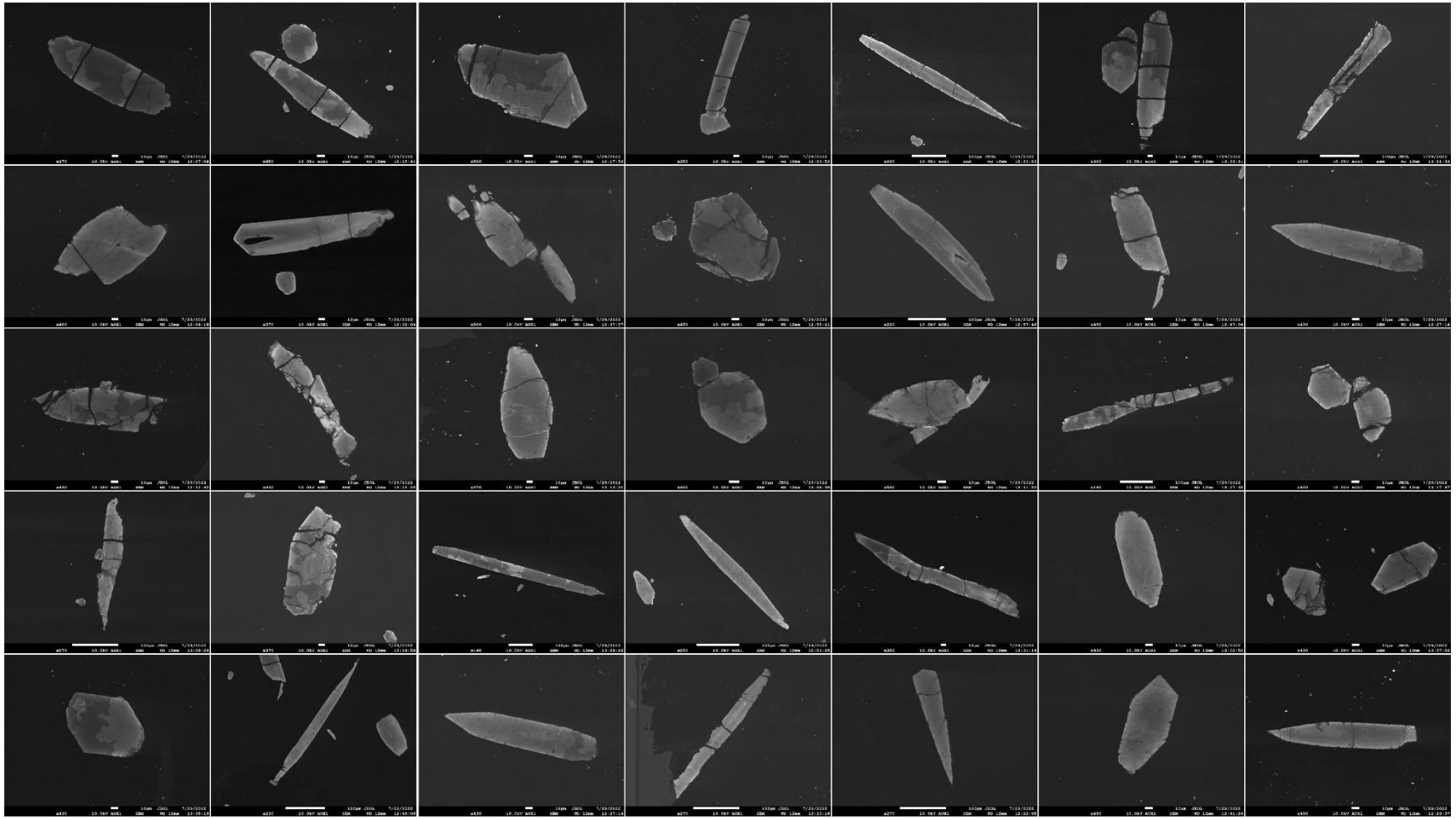

Sample : **195908** (Stog'er Tight), Alt: Strong

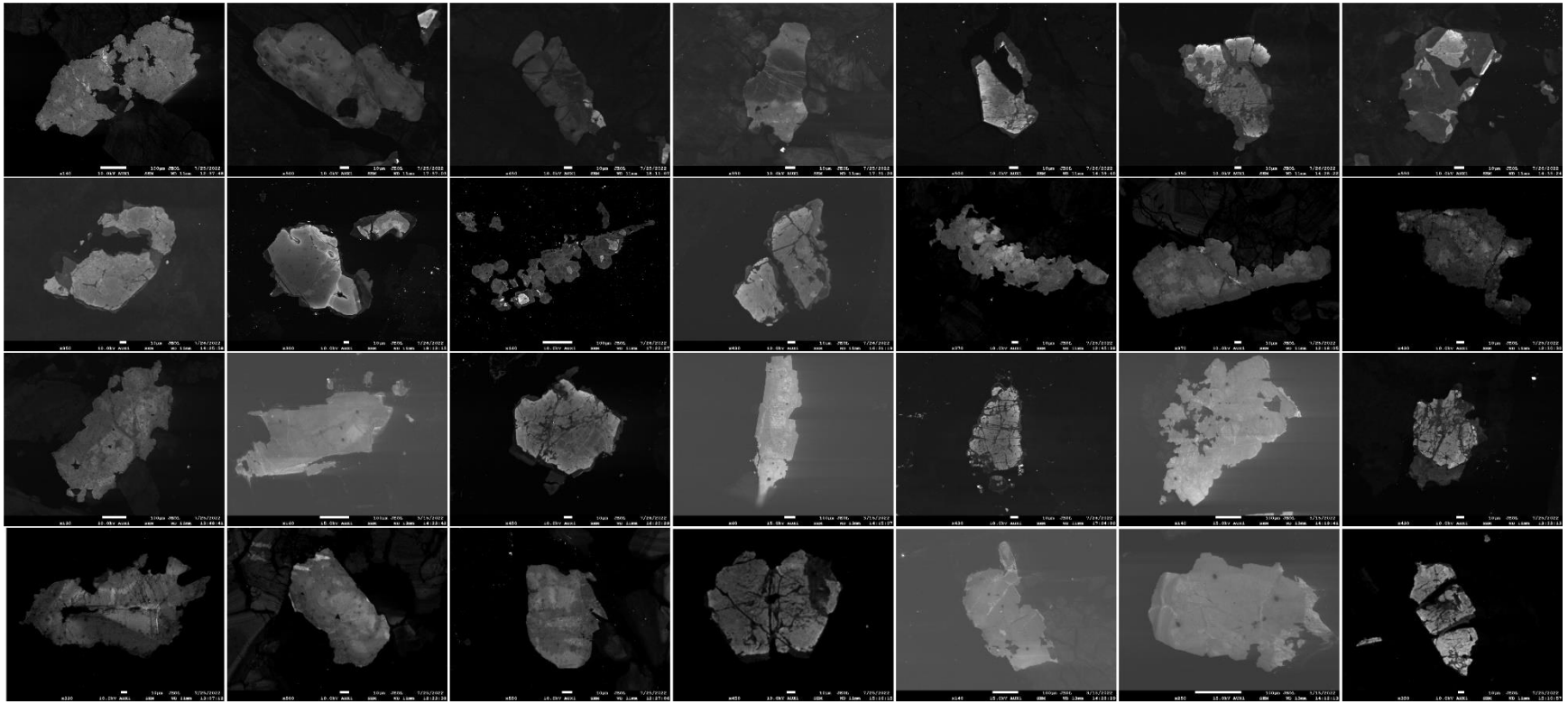

Sample : **195913** (Stog'er Tight), Alt: Strong

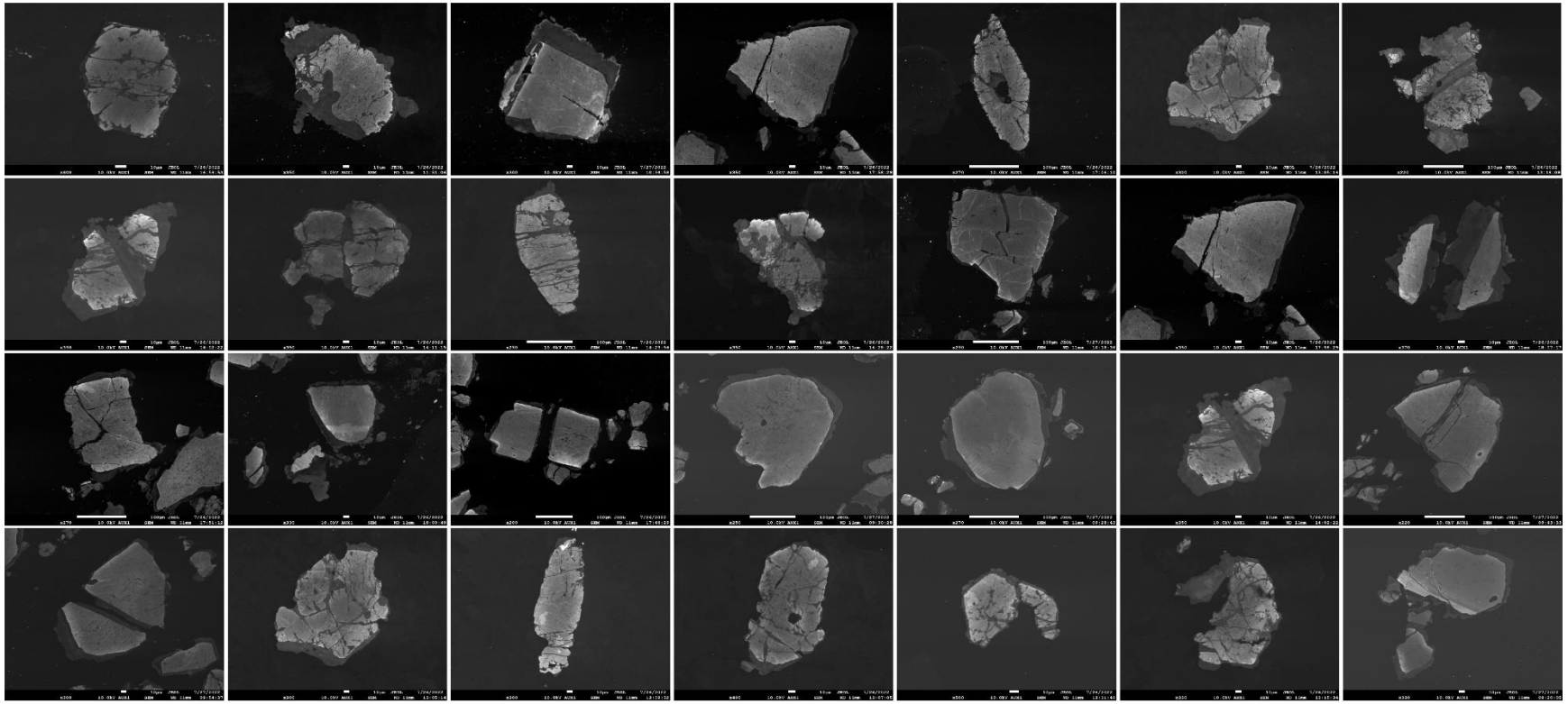

Sample : **16SJP001** (Stog'er Tight), Alt: Proximal

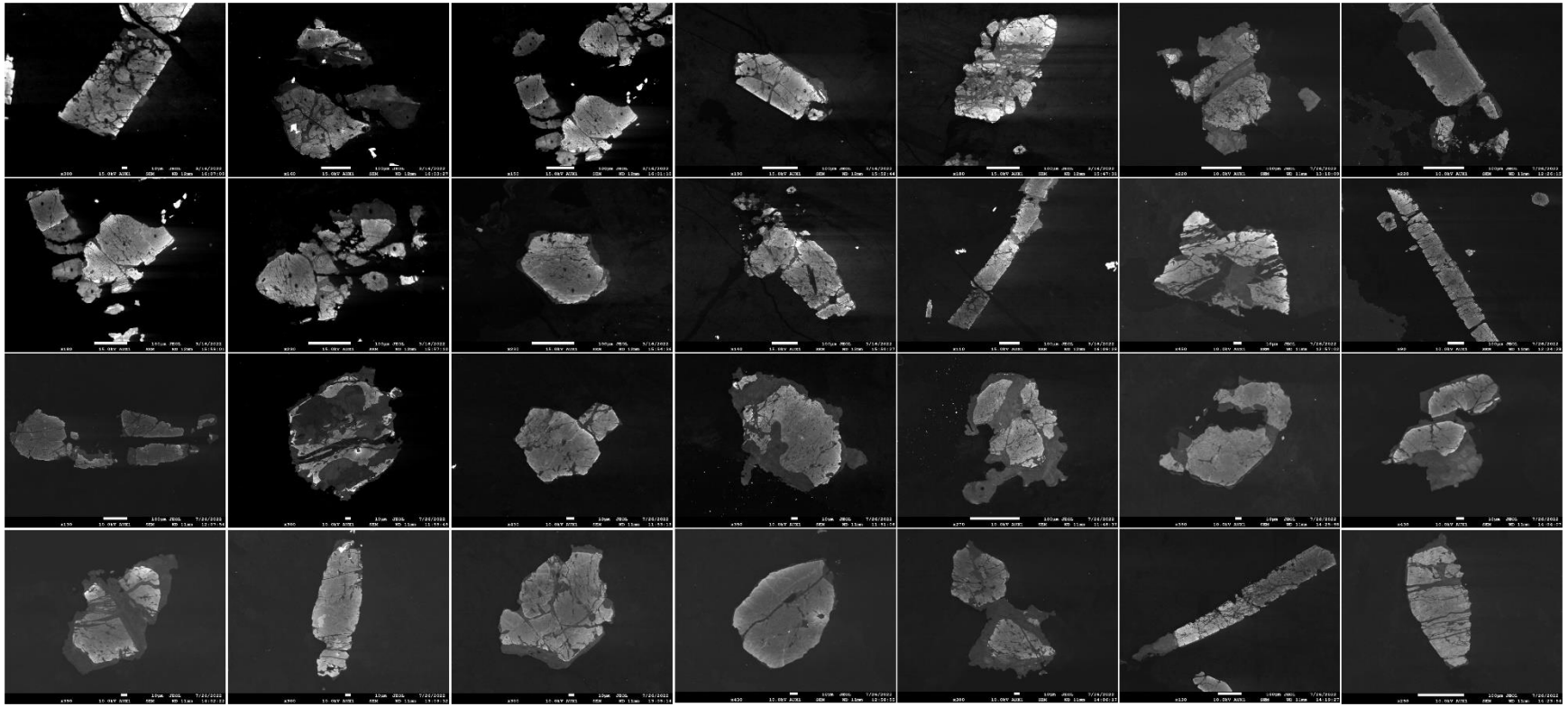

Sample : **16SJP002** (Stog'er Tight), Alt: Proximal

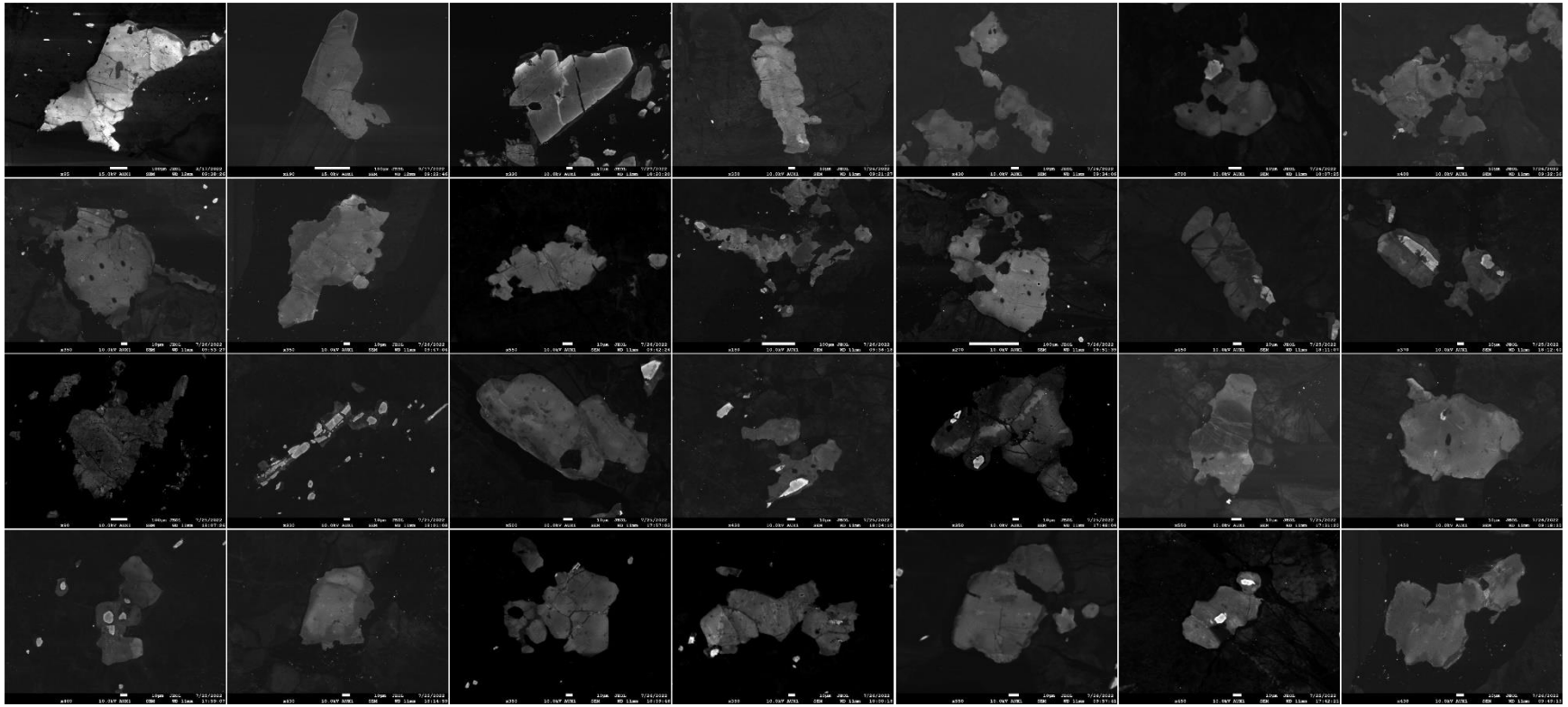

Sample : **I951379** (Argyle), Alt: Proximal

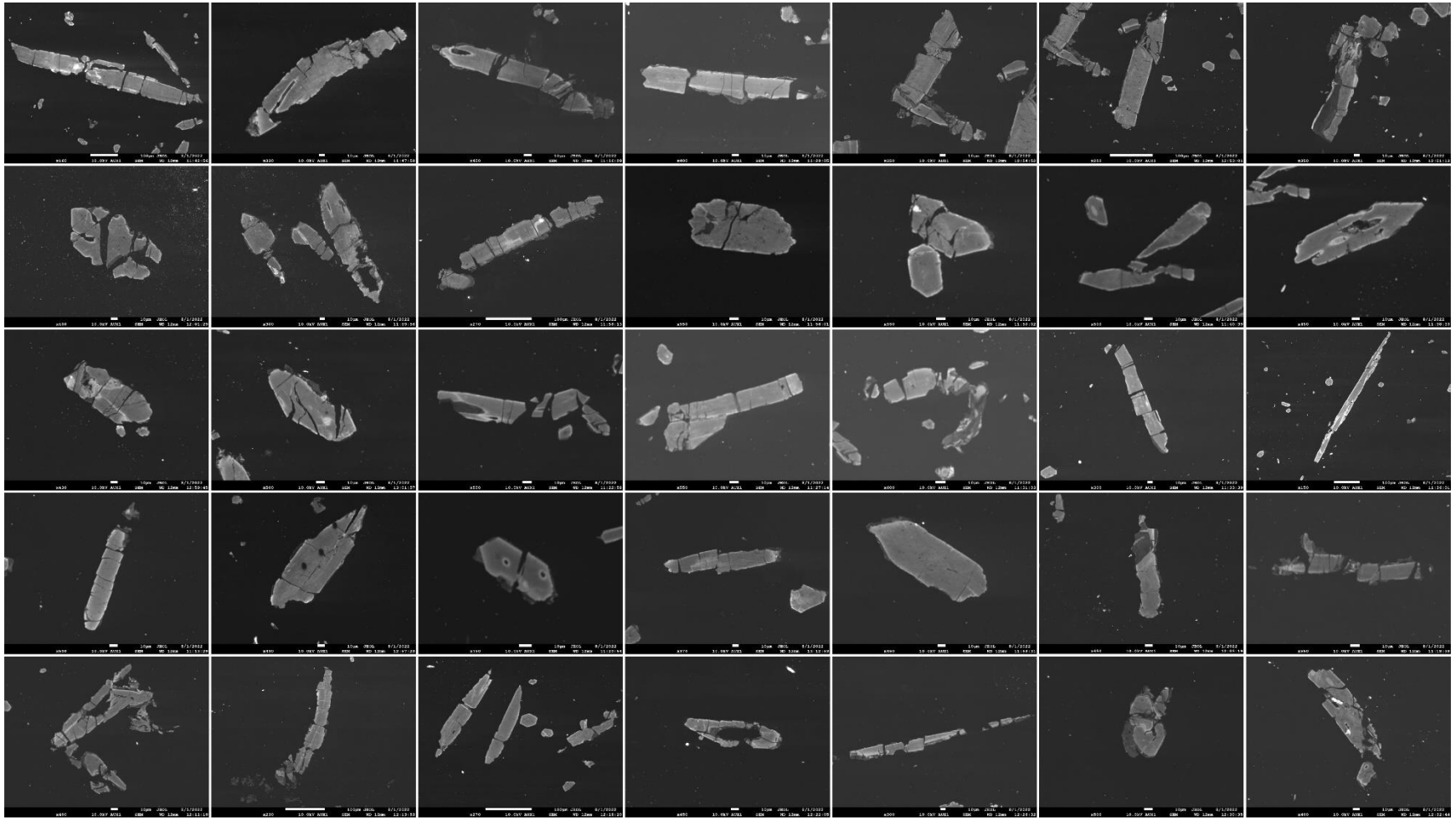

APPENDIX C: Scanning electron microscopy-mineral liberation analysis (SEM-MLA) of the mounts from the Animal Pond Prospect, Stog'er Tight and Argyle deposits

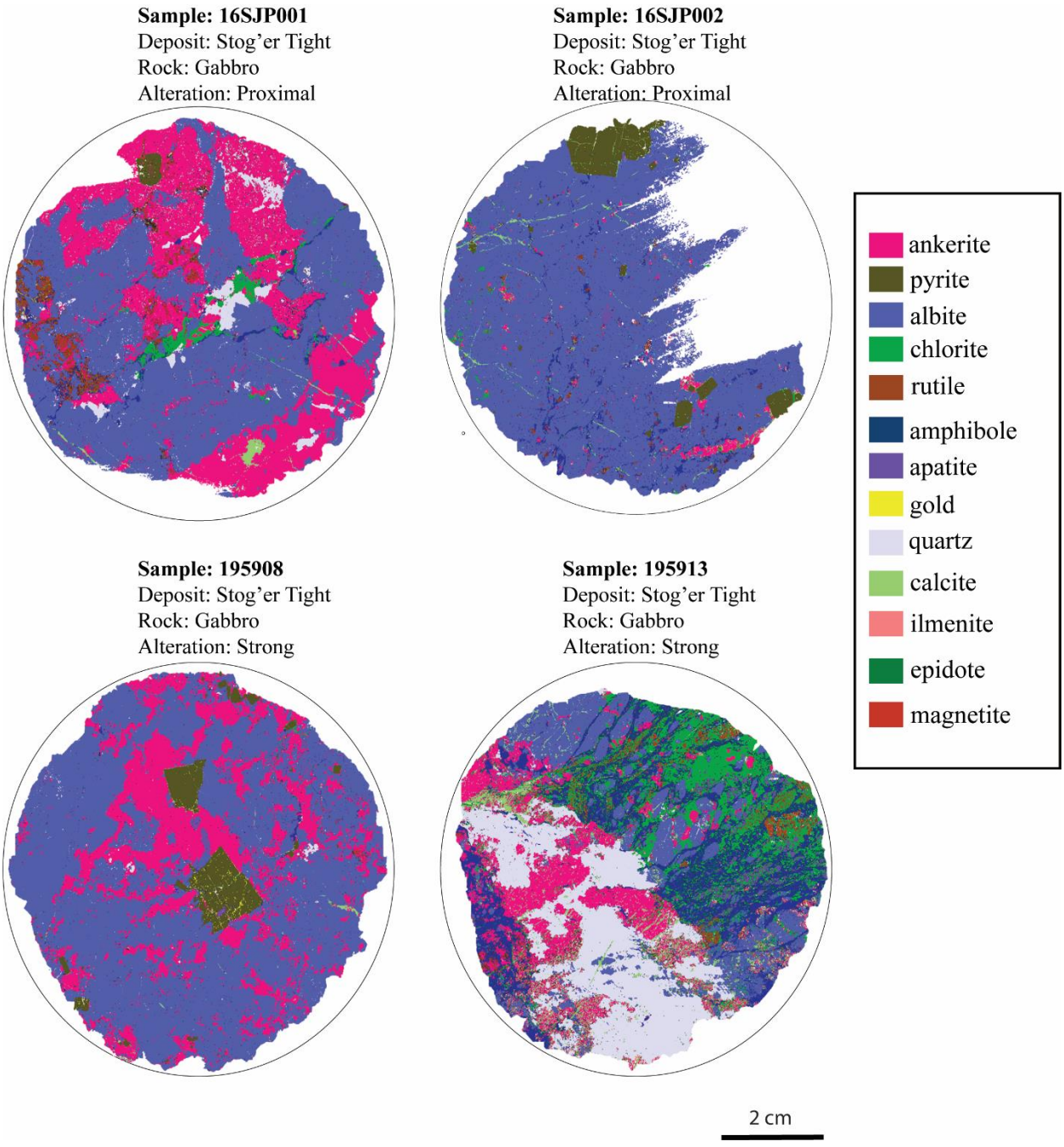

Scanning electron microscopy-mineral liberation analysis (SEM-MLA) of the mounts from the the Animal Pond Prospect, Stog'er Tight and Argyle deposits *(continued)*

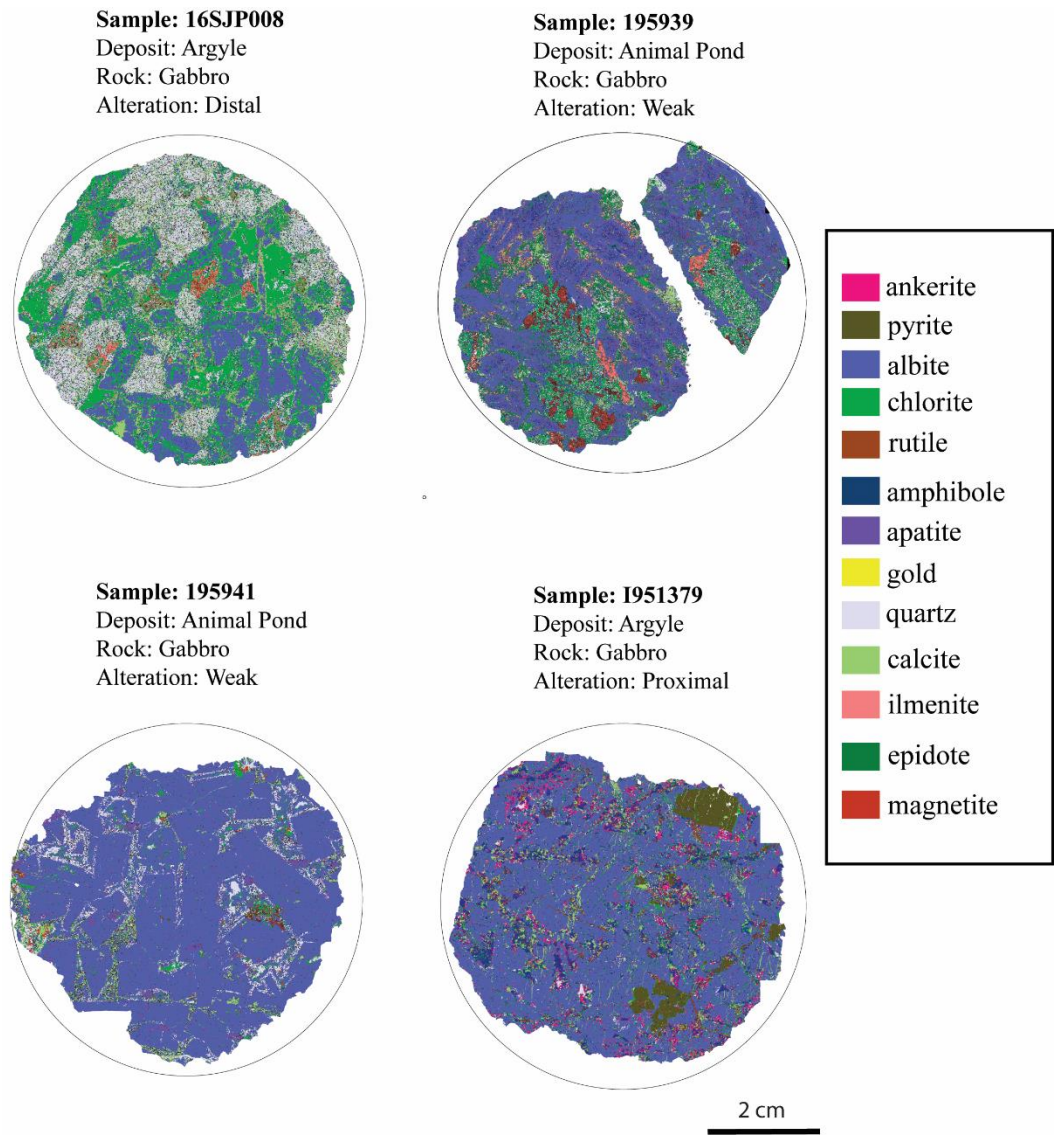

APPENDIX D: Summarized methods for EPMA and EPMA average oxide and apfu results of apatite from the Animal Pond Prospect, Stog'er Tight and Argyle deposits

Table D1. Summary methods for EPMA fluorapatite analyses.

EPMA										
Model	JEOL JXA-8230 Superprobe									
Voltage	15kV									
Current	20 Na									
Spot size	10 µm									
Secondary Standard	JMH fluorapatite 347									
		F	Fe	Mn	Nd	Ce	La	Cl	Ca	S
Peak counting time (s)		10	40	40	40	40	40	20	30	40
Background counting time (s)		5	20	20	20	20	20	10	15	20
Element X-ray line		Kα	Kα	Kα	Lβ	Lα	Lα	Kα	Kα	Kα
Analyzing crystal		LDE1	LIFL	LIFL	LIFL	LIFL	LIFL	PETL	PETL	PETL
Primary standard		JMH_fluor apatite_319	Almandine_Garnet	Rhodenite	NdP_5O14	CeP_5O_{14}	LaP_5O_{14}	JMH_chlor apatite_346	JMH_fluor apatite_319	Sphalerite

P	Na	Si	Mg	As	U	Th	Y	Sr
20	20	40	40	40	40	40	40	40
10	10	20	20	20	20	20	20	20
Kα	Kα	Kα	Kα	Lα	Mα	Mα	Lα	Lα
PETL	TAP	TAP	TAP	TAP	PETH	PETH	PETH	PETH
Apatite	Albite	Albite	Diopside	Arseno pyrite	Syn-UO_2	Syn-Thor	YP_5O14	Celestite

Table D2. Fluorapatite average results from EPMA (wt. %) for oxides in the Animal Pond prospect, Stog'er Tight and Argyle deposits.

Sample	**195939**		**195941**		**16SJP008**		**I951379**	
Deposit	Animal Pond		Animal Pond		Argyle		Argyle	
Rock Type	Gabbro		Gabbro		Gabbro		Gabbro	
Alteration	Weak		Distal		Distal		Proximal	
Luminescence	Yellow green		Yellow green		Yellow green		Dark Green	
CL	Homogeneous		Homogeneous		Homogeneous		Messy	
	Mean	sd	Mean	sd	Mean	sd	Mean	sd
EPMA (wt%)		n=97		n=38		n=108		n=93
SiO_2	0.01	0.04	0.13	0.16	0.21	0.20	0.34	0.27
Na_2O	0.03	0.04	0.02	0.03	0.07	0.12	0.11	0.37
MnO	0.12	0.02	0.08	0.01	0.09	0.02	0.07	0.03
MgO	0.01	0.01	0.01	0.01	0.01	0.01	0.01	0.01
CaO	54.61	0.68	54.21	0.41	53.78	1.05	54.02	1.76
P_2O_5	41.79	0.49	41.17	0.53	41.26	0.68	41.06	1.28
FeO	0.43	0.17	0.33	0.10	0.67	0.45	0.52	0.45
As_2O_5	0.03	0.02	0.07	0.07	0.20	0.20	0.09	0.08
SrO	0.05	0.02	0.08	0.02	0.08	0.02	0.10	0.04
La_2O_3	0.04	0.05	0.05	0.03	0.08	0.10	0.07	0.09
Ce_2O_3	0.13	0.16	0.14	0.08	0.23	0.30	0.23	0.25
Nd_2O_3	0.26	0.28	0.08	0.06	0.11	0.12	0.11	0.12
Y_2O_3	0.07	0.06	0.10	0.05	0.14	0.13	0.14	0.11
UO_2	0.01	0.01	0.01	0.01	0.01	0.01	0.01	0.01
ThO_2	0.00	0.01	0.01	0.01	0.01	0.01	0.01	0.01
SO_3	0.01	0.01	0.01	0.01	0.01	0.01	0.01	0.01
F	2.32	0.23	3.15	0.52	2.95	0.38	3.45	0.48
Cl	0.24	0.13	0.22	0.14	0.36	0.12	0.10	0.09
Total recalculated	100.16		100.34		100.16		100.63	
Total (Mass %)	99.12		99.01		98.84		99.15	

Note: n = number of analyses; sd = standard deviation

Table D2. *(continued)*

Sample	**16SJP001**		**16SJP002**		**195908**		**195913**	
Deposit	Stog'er Tight		Stog'er Tight		Stog'er Tight		Stog'er Tight	
Rock Type	Gabbro		Gabbro		Gabbro		Gabbro	
Alteration	Proximal		Proximal		Strong		Strong	
Luminescence	Dark Green		Gray		Dark Green		Gray	
CL	Messy		Messy		Messy		Messy	
	Mean	sd	Mean	sd	Mean	sd	Mean	sd
EPMA (wt%)		n=140		n=118		n=118		n=200
SiO_2	0.13	0.17	0.23	0.27	0.16	0.13	0.00	0.02
Na_2O	0.04	0.08	0.08	0.23	0.03	0.02	0.01	0.02
MnO	0.04	0.03	0.02	0.02	0.03	0.02	0.06	0.05
MgO	0.01	0.01	0.01	0.01	0.01	0.01	0.01	0.01
CaO	55.08	0.82	55.12	1.09	55.32	0.77	55.15	0.71
P_2O_5	41.85	0.80	41.82	0.84	41.95	0.85	42.00	0.48
FeO	0.16	0.20	0.06	0.07	0.11	0.09	0.39	0.21
As_2O_5	0.06	0.10	0.01	0.02	0.02	0.03	0.01	0.03
SrO	0.11	0.05	0.12	0.06	0.17	0.06	0.05	0.02
La_2O_3	0.04	0.04	0.04	0.04	0.03	0.03	0.03	0.04
Ce_2O_3	0.09	0.12	0.09	0.14	0.06	0.07	0.07	0.10
Nd_2O_3	0.06	0.05	0.06	0.06	0.05	0.03	0.13	0.15
Y_2O_3	0.07	0.06	0.09	0.11	0.06	0.04	0.04	0.04
UO_2	0.01	0.01	0.01	0.01	0.01	0.01	0.01	0.01
ThO_2	0.01	0.01	0.01	0.01	0.01	0.01	0.00	0.01
SO_3	0.01	0.01	0.02	0.01	0.02	0.05	0.01	0.01
F	3.65	0.47	3.59	0.45	3.89	0.63	3.10	0.37
Cl	0.02	0.02	0.02	0.02	0.02	0.01	0.06	0.09
Total recalculated	101.32		101.17		101.77		101.13	
Total (Mass %)	99.78		99.66		100.13		99.82	

Note: n = number of analyses; sd = standard deviation

APPENDIX E: Summarized methods for LASS (LA-ICPMS and LA-MC- ICPMS) and trace element results of apatite from the Animal Pond Prospect, Stog'er Tight and Argyle deposits

Table E1. Summary methods for LASS fluorapatite analyses.

LASS	
Model	Thermo-Finnigan ELEMENT XR coupled with a GeoLas 193 nm Excimer laser system
Pulse frequency	10 Hz
Energy density	5 j/cm^2
Spot size	99-109 μm
Gas blank	30s
Signal	60s
Internal Standard	Ca (from EPMA)
Primary reference material	NIST-610 (ICP-MS), TH-1(MC-ICPMS)
Secondary reference material	NIST-612, BCR2G (ICPMS); MAD02, Durango apatite (MC-ICPMS)
Elements/Isotopes	^{43}Ca, ^{25}Mg, ^{27}Al, ^{29}Si, ^{31}P, ^{39}K, ^{45}Sc, ^{49}Ti, ^{51}V, ^{53}Cr, ^{55}Mn, ^{57}Fe, ^{75}As, ^{88}Sr, ^{89}Y, ^{90}Zr, ^{93}Nb, ^{137}Ba, ^{139}La, ^{140}Ce, ^{141}Pr, ^{146}Nd, ^{147}Sm, ^{153}Eu, ^{157}Gd, ^{159}Tm, ^{163}Dy, ^{165}Ho, ^{166}Er, ^{169}Tm, ^{172}Yb, ^{175}Lu, ^{178}Hf, ^{181}Ta, ^{208}Pb, ^{232}Th, ^{238}U

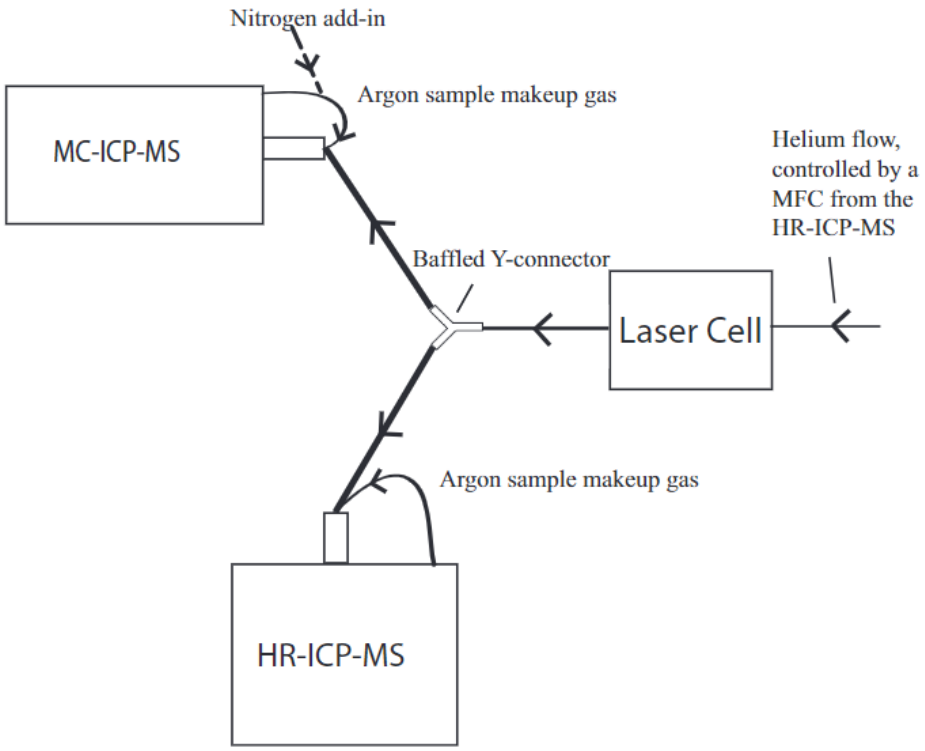

Figure E1. LASS analytical setup (Goudie et al., 2014).

Table E2. Fluorapatite average results from LA-ICP-MS (ppm) for trace elements in the Animal Pond prospect, Stog'er Tight and Argyle deposits.

Sample	**195939**		**195941**		**16SJP008**		**I951379**	
Deposit	Animal Pond		Animal Pond		Argyle		Argyle	
Rock Type	Gabbro		Gabbro		Gabbro		Gabbro	
Alteration	Weak		Distal		Distal		Proximal	
	Mean	sd	Mean	sd	Mean	sd	Mean	sd
LA-ICPMS (ppm)		n=34		n=40		n=57		n=28
Mg	2744.12	2140.27	1682.88	1426.66	4895.00	2490.32	4385.56	2086.95
Sc	19.56	30.80	1.74	0.52	24.81	24.07	20.81	40.63
Ti	75.40	31.53	62.00	32.91	72.23	51.19	94.09	67.70
V	108.07	97.19	7.93	3.05	247.35	202.44	72.15	98.47
Mn	827.63	184.23	606.28	118.99	1118.09	403.16	804.17	205.58
As	45.75	27.16	33.28	25.74	25.58	20.19	108.58	374.79
Sr	871.65	175.98	678.25	49.77	723.68	111.07	779.63	93.00
Y	1083.15	265.43	693.05	178.60	1177.63	512.82	1129.21	163.85
Zr	54.35	97.81	18.03	12.59	22.89	28.23	134.86	237.02
Nb	10.76	25.39	2.02	4.40	7.78	18.91	8.94	21.21
La	550.32	118.16	315.88	117.23	665.65	332.13	629.79	154.69
Ce	1560.59	308.58	945.95	308.62	1872.84	910.87	1824.07	431.23
Pr	242.35	44.40	150.79	45.52	284.04	131.13	277.94	61.40
Nd	1170.50	193.43	788.48	244.05	1364.77	578.32	1385.46	282.01
Sm	290.82	42.84	205.38	50.80	329.18	139.08	350.64	81.27
Eu	61.32	12.89	46.08	6.76	56.20	10.21	77.26	16.69
Gd	294.24	44.62	218.97	54.48	331.85	127.89	356.56	56.84
Tb	39.84	7.03	27.37	6.72	43.79	18.59	44.51	7.67
Dy	226.06	45.21	153.44	39.49	246.58	105.00	240.43	41.95
Ho	40.23	10.59	27.44	7.84	44.33	18.72	44.58	6.49
Er	98.63	30.85	65.35	18.31	108.98	49.20	104.88	20.21
Tm	11.16	4.56	7.14	1.66	12.16	5.97	12.74	5.35
Yb	59.89	27.45	36.32	9.45	63.80	35.92	63.09	11.22
Lu	7.56	3.88	4.56	1.19	8.01	5.05	7.87	2.10
Pb	1.91	1.50	0.45	0.18	1.39	1.42	2.27	1.65
Th	9.96	24.51	3.30	1.22	9.79	19.85	9.79	7.67

U	4.35	13.50	1.43	0.33	4.30	12.19	3.78	2.86
∑REE	4653.51	826.13	2993.12	907.81	5432.20	2419.79	5424.17	1116.05
Th/U	2.79	1.46	2.28	0.36	2.62	0.99	3.40	3.74
Sr/Y	0.83	0.21	1.01	0.15	0.72	0.31	0.69	0.19
Ce/Ce*	1.06	0.04	1.06	0.03	1.06	0.04	1.06	0.04
Eu/Eu*	0.64	0.11	0.67	0.05	0.56	0.15	0.67	0.07

Table E2. *(continued)*

Sample	**16SJP001**		**16SJP002**		**195908**		**195913**	
Deposit	Stog'er Tight		Stog'er Tight		Stog'er Tight		Stog'er Tight	
Rock Type	Gabbro		Gabbro		Gabbro		Gabbro	
Alteration	Proximal		Proximal		Strong		Strong	
	Mean	sd	Mean	sd	Mean	sd	Mean	sd
LA-ICPMS (ppm)		n=49		n=50		n=57		n=45
Mg	405.93	211.10	80.67	182.99	279.99	353.00	2041.63	2145.96
Sc	2.50	2.80	1.40	2.85	2.23	4.59	2.29	1.67
Ti	62.18	40.09	19.39	43.67	24.41	35.94	60.60	53.31
V	5.50	7.77	6.54	22.29	6.33	10.59	34.11	46.54
Mn	307.35	106.43	103.64	120.54	192.24	207.58	515.44	107.10
As	9.38	5.42	7.55	1.25	9.75	6.81	17.76	9.56
Sr	926.24	170.45	984.24	218.58	1368.86	368.43	796.11	86.17
Y	704.65	460.98	618.36	166.97	509.99	213.99	863.71	242.87
Zr	12.30	6.86	24.62	83.07	35.70	118.11	48.07	111.36
Nb	0.72	0.88	10.50	51.89	4.34	18.69	0.61	0.85
La	342.69	310.82	64.97	69.40	104.22	150.83	422.59	253.61
Ce	985.40	799.29	255.75	192.89	347.52	424.02	1213.13	586.92
Pr	157.62	119.97	50.67	28.43	61.41	61.26	187.85	75.84
Nd	792.37	514.65	323.32	138.77	365.23	292.39	955.78	330.53

Sm	217.99	111.46	154.45	32.00	147.37	56.29	247.27	74.65
Eu	60.55	34.23	70.86	16.52	54.53	14.37	56.74	12.21
Gd	234.36	93.96	229.37	40.03	197.85	54.75	268.71	64.33
Tb	30.56	13.05	33.94	6.11	27.65	7.35	36.06	8.60
Dy	163.92	86.12	177.23	37.38	142.67	41.36	194.72	46.37
Ho	28.19	17.48	28.05	7.40	21.63	7.39	33.77	8.74
Er	66.07	44.87	62.73	20.29	45.63	19.45	80.88	22.80
Tm	7.12	4.86	6.10	2.11	4.51	2.16	8.83	2.67
Yb	36.32	25.75	27.30	10.04	20.85	11.79	45.04	12.54
Lu	4.45	3.57	3.27	1.62	2.31	1.56	5.49	1.50
Pb	3.97	1.73	6.54	2.49	11.92	4.86	1.38	0.63
Th	3.07	2.38	2.16	2.45	1.84	3.47	4.79	3.45
U	1.02	0.44	0.49	1.14	0.49	0.67	1.57	0.54
∑REE	3127.60	2133.42	1487.99	537.30	1543.37	1092.77	3756.85	1460.82
Th/U	3.61	2.65	16.78	18.12	2.93	2.54	3.63	4.62
Sr/Y	1.58	0.79	1.77	0.81	3.41	2.49	1.01	0.41
Ce/Ce*	1.05	0.04	1.15	0.08	1.14	0.06	1.05	0.03
Eu/Eu*	0.81	0.12	1.16	0.22	1.02	0.21	0.69	0.10

Note: n = number of analyses; sd = standard deviation

APPENDIX F: Nd results for apatite grains from LASS, and calculation of $\varepsilon_{Nd}(t)$

Table F1. Sm–Nd isotopic data from for apatite grains from LASS, and calculation of $\varepsilon_{Nd}(t)$

Sample	Deposit	Alteration	$^{143}Nd/^{144}Nd$	2SE	$^{147}Sm/^{144}Nd$	2SE	Age (Ma)	ε_{Ndt}	$^{143}Nd/^{144}Nd_t$	T_{DM}
16SJP008_1_1	Argyle	Distal	0.512774	0.000035	0.14537	0.00057	420	5.41	0.512374	0.7825
16SJP008_2_1	Argyle	Distal	0.512769	0.000032	0.13498	0.00034	420	5.87	0.512398	0.6864
16SJP008_3_1	Argyle	Distal	0.512786	0.000032	0.15231	0.00057	420	5.27	0.512367	0.8433
16SJP008_4_1	Argyle	Distal	0.512752	0.000031	0.13707	0.00060	420	5.42	0.512375	0.7404
16SJP008_5_1	Argyle	Distal	0.512710	0.000031	0.13974	0.00052	420	4.46	0.512326	0.8570
16SJP008_7_1	Argyle	Distal	0.512729	0.000032	0.14141	0.00028	420	4.74	0.512340	0.8361
16SJP008_8_1	Argyle	Distal	0.512752	0.000024	0.14093	0.00013	420	5.22	0.512364	0.7809
16SJP008_9_1	Argyle	Distal	0.512752	0.000023	0.14310	0.00098	420	5.10	0.512358	0.8056
16SJP008_10_1	Argyle	Distal	0.512738	0.000026	0.14093	0.00038	420	4.94	0.512350	0.8111
16SJP008_11_1	Argyle	Distal	0.512788	0.000045	0.14588	0.00019	420	5.65	0.512387	0.7561
16SJP008_12_1	Argyle	Distal	0.512789	0.000025	0.14728	0.00014	420	5.60	0.512384	0.7702
16SJP008_13_1	Argyle	Distal	0.512746	0.000029	0.13338	0.00028	420	5.50	0.512379	0.7172
16SJP008_1	Argyle	Distal	0.512770	0.000032	0.14878	0.00015	420	5.15	0.512361	0.8347
16SJP008_2	Argyle	Distal	0.512761	0.000051	0.14380	0.00110	420	5.24	0.512365	0.7937
16SJP008_3	Argyle	Distal	0.512774	0.000027	0.14231	0.00040	420	5.57	0.512383	0.7480
16SJP008_4	Argyle	Distal	0.512822	0.000035	0.15189	0.00023	420	5.99	0.512404	0.7454
16SJP008_5	Argyle	Distal	0.512799	0.000028	0.14914	0.00011	420	5.69	0.512389	0.7687
16SJP008_6	Argyle	Distal	0.512754	0.000029	0.14526	0.00011	420	5.02	0.512354	0.8272
16JP008_8	Argyle	Distal	0.512746	0.000050	0.14380	0.00160	420	4.94	0.512350	0.8274
16JP008_9	Argyle	Distal	0.512766	0.000049	0.14020	0.00240	420	5.53	0.512380	0.7430
16JP008_10	Argyle	Distal	0.512743	0.000025	0.13490	0.00150	420	5.36	0.512372	0.7374

16JP008_12	Argyle	Distal	0.512787	0.000054	0.14140	0.00140	420	5.87	0.512398	0.7100
16JP008_14	Argyle	Distal	0.512780	0.000037	0.14690	0.00140	420	5.44	0.512376	0.7869
16JP008_15	Argyle	Distal	0.512732	0.000043	0.14110	0.00140	420	4.82	0.512344	0.8260
16JP008_17	Argyle	Distal	0.512667	0.000050	0.13722	0.00054	420	3.76	0.512290	0.9161
16JP008_22	Argyle	Distal	0.512801	0.000034	0.14126	0.00020	420	6.16	0.512412	0.6783
16JP008_23	Argyle	Distal	0.512789	0.000048	0.15069	0.00032	420	5.41	0.512375	0.8133
16JP008_24	Argyle	Distal	0.512744	0.000056	0.14239	0.00016	420	4.98	0.512352	0.8149
16JP008_25	Argyle	Distal	0.512733	0.000076	0.15090	0.00100	420	4.31	0.512318	0.9568
16JP008_26	Argyle	Distal	0.512823	0.000040	0.15050	0.00013	420	6.09	0.512409	0.7259
16JP008_27	Argyle	Distal	0.512738	0.000046	0.15302	0.00019	420	4.29	0.512317	0.9784
16JP008_28	Argyle	Distal	0.512796	0.000052	0.15554	0.00035	420	5.29	0.512368	0.8647
16JP008_29	Argyle	Distal	0.512762	0.000037	0.14871	0.00083	420	4.99	0.512353	0.8532
16JP008_30	Argyle	Distal	0.512748	0.000068	0.15052	0.00065	420	4.62	0.512334	0.9134
16JP008_31	Argyle	Distal	0.512640	0.000053	0.15380	0.00220	420	2.34	0.512217	1.2496
16JP008_32	Argyle	Distal	0.512769	0.000033	0.14150	0.00120	420	5.52	0.512380	0.7502
16JP008_34	Argyle	Distal	0.512771	0.000028	0.14839	0.00039	420	5.19	0.512363	0.8272
16JP008_35	Argyle	Distal	0.512783	0.000033	0.14582	0.00033	420	5.56	0.512382	0.7670
16JP008_36	Argyle	Distal	0.512765	0.000042	0.14496	0.00016	420	5.25	0.512366	0.7983
16JP008_37	Argyle	Distal	0.512793	0.000037	0.14412	0.00058	420	5.85	0.512397	0.7251
16JP008_38	Argyle	Distal	0.512759	0.000033	0.14569	0.00016	420	5.10	0.512358	0.8210
16JP008_39	Argyle	Distal	0.512739	0.000024	0.14593	0.00014	420	4.69	0.512338	0.8705
16JP008_40	Argyle	Distal	0.512748	0.000041	0.14982	0.00041	420	4.66	0.512336	0.9030
16JP008_41	Argyle	Distal	0.512797	0.000028	0.15279	0.00030	420	5.46	0.512377	0.8216
16JP008_42	Argyle	Distal	0.512762	0.000039	0.14912	0.00046	420	4.97	0.512352	0.8588
16JP008_43	Argyle	Distal	0.512793	0.000040	0.14494	0.00056	420	5.80	0.512394	0.7340
195941_1_1	Animal Pond	Weak	0.512770	0.000033	0.15154	0.00009	420	5.00	0.512353	0.8730
195941_2_1	Animal Pond	Weak	0.512793	0.000037	0.15138	0.00024	420	5.46	0.512377	0.8125

195941_3_1	Animal Pond	Weak	0.512790	0.000036	0.15172	0.00078	420	5.38	0.512373	0.8248
195941_4_1	Animal Pond	Weak	0.512732	0.000026	0.15255	0.00015	420	4.20	0.512312	0.9861
195941_5_1	Animal Pond	Weak	0.512764	0.000027	0.15070	0.00008	420	4.93	0.512349	0.8760
195941_6_1	Animal Pond	Weak	0.512787	0.000034	0.15189	0.00031	420	5.31	0.512369	0.8348
195941_7_1	Animal Pond	Weak	0.512795	0.000037	0.15212	0.00044	420	5.45	0.512377	0.8175
195941_8_1	Animal Pond	Weak	0.512793	0.000059	0.15160	0.00072	420	5.44	0.512376	0.8155
195941_9_1	Animal Pond	Weak	0.512821	0.000022	0.15070	0.00026	420	6.04	0.512406	0.7333
195941_10_1	Animal Pond	Weak	0.512842	0.000032	0.15331	0.00009	420	6.31	0.512420	0.7112
195941_11_1	Animal Pond	Weak	0.512802	0.000024	0.15273	0.00005	420	5.56	0.512382	0.8079
195941_12_1	Animal Pond	Weak	0.512790	0.000037	0.15006	0.00038	420	5.47	0.512377	0.8025
195941_13_1	Animal Pond	Weak	0.512781	0.000032	0.15291	0.00048	420	5.14	0.512360	0.8649
195941_14_1	Animal Pond	Weak	0.512786	0.000022	0.15168	0.00016	420	5.30	0.512369	0.8344
195941_15_1	Animal Pond	Weak	0.512806	0.000025	0.15277	0.00010	420	5.63	0.512386	0.7980
195941_17_1	Animal Pond	Weak	0.512816	0.000048	0.15541	0.00029	420	5.69	0.512389	0.8084
195941_18_1	Animal Pond	Weak	0.512799	0.000036	0.15299	0.00019	420	5.49	0.512378	0.8192
195941_1	Animal Pond	Weak	0.512815	0.000031	0.15196	0.00005	420	5.85	0.512397	0.7641
195941_2	Animal Pond	Weak	0.512802	0.000020	0.15135	0.00028	420	5.63	0.512386	0.7893
195941_3	Animal Pond	Weak	0.512801	0.000030	0.15260	0.00038	420	5.55	0.512381	0.8086
195941_5	Animal Pond	Weak	0.512832	0.000047	0.15255	0.00081	420	6.15	0.512412	0.7279
195941_6	Animal Pond	Weak	0.512787	0.000030	0.15485	0.00037	420	5.15	0.512361	0.8783
195941_7	Animal Pond	Weak	0.512810	0.000028	0.15218	0.00013	420	5.74	0.512391	0.7798
195941_8	Animal Pond	Weak	0.512830	0.000034	0.15470	0.00046	420	6.00	0.512404	0.7607
195941_9	Animal Pond	Weak	0.512817	0.000025	0.15061	0.00022	420	5.97	0.512403	0.7422
195941_10	Animal Pond	Weak	0.512795	0.000022	0.15211	0.00020	420	5.46	0.512377	0.8174
195941_11	Animal Pond	Weak	0.512825	0.000040	0.15263	0.00006	420	6.01	0.512405	0.7469
195941_12	Animal Pond	Weak	0.512829	0.000026	0.14938	0.00041	420	6.27	0.512418	0.6981
195941_13	Animal Pond	Weak	0.512768	0.000037	0.15152	0.00022	420	4.96	0.512351	0.8779

195941_14	Animal Pond	Weak	0.512757	0.000039	0.15208	0.00006	420	4.71	0.512339	0.9143
195941_15	Animal Pond	Weak	0.512812	0.000036	0.15077	0.00011	420	5.86	0.512397	0.7567
195941_16	Animal Pond	Weak	0.512796	0.000036	0.15050	0.00009	420	5.56	0.512382	0.7933
195941_17	Animal Pond	Weak	0.512790	0.000031	0.15194	0.00007	420	5.37	0.512372	0.8278
195941_18	Animal Pond	Weak	0.512805	0.000034	0.15222	0.00015	420	5.64	0.512386	0.7932
195941_19	Animal Pond	Weak	0.512833	0.000020	0.15127	0.00013	420	6.24	0.512417	0.7099
195941_20	Animal Pond	Weak	0.512814	0.000030	0.15228	0.00021	420	5.82	0.512395	0.7709
195941_21	Animal Pond	Weak	0.512789	0.000048	0.15050	0.00100	420	5.42	0.512375	0.8108
195941_22	Animal Pond	Weak	0.512848	0.000031	0.15012	0.00034	420	6.60	0.512435	0.6594
195939_1	Animal Pond	Distal	0.512751	0.000055	0.14032	0.00057	420	5.23	0.512365	0.7763
195939_2	Animal Pond	Distal	0.512753	0.000041	0.14337	0.00089	420	5.10	0.512359	0.8065
195939_3	Animal Pond	Distal	0.512747	0.000061	0.14130	0.00250	420	5.10	0.512358	0.7958
195939_4	Animal Pond	Distal	0.512767	0.000023	0.14659	0.00053	420	5.20	0.512364	0.8136
195939_5	Animal Pond	Distal	0.512656	0.000039	0.13948	0.00090	420	3.42	0.512272	0.9680
195939_6	Animal Pond	Distal	0.512748	0.000056	0.14130	0.00180	420	5.12	0.512359	0.7936
195939_7	Animal Pond	Distal	0.512726	0.000055	0.13780	0.00210	420	4.88	0.512347	0.8015
195939_8	Animal Pond	Distal	0.512749	0.000025	0.14384	0.00020	420	5.00	0.512353	0.8211
195939_9	Animal Pond	Distal	0.512747	0.000030	0.14179	0.00092	420	5.07	0.512357	0.8014
195939_13	Animal Pond	Distal	0.512683	0.000051	0.14260	0.00072	420	3.78	0.512291	0.9521
195939_14	Animal Pond	Distal	0.512695	0.000070	0.14458	0.00081	420	3.91	0.512297	0.9530
195939_15	Animal Pond	Distal	0.512751	0.000061	0.14424	0.00078	420	5.02	0.512354	0.8215
195939_16	Animal Pond	Distal	0.512757	0.000021	0.14314	0.00015	420	5.19	0.512363	0.7949
195939_17	Animal Pond	Distal	0.512759	0.000037	0.15330	0.00320	420	4.69	0.512337	0.9282
195939_18	Animal Pond	Distal	0.512751	0.000056	0.14608	0.00062	420	4.92	0.512349	0.8445
195939_19	Animal Pond	Distal	0.512728	0.000051	0.14325	0.00072	420	4.62	0.512334	0.8609
195939_21	Animal Pond	Distal	0.512752	0.000061	0.15120	0.00140	420	4.66	0.512336	0.9136
195939_22	Animal Pond	Distal	0.512685	0.000073	0.14049	0.00089	420	3.93	0.512299	0.9196

195939_23	Animal Pond	Distal	0.512604	0.000063	0.14140	0.00100	420	2.30	0.512215	1.1072
195939_24	Animal Pond	Distal	0.512778	0.000025	0.14280	0.00100	420	5.62	0.512385	0.7444
195939_26	Animal Pond	Distal	0.512686	0.000050	0.14033	0.00052	420	3.96	0.512300	0.9154
195939_28	Animal Pond	Distal	0.512773	0.000029	0.14527	0.00049	420	5.39	0.512373	0.7837
195939_29	Animal Pond	Distal	0.512734	0.000038	0.14777	0.00029	420	4.50	0.512328	0.9075
195939_30	Animal Pond	Distal	0.512718	0.000063	0.14851	0.00068	420	4.14	0.512310	0.9568
195939_31	Animal Pond	Distal	0.512776	0.000032	0.15690	0.00120	420	4.83	0.512344	0.9419
195939_32	Animal Pond	Distal	0.512789	0.000047	0.14211	0.00026	420	5.88	0.512398	0.7129
195939_33	Animal Pond	Distal	0.512720	0.000022	0.14964	0.00032	420	4.12	0.512308	0.9693
195939_34	Animal Pond	Distal	0.512747	0.000033	0.14919	0.00030	420	4.67	0.512337	0.8964
195939_35	Animal Pond	Distal	0.512809	0.000018	0.14773	0.00012	420	5.96	0.512403	0.7279
195939_36	Animal Pond	Distal	0.512739	0.000053	0.14566	0.00017	420	4.71	0.512338	0.8669
195913_1	Stog'er Tight	Strong	0.512834	0.000026	0.15500	0.00110	420	6.06	0.512408	0.7540
195913_3	Stog'er Tight	Strong	0.512851	0.000031	0.16403	0.00077	420	5.91	0.512400	NA
195913_6	Stog'er Tight	Strong	0.512799	0.000061	0.15760	0.00110	420	5.24	0.512366	0.8892
195913_7	Stog'er Tight	Strong	0.512764	0.000060	0.16120	0.00200	420	4.36	0.512321	NA
195913_8	Stog'er Tight	Strong	0.512778	0.000083	0.15520	0.00100	420	4.96	0.512351	0.9081
195913_9	Stog'er Tight	Strong	0.512781	0.000044	0.16290	0.00110	420	4.60	0.512333	NA
195913_10	Stog'er Tight	Strong	0.512810	0.000055	0.16189	0.00063	420	5.22	0.512365	NA
195913_13	Stog'er Tight	Strong	0.512805	0.000037	0.15970	0.00130	420	5.24	0.512366	0.9075
195913_14	Stog'er Tight	Strong	0.512838	0.000035	0.16240	0.00160	420	5.74	0.512391	NA
195913_15	Stog'er Tight	Strong	0.512771	0.000040	0.14718	0.00062	420	5.25	0.512366	0.8116
195913_16_1	Stog'er Tight	Strong	0.512807	0.000030	0.15302	0.00031	420	5.64	0.512386	0.7988
195913_16_2	Stog'er Tight	Strong	0.512820	0.000029	0.15177	0.00020	420	5.96	0.512403	0.7490
195913_17	Stog'er Tight	Strong	0.512819	0.000036	0.16033	0.00048	420	5.48	0.512378	NA
195913_18_1	Stog'er Tight	Strong	0.512819	0.000031	0.15573	0.00051	420	5.73	0.512391	0.8048
195913_18_2	Stog'er Tight	Strong	0.512838	0.000052	0.14646	0.00074	420	6.60	0.512435	0.6457

195913_19	Stog'er Tight	Strong	0.512812	0.000025	0.15525	0.00058	420	5.62	0.512385	0.8169
195913_20	Stog'er Tight	Strong	0.512826	0.000025	0.15526	0.00093	420	5.89	0.512399	0.7791
195913_22	Stog'er Tight	Strong	0.512812	0.000034	0.15240	0.00100	420	5.77	0.512393	0.7776
195913_23	Stog'er Tight	Strong	0.512881	0.000034	0.18260	0.00110	420	5.50	0.512379	NA
195913_24	Stog'er Tight	Strong	0.512768	0.000033	0.15820	0.00260	420	4.60	0.512333	0.9876
195913_25	Stog'er Tight	Strong	0.512835	0.000037	0.15043	0.00025	420	6.33	0.512421	0.6951
195913_26	Stog'er Tight	Strong	0.512808	0.000035	0.15085	0.00071	420	5.78	0.512393	0.7678
195913_27	Stog'er Tight	Strong	0.512757	0.000057	0.14296	0.00053	420	5.20	0.512364	0.7928
195913_28	Stog'er Tight	Strong	0.512806	0.000037	0.14565	0.00074	420	6.02	0.512405	0.7119
195913_30	Stog'er Tight	Strong	0.512833	0.000023	0.14860	0.00043	420	6.39	0.512424	0.6798
195913_31	Stog'er Tight	Strong	0.512810	0.000021	0.15139	0.00016	420	5.79	0.512394	0.7696
195913_32	Stog'er Tight	Strong	0.512829	0.000033	0.14921	0.00059	420	6.27	0.512419	0.6962
195913_33	Stog'er Tight	Strong	0.512820	0.000054	0.14927	0.00020	420	6.10	0.512409	0.7189
195913_34	Stog'er Tight	Strong	0.512806	0.000081	0.14620	0.00130	420	5.99	0.512404	0.7178
195913_35	Stog'er Tight	Strong	0.512796	0.000027	0.15970	0.00140	420	5.07	0.512357	0.9340
195913_37	Stog'er Tight	Strong	0.512715	0.000027	0.15050	0.00046	420	3.98	0.512301	0.9954
195913_38	Stog'er Tight	Strong	0.512853	0.000030	0.17430	0.00300	420	5.40	0.512374	NA
195913_39	Stog'er Tight	Strong	0.512747	0.000033	0.15606	0.00042	420	4.31	0.512318	1.0072
195913_40	Stog'er Tight	Strong	0.512801	0.000034	0.15557	0.00041	420	5.39	0.512373	0.8515
195913_41	Stog'er Tight	Strong	0.512808	0.000043	0.15930	0.00210	420	5.32	0.512370	0.8918
195913_42	Stog'er Tight	Strong	0.512853	0.000037	0.15394	0.00038	420	6.49	0.512430	0.6898
195913_43	Stog'er Tight	Strong	0.512857	0.000023	0.15643	0.00038	420	6.43	0.512427	0.7099
195908_1	Stog'er Tight	Strong	0.513361	0.000056	0.36430	0.00470	420	5.11	0.512359	NA
195908_2	Stog'er Tight	Strong	0.513175	0.000076	0.33850	0.00700	420	2.86	0.512244	NA
195908_3	Stog'er Tight	Strong	0.513198	0.000045	0.34110	0.00100	420	3.17	0.512260	NA
195908_4	Stog'er Tight	Strong	0.513309	0.000066	0.33863	0.00097	420	5.47	0.512378	NA
195908_5	Stog'er Tight	Strong	0.513310	0.000064	0.34176	0.00063	420	5.33	0.512370	NA

195908_7	Stog'er Tight	Strong	0.513260	0.000053	0.34718	0.00038	420	4.06	0.512305	NA
195908_8	Stog'er Tight	Strong	0.513327	0.000084	0.35578	0.00025	420	4.90	0.512348	NA
16SJP001_1_1	Stog'er Tight	Proximal	0.512860	0.000047	0.14770	0.00210	420	6.96	0.512454	0.6057
16SJP001_2_1	Stog'er Tight	Proximal	0.512913	0.000058	0.19570	0.00240	420	5.42	0.512375	NA
16SJP001_5_1	Stog'er Tight	Proximal	0.512820	0.000057	0.16475	0.00075	420	5.26	0.512367	NA
16SJP001_7_1	Stog'er Tight	Proximal	0.512815	0.000056	0.15590	0.00130	420	5.64	0.512386	0.8182
16SJP001_8_1	Stog'er Tight	Proximal	0.512746	0.000064	0.15765	0.00094	420	4.20	0.512312	1.0397
16SJP001_9_1	Stog'er Tight	Proximal	0.512829	0.000048	0.16130	0.00140	420	5.63	0.512385	NA
16SJP001_10_1	Stog'er Tight	Proximal	0.512837	0.000060	0.16480	0.00340	420	5.59	0.512384	NA
16SJP001_11_1	Stog'er Tight	Proximal	0.512817	0.000068	0.15660	0.00200	420	5.64	0.512386	0.8231
16SJP001_12_1	Stog'er Tight	Proximal	0.512835	0.000057	0.16650	0.00150	420	5.46	0.512377	NA
16SJP001_13_1	Stog'er Tight	Proximal	0.512769	0.000080	0.16250	0.00270	420	4.39	0.512322	NA
16SJP001_14_1	Stog'er Tight	Proximal	0.512849	0.000057	0.21800	0.01500	420	2.97	0.512249	NA
16SJP001_1	Stog'er Tight	Proximal	0.512789	0.000056	0.18500	0.01400	420	3.57	0.512280	NA
16SJP001_2	Stog'er Tight	Proximal	0.512862	0.000040	0.17130	0.00120	420	5.73	0.512391	NA
16SJP001_5	Stog'er Tight	Proximal	0.512846	0.000044	0.16790	0.00170	420	5.60	0.512384	NA
16SJP001_6	Stog'er Tight	Proximal	0.512877	0.000055	0.18370	0.00330	420	5.36	0.512372	NA
16SJP001_8	Stog'er Tight	Proximal	0.512837	0.000051	0.17560	0.00510	420	5.01	0.512354	NA
16SJP001_12	Stog'er Tight	Proximal	0.512808	0.000054	0.15230	0.00220	420	5.70	0.512389	0.7865
16SJP001_13	Stog'er Tight	Proximal	0.512814	0.000032	0.15546	0.00070	420	5.65	0.512386	0.8145
16SJP001_15	Stog'er Tight	Proximal	0.512816	0.000054	0.15448	0.00076	420	5.74	0.512391	0.7952
16SJP001_16	Stog'er Tight	Proximal	0.512890	0.000050	0.16510	0.00140	420	6.61	0.512436	NA
16SJP001_17	Stog'er Tight	Proximal	0.512828	0.000046	0.15570	0.00160	420	5.91	0.512400	0.7798
16SJP001_19	Stog'er Tight	Proximal	0.512838	0.000028	0.15642	0.00078	420	6.06	0.512408	0.7623
16SJP001_20	Stog'er Tight	Proximal	0.512861	0.000045	0.17030	0.00440	420	5.77	0.512393	NA
16SJP001_21	Stog'er Tight	Proximal	0.512814	0.000066	0.16140	0.00370	420	5.33	0.512370	NA
16SJP001_24	Stog'er Tight	Proximal	0.512833	0.000031	0.15680	0.00140	420	5.95	0.512402	0.7816

16SJP001_25	Stog'er Tight	Proximal	0.512809	0.000034	0.15456	0.00043	420	5.60	0.512384	0.8150
16SJP001_26	Stog'er Tight	Proximal	0.512821	0.000038	0.17516	0.00075	420	4.72	0.512339	NA
16SJP001_27	Stog'er Tight	Proximal	0.512888	0.000061	0.19960	0.00480	420	4.72	0.512339	NA
16SJP001_28	Stog'er Tight	Proximal	0.512786	0.000064	0.18130	0.00220	420	3.71	0.512287	NA
16SJP001_29	Stog'er Tight	Proximal	0.512891	0.000076	0.17530	0.00810	420	6.08	0.512409	NA
16SJP001_31	Stog'er Tight	Proximal	0.512889	0.000044	0.18510	0.00400	420	5.52	0.512380	NA
16SJP001_32	Stog'er Tight	Proximal	0.512704	0.000090	0.15187	0.00044	420	3.69	0.512286	1.0462
16SJP001_33	Stog'er Tight	Proximal	0.512844	0.000078	0.16830	0.00160	420	5.54	0.512381	NA
16SJP001_35	Stog'er Tight	Proximal	0.512881	0.000054	0.15970	0.00096	420	6.73	0.512442	0.6841
I1951379_3	Stog'er Tight	Proximal	0.512741	0.000059	0.15240	0.00230	420	4.39	0.512322	0.9604
I951379_5	Stog'er Tight	Proximal	0.512749	0.000037	0.14460	0.00110	420	4.96	0.512351	0.8304
I951379_8	Stog'er Tight	Proximal	0.512748	0.000050	0.15110	0.00110	420	4.59	0.512332	0.9221
I951379_10	Argyle	Proximal	0.512713	0.000064	0.14770	0.00150	420	4.09	0.512307	0.9566
I951379_11	Argyle	Proximal	0.512726	0.000048	0.14533	0.00087	420	4.47	0.512326	0.8925
I951379_12	Argyle	Proximal	0.512715	0.000054	0.14930	0.00030	420	4.04	0.512304	0.9762
I951379_14	Argyle	Proximal	0.512748	0.000074	0.14900	0.01100	420	4.70	0.512338	0.8912
I951379_15	Argyle	Proximal	0.512755	0.000062	0.14506	0.00072	420	5.05	0.512356	0.8224
I951379_26	Argyle	Proximal	0.512670	0.000052	0.15900	0.00150	420	2.64	0.512233	1.2863
I951379_30	Argyle	Proximal	0.512778	0.000043	0.15449	0.00018	420	5.00	0.512353	0.8968
16SJP002_1	Stog'er Tight	Proximal	0.513307	0.000061	0.35347	0.00091	420	4.64	0.512335	NA
16SJP002_2	Stog'er Tight	Proximal	0.513400	0.000055	0.38720	0.00440	420	4.64	0.512335	NA

Notes: The chondritic uniform reservoir (CHUR) used in calculation is assumed to have $^{147}Sm/^{144}Nd$ of 0.196593 and present-day $^{143}Nd/^{144}Nd$ of 0.512638. Calculation of depleted mantle model ages (where possible) follows the model of Goldstein et al. (1984). The 420 Ma age is based upon the U–Pb results of Ramezani et al. (2000). T_{DM} ages is given in Ga.